# Modeling Phonon-Polariton Generation and Control in Ferroelectric Crystals



by

Zhao Chen

Submitted to the Department of Physics
in partial fulfillment of the requirements for the degree of

Master of Science in Physics



at the

MASSACHUSETTS INSTITUTE OF TECHNOLOGY

June 2009



Author .....
Department of Physics
May, 2009

Certified by .....
Keith A. Nelson
Professor of Chemistry
Thesis Supervisor

Certified by .....
J. David Litster
Professor of Physics
Thesis Supervisor

Accepted by ....
Thomas J. Greytak
Professor of Physics
Associate Department Head for Education

# Modeling Phonon-Polariton Generation and Control in Ferroelectric Crystals

by

Zhao Chen

Submitted to the Department of Physics
on May, 2009, in partial fulfillment of the
requirements for the degree of
Master of Science in Physics

## Abstract

In this thesis, we present simulations, using Finite Element Method (FEM), of phonon-polariton generation and coherent control in ferroelectric crystals $LiNbO_3$ and $LiTaO_3$ through nonlinear electro-optic interactions with ultrashort laser pulses. This direct space-time monitoring platform is used to investigate the nature of the excitation mechanism, the science of propagation in patterned structure, and the waveform control via multi-dimensional pulse shaping. Compared with previous simulation methods, this platform demonstrates considerable improvement in complex domain by achieving varied accuracy over space based on the level of interest of the region, which may facilitate scientific exploration in high power terahertz generation and polaritonic signal processing.

Thesis Supervisor: Keith A. Nelson
Title: Professor of Chemistry

Thesis Supervisor: J. David Litster
Title: Professor of Physics

# Acknowledgments

This thesis marks the end of a challenging but fruitful journey. The experience in the past three years in every aspect of my life is profoundly memorable, and my heart is filled with nothing but gratitude for being able to live in the persistent commitment to excellence and relentless pursuit of perfection. Behind these are many exceptional individuals, to whom I would like to extend my sincerest thanks and appreciation.

First and foremost, I would like to thank my advisors Prof. Keith A. Nelson and Prof. J. David Litster, for leading me through the unprecedented difficult period of my life with their constant trust, understanding and encouragement, both academically and personally. Their inspirational advice is beyond measure, and it is my great honor to learn dedication, perseverance and sacrifice from them.

This work could not have been accomplished without numerous discussions with other group members, whose knowledge and personalities make the whole group a truly stimulating place to stay. Special thanks to Matthias Hoffmann and Kung-Hsuan Lin for their tremendous guidance, and I would also like to thank current group members Dylan Arias, Nathaniel Brandt, Harold Hwang, Jeremy Johnson, Christoph Klieber, Kara Manke, Cassandra Newell, Gagan Saini, Taeho Shin, Kathy Stone, Vasily Temnov, Duffy Turner, Johanna Wendlandt, Patrick Wen, Kit Werley, and Ka-Lo Yeh. I wish everyone success and happiness.

I am grateful for the brotherhood and friendship with many people on this campus and in my life. Sharing life with them has been invaluable.

Finally, I deeply appreciate the love and support of my family. I can not think of words to thank them enough for all they have done for me.

*To my Mom, my Dad and my Sister.*

# Contents

# List of Figures

# List of Tables

# Chapter 1

# Introduction

The continuing rapid development of terahertz (THz) science and technology [30, 85, 102, 64, 87], whose spectral region lies between 100 GHz and 10 THz, has sparked intense scientific research interest across many fields and brought numerous breakthroughs in a wide range of applications in high power THz generation, THz imaging and THz spectroscopy. Among many sources of terahertz radiation, generation through nonlinear electro-optic effects using ultrashort laser pulses has spearheaded THz research for the past few decades with its simplicity and high efficiency. The radiation originates from the collective elementary excitation called phonon-polariton in nonlinear electromagnetic media, such as ferroelectric materials $LiNbO_3$ and $LiTaO_3$, among others.

In this thesis we present novel simulations, using Finite Element Method (FEM), of phonon-polariton generation and propagation in bulk, thin and patterned ferroelectric crystals, mainly $LiNbO_3$ and $LiTaO_3$. We also treat terahertz waveform control through the temporal and spatial shaping of ultrashort optical driving pulses. This is particularly interesting since the results coming from the solutions of the governing partial differential equations (PDE), or the ideal solutions, could be compared with experiments in which many more expected and unexpected factors are involved. Furthermore, the parametric optimization for the output field and the direct space-time monitoring of the field could be greatly helpful in the early design stage of experiments.

Before the introduction of related experimental history, materials, techniques and recent developments, a typical picture of interactions of cylindrically focused femtosecond laser pulses and bulk uniaxial ferroelectric $LiNbO_3$ is presented in Figure 1-1. Both the polarization of the pump optical pulse (blue) and the generated phonon-polariton wave (orange) are along the crystal optical axis, which is the vertical Z axis in the figure. The properties of the Z component of the polariton electrical field, i.e. the lateral propagation in the Z-X plane from the front view and the cherenkov-like propagation in the Y-X plane from the top view, are illustrated. It is worth mentioning that the polariton wavevector, perpendicular to the optical axis, is also almost perpendicular to the Y axis in this case, which allows polariton detection and imaging in a region far away from the optical excitation.

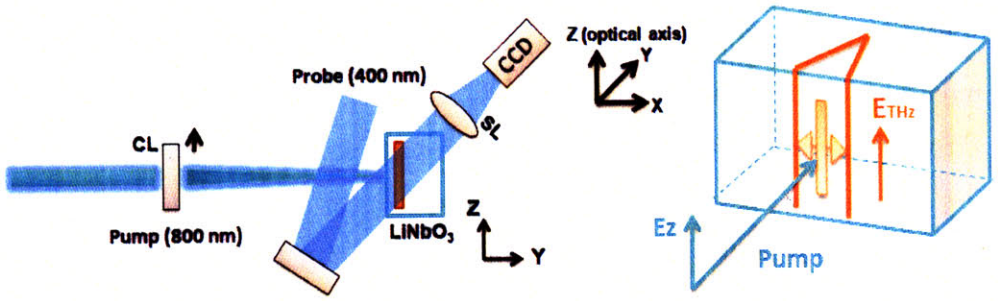


Figure 1-1: Schematic illustration of essential concepts for phonon polariton response to a cylindrically focused line source.

## 1.1 What are polaritons?

It is well known that in crystalline materials with translational symmetries, atoms vibrating around their equilibrium sites with small amplitude could be well approximated by harmonic oscillations, which could be further resolved into normal modes with each mode representing a plane wave with a certain eigenfrequency. The energy quantum of this collective excitation is called a phonon. When a long-wavelength transverse optical phonon is induced in a polar or ionic crystal, the oscillating dipoles in turn generate electromagnetic radiation, which in some cases could be in phase to form a macroscopic field as part of an electromagnetic wave propagating through the crystal. This newly formed electromagnetic wave, coupled to the transverse phonon

mode with comparable frequency and wavevector, propagates in such a special way that different frequency components propagate with different speeds, depending on the strength of their interaction with the transverse phonon wave. The energy quantum of this strongly coupled excitation is called phonon-polariton.

On the other hand, given the nature of the phonon-polariton as the internal degrees of freedom of the medium, the physical response our macroscopic system shows against a certain external perturbation, there should exist a variety of excited states of diverse character and origin, which constitute the families of elementary excitations [75] and their weak interactions [72] with each other in a wide range of materials.

In general, the coupling of electromagnetic waves and polarization waves induced by elementary excitations, or quasi-particles consisting of photons and matter excitations are referred as polaritons. Some other examples include: coupling with spin waves in ferromagnetic crystals could form magnon-polaritons [93]; coupling with collective electron vibrations could form plasmon-polaritons; coupling with electron-hole excitations could form exciton-polaritons; also, all bulk polaritons have their counterparts at the crystal surface, such as surface plasmon polaritons [66, 76], surface exciton polaritons, etc.

The existence of polaritons was first predicted by Huang [46, 47] in an isotropic diatomic ionic crystal in 1951, first denominated as polariton by Hopfield [44] in 1958, and first observed experimentally by Henry and Hopfield [43] in GaP in 1965. From a historical and experimental point of view, the discovery and early fundamental research of these quasi-particles in solids have been conducted by means of inelastic light scattering spectroscopy [11, 15, 39], on which a brief introduction would be presented next.

## 1.2 History with Raman and Brillouin Scattering

Brillouin studied the interaction of light with acoustic waves [14] in 1922. The now named Raman effect was predicted in a two quantized energy level system by Smekal [95] in 1923, and discovered in liquids and gases by C.V. Raman [81, 82] and in crys-

tals by Landsberg and Mandelstam [62] both in 1928. In Raman's ground-breaking experiment, scattering from a beam of sunlight converged by telescopes was detected with the method of complementary light-filters. It was demonstrated that in ordinary light scattering, "the diffuse radiation of the ordinary kind, having the same wave length as the incident beam, is accompanied by a modified scattered radiation of degraded frequency [81]", which are called Rayleigh scattering and Stokes scattering respectively at present.

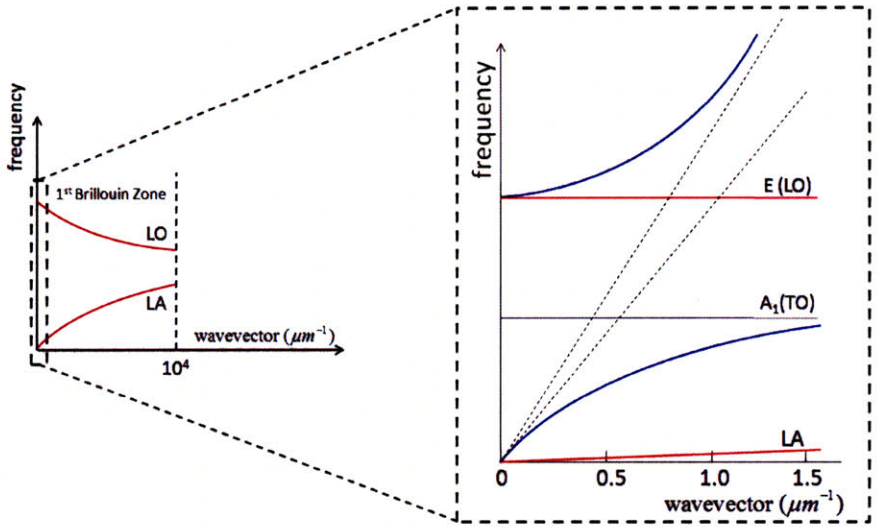


Figure 1-2: Dispersion curves of the long-wavelength optical phonons, photons and polaritons near the center of the first Brillouin zone.

This newly discovered effect was used extensively in the study of excitations of molecules and crystals, also the observation of Raman scattering by optical phonons in diamonds [80] in the early days of mercury arcs. However, theoretical development of quantum treatment [24, 27, 58], polarizability theory [77], lattice dynamics [12, 44, 46, 47], general polarization waves in polyatomic crystal [60], and Stimulated Brillouin and Raman Scattering [90, 92] had been dominating experimental work until the advent and development of the laser in 1960s. Since then elementary excitations in solids, including acoustical and optical phonons [84], single and collective electronic excitation, magnetic excitations, surface and bulk polaritons had been observed and systematically studied by inelastic Raman and Brillouin scattering in metals, semiconductors, insulators, superconductors and magnetic materials, among which the

study of ferroelectric crystal $LiNbO_3$ and $LiTaO_3$ was particularly interesting due to its excellent nonlinear optical properties [37, 114].

Raman scattering by optical phonons in $LiNbO_3$ was conducted in 1960s with focus on its dielectric dispersion [61], assignments of polar phonon modes ($4A_1 + 9E$) [4, 9, 86] and measurement of electro-optic coefficients [49]. Scattering by phonon-polaritons in $LiNbO_3$ was observed several years later [94] since the polariton wavevector region lies around the center of the first Brillouin zone (Figure **??**) that the angle between the incident light and scattered light is as small as several degrees. Directional dispersion of extraordinary polaritons [78], polaritons in $LiTaO_3$ [3], nonlinear interactions of polaritons [70] and upper polariton branch [36] were all carefully studied in the 1970s.

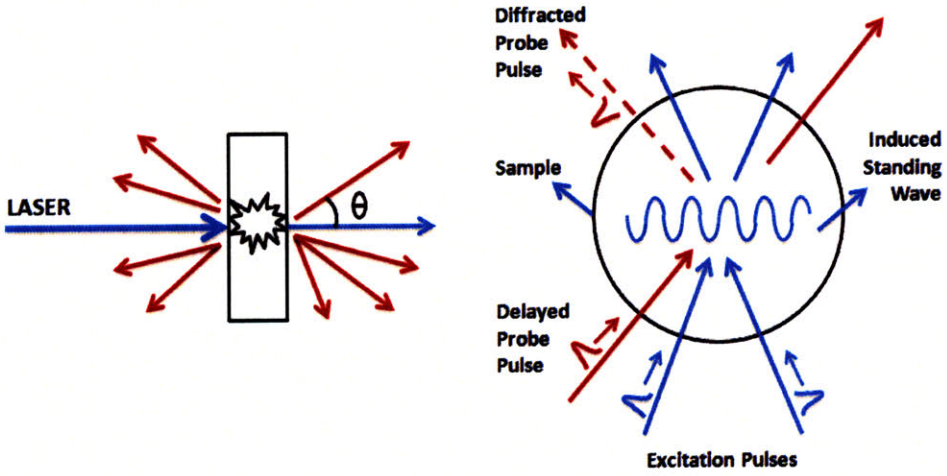


Figure 1-3: Schematic representation of (a) traditional light scattering experiment (b) the Impulsive Stimulated Scattering (ISS) experiment [115].

With the rapid development of laser technology, especially the advent of femtosecond lasers [35, 89] in early 1980s, observations on time scales shorter than an individual vibrational oscillation period came into reality [88, 23]. Many fundamental elementary excitations, including coherent acoustic phonons, optic phonons and polaritons were carefully studied with a novel Impulsive Stimulated Scattering (ISS) technique [115, 116, 117]. As shown schematically in Figure 1-3, a spatially periodic, temporally impulsive interference pattern, created by crossing two ultrashort pulses into the sample, was used to excite coherent vibrational waves, which could be further

monitored by diffraction of a third variably delayed probe pulse. This allowed the direct time resolved characterization at various stages of stretched molecules, distorted crystal lattices, anharmonic vibrations and their relaxation behavior. The light scattering processes were denominated Impulsive Stimulated Raman Scattering (ISRS) [115] and Impulsive Stimulated Brillouin Scattering (ISBS) [28] accordingly.

In 1990s a series of ISRS experiments were conducted to study lattice dynamics of ferroelectric materials in the polariton regime[23, 25, 113]. The improvement on sensitivity and accuracy based on heterodyne detection technique [68, 21] was achieved several years later, in which the novel grating arrangement was used to overcome the pancake effect [67]. An even more direct technique, spatiotemporal phonon-polariton imaging [1, 54, 53], was developed to fully characterize the collective vibrational response travelling at light-like speeds. With this powerful tool, research about coherent control over lattice vibrational waves was made possible and brought into reality recently.

## 1.3 Phonon Polariton Generation and Control

Ferroelectric materials, especially $LiNbO_3$ and $LiTaO_3$, have long been seen in use as highly functional components in optical technologies such as optical communications, signal processing and interconnection, thermal detection and frequency conversion [37, 65, 104]. The potential use in technologies of polariton regime, or terahertz polaritonics, has been explored in the past few years with many fundamental research and development efforts conducted with these materials.

As early as the 1970s, a series of experiments demonstrated far-infrared generation through optical rectification [118, 91] and ultrafast photoconductive switching [71]. The coherent Cherenkov-like far-infrared radiation from femtosecond optical pulse propagation in electro-optic media, which was $LiTaO_3$ in the experiment, was observed in 1984 at Bell Laboratories [7, 51, 8, 6]. Phonon-polariton generation with spatiotemporal pulse shaping [100, 31, 32], spatiotemporal imaging [1, 54, 53], and integrated functional elements such as waveguide, resonator, reflector and diffractive

elements [101, 98, 33, 99, 107, 111, 109], constitute the main polaritonic toolset.

Along with the development of terahertz polaritonics [30] in the linear regime, some research in the nonlinear response regime has been conducted via phonon polariton focusing in the crystal [45] and high power terahertz generation with a tilted-pulse-front technique [40, 42, 121, 122, 123]. Much fundamental research in the nonlinear terahertz spectroscopy and potential applications in many other fields are yet to be explored.

Given that the goal of this thesis is to directly simulate phonon-polariton generation, propagation and coherent control, the detailed theoretical background of the coupled polariton wave and its excitation through Impulsive Stimulated Raman Scattering (ISRS) follow next in Chapter 2. In Chapter 3, the basics of the Finite Element Method (FEM) and simulations in two and three dimensions are elaborated. The results of polaritons in bulk crystals, including the isotropic case and directional dispersion in anisotropic case, and broadband, narrowband and tilted-pulse-front excitation are in Chapter 4. Following that in Chapter 5 are generation and propagation in ferroelectric waveguides, including the dispersion properties and narrowband tunability. Finally in Chapter 6, THz field amplification through phonon-polariton focusing is presented.

# Chapter 2

# Theoretical Background of Phonon-Polariton Generation

The phonon-polariton as an elementary excitation in solids [12], the light scattering by phonon-polaritons [11, 39, 20], and the optic phonons and polaritons in ferroelectric crystals [4, 5] have been understood for decades. The theoretical treatment of phonon-polariton excitation by intense femtosecond laser pulses was developed as well [51, 8, 115, 116, 117, 83, 13, 23]. Given that the purpose of simulations is to better understand and explain experiment, we would try to present a brief but complete description of the assumptions and parameters of the mathematic model used for the phonon-polariton generation and propagation in this thesis. First and foremost, the platform lithium niobate ($LiNbO_3$) and lithium tantalate ($LiTaO_3$) are introduced.

## 2.1 Ferroelectric Crystals

$LiNbO_3$ and $LiTaO_3$ consist of planar sheets of oxygen atoms in a distorted hexagonal configuration below its Curie temperature as shown in Figure 2-1. The Li and Nb (Ta) ions are forced to move from the positions in higher symmetric non-polar paraelectric phase to the positions in ferroelectric phase. It can be seen that Nb ions are slightly above the centers between two oxygen planes, and Li ions are slightly above the oxygen planes. This structure lacks inversion symmetry and shows spontaneous polarization

along the c axis, which is also the optic axis and extraordinary axis for this uniaxial crystal.

The polar lattice phonon modes in $LiNbO_3$ and $LiTaO_3$ are the well know $4A_1 + 9E$ [49], where A means symmetry with respect to the most-fold axis, and E means twofold degeneracy. The phonon-polaritons in $LiNbO_3$ and $LiTaO_3$ discussed in this thesis are primarily coupled to the lowest frequency optic phonons along any direction, in which the coupling with lowest $A_1$ soft mode corresponds mostly to the vibrations of Li and Nb atoms along the optic axis, and the coupling with E mode corresponds mostly to the stretching of the oxygen tetrahedra in the plane perpendicular to the optic axis. Both transverse and longitudinal optic phonons can be A or E modes.

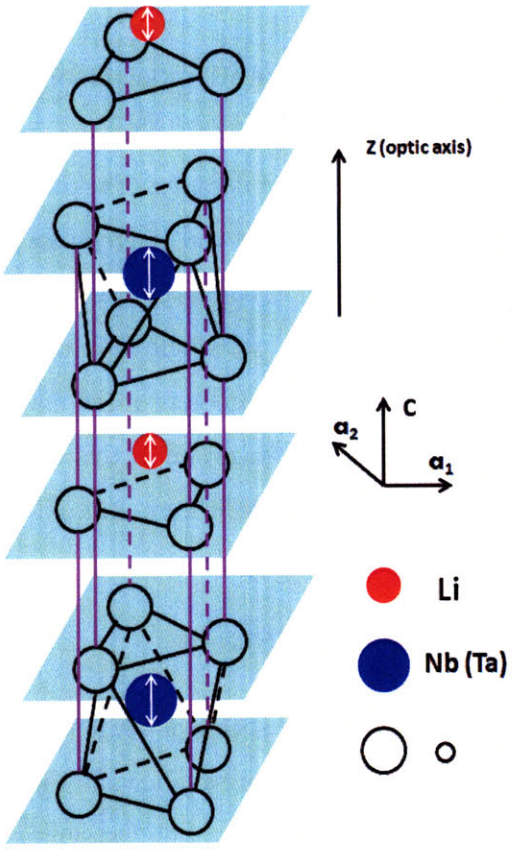


Figure 2-1: The crystal structure of lithium niobate and lithium tantalate.

## 2.2 Phonon Polaritons in Ionic Crystals

### 2.2.1 Phonon Equation

While it is a long standing effort to probe anharmonic lattice vibrations, most of the terahertz polaritonics work [30] are in the linear regime. The ion motion is modelled as a forced harmonic oscillator, which can be described by the linear macroscopic equations [12],

$$\ddot{\vec{Q}} = b_{11}\vec{Q} + b_{12}\vec{E} \tag{2.1}$$

$$\vec{P} = b_{21}\vec{Q} + b_{22}\vec{E} \tag{2.2}$$

where $\vec{P}$ is the dielectric polarization, $\vec{E}$ is the macroscopic electric field, $b$ coefficients are constants characteristic of the substance and direction relative to the optic axis of the uniaxial crystal, and $Q$ is the phonon normal mode displacement expressed as

$$\vec{Q} = \sqrt{NM}\vec{\mathrm{w}} \tag{2.3}$$

where

$$\frac{1}{M} = \sum \frac{1}{m_i} \tag{2.4}$$

$$N = \frac{4}{\sqrt{3}}\frac{1}{a^2 c} \tag{2.5}$$

$$\vec{\mathrm{w}} = \sqrt{\frac{\sum m_i \vec{r_i}^2}{M}} \tag{2.6}$$

where $M$ is the reduced mass of the unit cell, $i$ iterates over every single atom in the unit cell, $\vec{r_i}$ are the displacement of each atom from their equilibrium positions, $N$ is the oscillator density expressed with hexagonal lattice coordinates $a$ and $c$, and $\vec{\mathrm{w}}$ is the reduced mass displacement.

To account for interactions among different eigenmodes of lattice vibrations, a

phenomelogical damping term $\Gamma$ is introduced into equation (2.1),

$$\ddot{\vec{Q}} + \Gamma\dot{\vec{Q}} - b_{11}\vec{Q} = b_{12}\vec{E} \tag{2.7}$$

### 2.2.2 Photon Equation

To rigourously describe the motion of the electromagnetic fields, Maxwell's equations are introduced,

$$\nabla \times \vec{E} = -\frac{\partial \vec{B}}{\partial t} \tag{2.8}$$

$$\nabla \times \vec{H} = \frac{\partial \vec{D}}{\partial t} \tag{2.9}$$

$$\nabla \cdot \vec{B} = 0 \tag{2.10}$$

$$\nabla \cdot \vec{D} = 0 \tag{2.11}$$

which combined with vector and scalar potentials,

$$\vec{B} = \nabla \times \vec{A}, \quad \vec{E} = -\frac{\partial \vec{A}}{\partial t} - \nabla\phi \tag{2.12}$$

and coupled with displacement fields of polar phonon motions (2.2),

$$\vec{D} = \varepsilon_0\vec{E} + \vec{P} = (\varepsilon_0 + b_{22}) + b_{21}\vec{Q} \tag{2.13}$$

can lead to the wave equation,

$$(\nabla^2\vec{A} - \frac{1}{c_0^2/\varepsilon_\infty}\ddot{\vec{A}}) - \nabla\cdot((\nabla\cdot\vec{A}) + \frac{1}{c_0^2/\varepsilon_\infty}\dot{\phi}) = -\mu_0\omega_{\mathrm{TO}}\sqrt{\epsilon_0(\varepsilon_0 - \varepsilon_\infty)}\dot{\vec{Q}} \tag{2.14}$$

if we choose the polariton gauge,

$$\nabla\cdot\vec{A} = -\frac{\varepsilon_\infty}{c_0^2}\dot{\phi} \tag{2.15}$$

the coupled vector potential equation is described as,

$$(\nabla^2\vec{A} - \frac{1}{c_0^2/\varepsilon_\infty}\ddot{\vec{A}}) = -\mu_0\omega_{\mathrm{TO}}\sqrt{\epsilon_0(\varepsilon_0-\varepsilon_\infty)}\dot{\vec{Q}} \tag{2.16}$$

### 2.2.3 Phonon-polariton Equation

The governing equations to describe the joint vibrational modes of radiation field and lattice behavior, or phonon-polariton dynamics, are summarized as,

$$\begin{cases} \ddot{\vec{Q}} + \Gamma\dot{\vec{Q}} - b_{11}\vec{Q} &= b_{12}\vec{E} \\ (\nabla^2\vec{A} - \frac{1}{c_0^2/\varepsilon_\infty}\ddot{\vec{A}}) &= -\mu_0\omega_{\mathrm{TO}}\sqrt{\epsilon_0(\varepsilon_0-\varepsilon_\infty)}\dot{\vec{Q}} \end{cases} \tag{2.17}$$

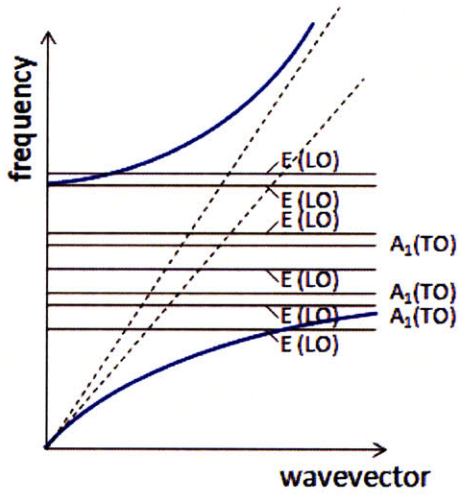


Figure 2-2: Qualitative sketch of phonon-polariton dispersion in $LiNbO_3$ when the wave vector is perpendicular to the optic axis. All longitudinal lattice vibrations are without dispersion while there is strong interaction between lowest $A_1$ transverse mode and electromagnetic wave.

Complete solutions should include the lattice longitudinal and transverse modes, which can be derived from the phonon equation alone; optical waves propagating in the crystal, which can be derived from the photon equation alone; and new coupled solutions corresponding to the inseparable interactions between them. In another word, solutions of phonon-polariton equations include all possible phonon, photon and polariton waves in this system. The detailed derivation has been worked out before [12], and the general conclusions can be shown qualitatively with the $LiNbO_3$

dispersion sketches in Figure 2-2, where only the coupling with lowest $A_1$ mode is considered.

As can be easily seen, all longitudinal vibrations are without dispersion within the phonon-polariton wave vector range, which means there is no interaction between the longitudinal mode and the radiation field, and evidently $\vec{Q} \parallel \vec{E} \parallel \vec{P} \parallel \vec{k}$, $\vec{H} = 0$ in this case. On the other hand, the strong coupling of the lowest transverse lattice wave and electromagnetic wave leads to the partial phonon partial photon dispersion, which lifts the crossing between the pure light curve (dotted line) and the pure lattice $A_1(\mathrm{TO})$ curve, and evidently $\vec{Q} \parallel \vec{E} \parallel \vec{P} \perp \vec{H} \perp \vec{k}$ in this case.

### 2.2.4 Quantitative Dispersion

With the constitutive relation $P(w) = \epsilon_0(\varepsilon_r(\omega) - 1)E(\omega)$, the dielectric function can be derived from equation (2.2),

$$\varepsilon_r(\omega) = 1 + \frac{b_{22}}{\epsilon_0} + \frac{1}{\epsilon_0}\frac{b_{12}b_{21}}{\omega_{\mathrm{TO}}^2 - \omega^2 - i\omega\Gamma} \tag{2.18}$$

Comparing the two off-resonance limits

$$\varepsilon_\infty = 1 + \frac{b_{22}}{\epsilon_0}, \quad \varepsilon_0 = \varepsilon_\infty + \frac{b_{12}b_{21}}{\epsilon_0\omega_{\mathrm{TO}}^2} \tag{2.19}$$

and the rigorous transverse solution of the phonon-polariton equation, the coupling $b$ coefficients can be written as,

$$b_{11} = \omega_{\mathrm{TO}}^2 \tag{2.20}$$

$$b_{12} = b_{21} = \omega_{\mathrm{TO}}\sqrt{\epsilon_0(\varepsilon_0 - \varepsilon_\infty)} \tag{2.21}$$

$$b_{22} = \epsilon_0(\varepsilon_\infty - 1) \tag{2.22}$$

The dielectric function itself becomes

$$\varepsilon_r(\omega) = \varepsilon_\infty + \frac{\omega_{\mathrm{TO}}^2(\varepsilon_0 - \varepsilon_\infty)}{\omega_{\mathrm{TO}}^2 - \omega^2 - i\omega\Gamma} \tag{2.23}$$

so the dispersion relations are,

$$\omega(k) = \sqrt{\frac{\omega_{\mathrm{TO}}^2\varepsilon_0 + c^2k^2}{2\varepsilon_\infty} \pm \frac{1}{2}\sqrt{(\frac{\omega_{\mathrm{TO}}^2\varepsilon_0 + c^2k^2}{\varepsilon_\infty})^2 - \frac{4\omega_{\mathrm{TO}}^2\varepsilon_0 c^2k^2}{\varepsilon_\infty}}} \tag{2.24}$$

in which the positive and negative roots correspond to the upper and lower branches respectively, as shown by the blue lines in Figure 2-3.

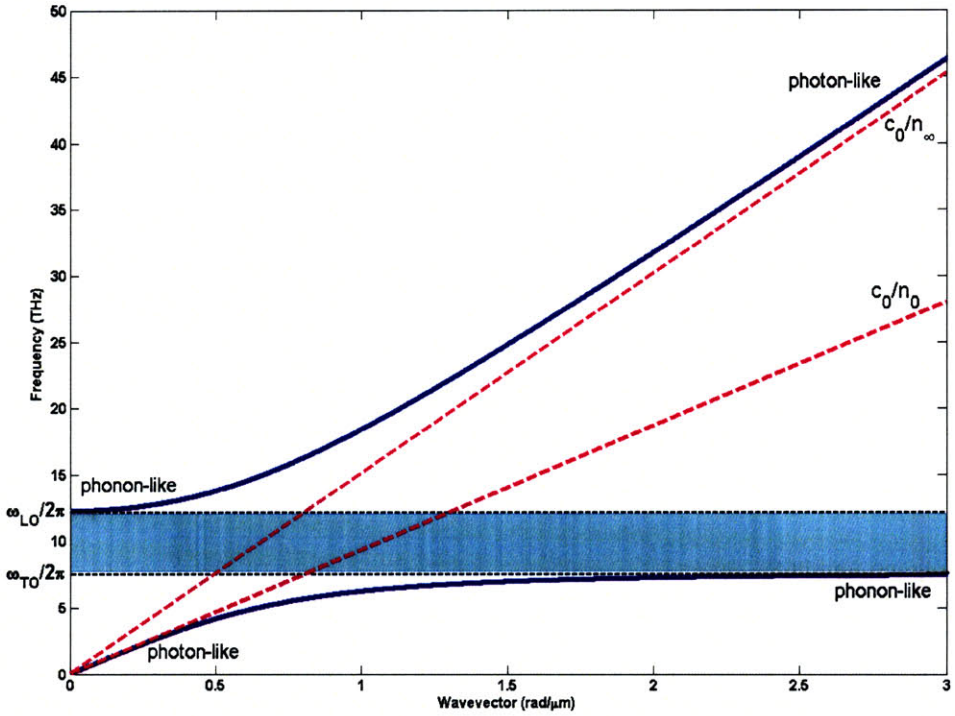


Figure 2-3: Dispersion curve for the lowest transverse phonon mode of $LiNbO_3$.

It is clear that the dispersion relations are characterized by three parameters: $\omega_{\mathrm{TO}}$ is the resonance frequency of the lowest transverse optic phonon mode, and $\varepsilon_0$ and $\varepsilon_\infty$ are the dielectric constants in low and high frequency limits. The high frequency here means it is much higher than the resonance frequency $\omega_{\mathrm{TO}}$ but still smaller than the first brillouin zone boundary so that the wave vector-dependence of phonon frequencies can be eliminated. The low frequency limit $\omega_{\mathrm{LO}}$ of the upper branch is marked LO because the mechanical and electromagnetic motions are completely out

of phase in this case, and it has the same resonance frequency as the longitudinal branch. The analytical expression is,

$$\omega_{\mathrm{LO}} = \omega_{\mathrm{TO}} \sqrt{\varepsilon_0 / \varepsilon_\infty} \tag{2.25}$$

### 2.2.5 Anisotropy in Uniaxial Dielectrics

Uniaxial crystals are characterized by the dielectric tensors $\epsilon_{xx}(\omega)$=$\epsilon_{yy}(\omega)$=$\epsilon_\perp(\omega)$ and $\epsilon_{zz}(\omega)$=$\epsilon_\parallel(\omega)$, where the $\perp$ and $\parallel$ stand for polariton wave polarization perpendicular or parallel to the optic axis. The dielectric function in equation (2.23) will be characterized by more parameters,

$$\varepsilon_\parallel(\omega) = \varepsilon_{\infty\parallel} + \frac{\omega_{\mathrm{TO}\parallel}^2(\varepsilon_{0\parallel} - \varepsilon_{\infty\parallel})}{\omega_{\mathrm{TO}\parallel}^2 - \omega^2 - i\omega\Gamma_\parallel} \tag{2.26}$$

$$\varepsilon_\perp(\omega) = \varepsilon_{\infty\perp} + \frac{\omega_{\mathrm{TO}\perp}^2(\varepsilon_{0\perp} - \varepsilon_{\infty\perp})}{\omega_{\mathrm{TO}\perp}^2 - \omega^2 - i\omega\Gamma_\perp} \tag{2.27}$$

which combined with the phonon-polariton motion equation can lead to the directional dispersion relation in the general case ($0 < \theta < 90^0$) [70],

$$\varepsilon(\omega,\theta) = \frac{c^2k^2}{\omega^2} = \frac{\varepsilon_\perp(\omega)\varepsilon_\parallel(\omega)}{\varepsilon_\perp(\omega)\sin^2\theta + \varepsilon_\parallel(\omega)\cos^2\theta} \tag{2.28}$$

where $\theta$ denotes the angle between the polariton wave vector and the optic axis.

Only the lowest transverse polar mode is taken into account along any direction. More rigorous solutions can be derived based on the Kurosawa equation [60], so it is obvious that the approximation comes from the influence of higher frequency transverse polar modes. This makes equation (2.28) legitimate enough for directional dispersion calculation because even for the familiar $\theta = 90^0$ case, the influence of higher frequency polar modes is ignored.

Also interesting is that polariton waves in uniaxial crystals are not always transverse. They are mixed TO+LO type in the general propagation direction $0^0 < \theta < 90^0$ as shown in Figure 2-4. The phonon modes listed in the table are for two limiting cases $\theta = 90^0$ and $\theta = 0^0$, which do not mean the polaritons are coupled with all

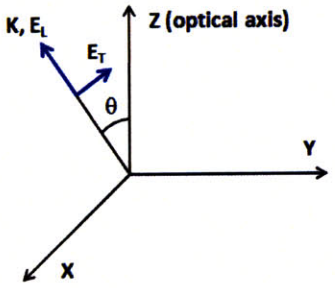


| k \|\| z, theta = 0 | | k ⊥ z, theta = 90° | |
|---|---|---|---|
| $w_{L\|\|}$ | A (LO) | $w_{T\|\|}$ | A (TO) |
| $w_{T\perp}$ | E (TO) | $w_{L\perp}$ | E (LO) |

Figure 2-4: Polariton electric field of the mixed LO+TO wave when $0^0 < \theta < 90^0$.

phonons. For instance, when $\theta = 90^0$, the polarization is along the optic axis, and the electromagnetic wave is only coupled with the $A_1$ phonon mode.

It is derived from the directional dispersion equation (2.28) that phonon polariton waves propagate linearly along three Cartesian coordinate axis, so the phonon-polariton equations can be expressed with physical constants characteristic of the substance, and for $LiNbO_3$, those constants are [4, 30],

| | $\omega_T/2\pi$ (THz) | $\Gamma/2\pi$ (THz) | $\varepsilon_0$ | $\varepsilon_\infty$ |
|---|---|---|---|---|
| $\vec{k}\perp z, \theta = 90^0$ | $\omega_{T\|\|}/2\pi = 7.6$ | $\Gamma_{\|\|}/2\pi = 0.63$ | $\varepsilon_{0\|\|} = 26.0$ | $\varepsilon_{\infty\|\|} = 10.0$ |
| $\vec{k}\|\|z, \theta = 0^0$ | $\omega_{T\perp}/2\pi = 4.6$ | $\Gamma_{\|\|}/2\pi = 0.42$ | $\varepsilon_{0\perp} = 41.5$ | $\varepsilon_{\infty\perp} = 19.5$ |

Table 2.1: Physical constants for phonon-polaritons in $LiNbO_3$.

## 2.3 Phonon-Polariton Excitation with Femtosecond Laser Pulses

The governing equations responsible for phonon-polaritons in last section clearly indicates that the phonon-polartion is an internal degree of freedom intrinsic to the substance, an elementary excitation the crystal shows against certain external per-

turbation. Actually, even just taking thermal effects into account, phonon-polariton can be excited in the crystal. However, in this section, we will present the theoretical background of coherent phonon-polariton generation with femtosecond laser pulses via Impulsive Stimulated Raman Scattering (ISRS).

### 2.3.1 Impulsive Stimulated Raman Scattering (ISRS)

Since the coherent terahertz radiation from $LiTaO_3$ was observed in early 1980s [7], there have been many experimental and theoretical work explaining the driving mechanism of this nonlinear optical process [51, 8, 25, 23, 113]. In [13], a detailed discussion about the nature of the driving force was presented.

The driving force can be put in the polariton equations,

$$\begin{cases} \ddot{\vec{Q}} + \Gamma\dot{\vec{Q}} - b_{11}\vec{Q} &= b_{12}\vec{E} + F_{ISRS} \\ (\nabla^2\vec{A} - \frac{1}{c_0^2/\varepsilon_\infty}\ddot{\vec{A}}) &= -\mu_0\omega_{\mathrm{TO}}\sqrt{\epsilon_0(\varepsilon_0 - \varepsilon_\infty)}\dot{\vec{Q}} + F' \end{cases} \tag{2.29}$$

where the $F'$ is due to pure electronic nonliearity, whose contribution to the polariton excitation is significantly smaller than the ISRS driving force [25, 23, 113], so it will be ignored in the simulations throughout this thesis.

When an intense optical beam, whose central frequency is approximately 375 THz for an 800 $nm$ laser, irradiates ferroelectric crystals, the electronic system (with resonance frequency in the ultraviolet range) responds much more strongerly than the ionic system (with resonance frequency around 7.6 THz), so the electrons will be driven in phase with the optical field. The ionic system, on the other hand, will oscillate in the far-infrared frequency range through nonlinear coupling to the electronic system. In ionic crystals with no inversion center in the unit cell, the Raman active modes are also IR active, so ion oscillations radiates electromagnetic waves, which in turn influence the ionic motion. Including the time-dependent ISRS

driving force [106, 103], phonon-polariton generation equations are,

$$\begin{cases} \ddot{\vec{Q}} + \Gamma\dot{\vec{Q}} - b_{11}\vec{Q} &= b_{12}\vec{E} + \frac{1}{2}\epsilon_0\sqrt{\frac{N}{M}}(\frac{\partial\alpha}{\partial\vec{w}})I_{pump}(t) \\ (\nabla^2\vec{A} - \frac{1}{c_0^2/\varepsilon_\infty}\ddot{\vec{A}}) &= -\mu_0\omega_{\mathrm{TO}}\sqrt{\epsilon_0(\varepsilon_0 - \varepsilon_\infty)}\dot{\vec{Q}} \end{cases} \tag{2.30}$$

In the ISRS driving term, the constants for $LiNbO_3$ are $N = 6.285 \times 10^{27}\ m^{-3}$, $M = 11.4\ amu$, $(\frac{\partial\alpha}{\partial\vec{w}})_{33} = 1.14 \times 10^{-18}\ m^2$, and the pump intensity is described in the following.

### 2.3.2 Beam Profile

The intensity profile is assumed to be a Gaussian. In three dimensional simulations, assuming the beam is propagating along y axis, the intensity can be written,

$$I(x,z,t) = I_0 e^{-(\frac{x-x_0}{\sigma x})^2 - (\frac{z-z_0}{\sigma z})^2 - (\frac{t-t_0}{\sigma_t})^2} \tag{2.31}$$

where $\sigma_x$, $\sigma_z$ and $\sigma_t$ are expressed with experimental parameters,

$$\sigma_x = \frac{\text{spotsize}}{2\sqrt{\ln 2}} \tag{2.32}$$

$$\sigma_t = \frac{\text{duration}}{2\sqrt{\ln 2}} \tag{2.33}$$

where the spotsize and duration are the full-width at half-maximum (FWHM) in a Gaussian form.

Other intensity profiles can be achieved in similar ways. For instance, a Gaussian form can be rotated to simulate a tilted-pulse-front, or modulated by a squared sinusoidal function to achieve laser induced grating, etc.

# Chapter 3

# Simulations with Finite Element Method

The understanding of phonon-polariton started with the theoretical prediction in a cubic diatomic crystal by analytically solving the equations governing the coupling of electromagnetic waves and lattice vibrations [46, 47]. Several models were introduced to explain and calculate the interactions of ultrashort pulses with ferroelectric crystals, and how the phonon-polariton wave is generated through this process. However, when it comes to a more engineering side, namely the spatiotemporal coherent control over the lattice response via pulse shaping and patterned structures, it is natural to pursue a discrete-assembly computational approximation, whose accuracy and capability have long been witnessed in engineering implementations [125, 126].

The essential idea of this approach is to subdivide the system into a number of elements, whose behavior is already well understood with given parameters and surrounding conditions, and then rebuild the original system as an approximation from those components. It is widely used to find solutions of partial differential equations (PDEs) and of integral equations across many fields in science and engineering. Among the spectrum of simulation schemes that are being used for ultrafast processes in ultrasmall systems, two approaches stand out withsubstantial research, namely the Finite Difference Time Domain (FDTD) method [119] and Finite Element Method (FEM) [126, 50, 127].

In this chapter, the basics and fundamentals of the partial differential equations (PDEs) are briefly mentioned first, following which are the introduction of FEM and FDTD methods, then the essential concepts, ideas and implementations of the simulation in this thesis are presented, both on the physical and computational side in two and three dimensions. The governing equations responsible for phonon-polariton generation and propagation in ferroelectric crystals are based on the theory presented in Chapter 2.

## 3.1 Partial Differential Equation

Partial differential equations (PDEs) are usually found as the local infinitesimal constraint imposed by the universal conservation of mass, momentum and energy in fields such as the propagation of sound or heat, electrostatics, electrodynamics, fluid flow, and elasticity, etc. PDEs are classified according their order, boundary conditions, and degree of linearity, of which the second order are usually encountered in the physical world, from the Schrödinger equation to Maxwell equations. The classical boundary value problem can be defined in domain $\Omega$ enclosed by boundary $\Gamma$:

$$L\phi = f \tag{3.1}$$

where the $L$ is a differential operator, $\phi$ is the unknown quantity, and $f$ is the source term. A general second order time-dependent example may look like:

$$e_\alpha \frac{\partial^2 \mathbf{u}}{\partial t^2} + d_\alpha \frac{\partial \mathbf{u}}{\partial t} + \nabla \cdot (-c\nabla \mathbf{u} - a\mathbf{u} + \gamma) + \alpha \mathbf{u} + \beta \cdot \nabla \mathbf{u} = f \tag{3.2}$$

where those coefficients may stand for diffusion, absorption, mass, damping and convection terms depending on the specific problems. The boundary conditions, including the exterior and interior ones, can vary from the simple Dirichlet and Neumann, to complicated impedance, periodic, scattering and radiation, etc. In the basic Neumann condition,

$$\mathbf{n} \cdot (c\nabla \mathbf{u} + a\mathbf{u} - \gamma) + q\mathbf{u} = g \tag{3.3}$$

the coefficients $q$ and $g$. Specify what values the derivative of the solution should take, while in the basic Dirichlet condition,

$$\mathbf{n} \cdot (c\nabla \mathbf{u} + a\mathbf{u} - \gamma) + q\mathbf{u} = g - h^T \mathbf{u}, \quad h\mathbf{u} = r \tag{3.4}$$

the coefficients specify what the values of the solution should take. When it comes to the electromagnetic case, the specific boundary condition can be perfect electric conductor, perfect magnetic conductor, general continuity and even surface current and potential, etc.

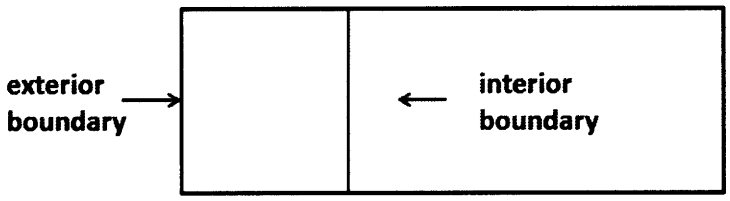


Figure 3-1: Exterior and interior boundaries.

Most physical problems can be specified by those PDEs or the strong form, while in some cases the weak form expressed as integral equations can be useful. For instance, heat transport in gas can be expressed in PDEs, but the ideal gas law for low pressure and high temperature cases should be specified by an integral, or a weak term.

## 3.2 Finite Difference in Time Domain (FDTD)

The Finite Difference Time Domain (FDTD) invented by Yee [119] in 1966 is a grid-based numerical modelling method widely used in the computational electrodynamics. It directly uses the E and H fields, and the time-dependent Maxwell's equations are discretized using central difference approximations to the space and time partial derivatives. The temporal discretization in the one dimensional case, for example, can be written as,

$$\frac{\partial f(x,t)}{\partial t} \equiv \frac{f(x,t+1/2) - f(x,t-1/2)}{\triangle t} \tag{3.5}$$

and the spatial discretization as,

$$\frac{\partial f(x,t)}{\partial x} \equiv \frac{f(x+1/2,t) - f(x-1/2,t)}{\triangle x} \tag{3.6}$$

Similarly, the $Z$ components of the equations (2.30) can be,

$$\begin{aligned} E_z[l,m,n] = E_z[l,m,n] + \frac{\Delta t}{(\epsilon_0 + b_{22})\Delta x}(H_y[l,m,n] - H_y[l-1,m,n]) \\ + \frac{\Delta t}{(\epsilon_0 + b_{22})\Delta y}(H_x[l,m-1,n] - H_x[l,m,n]) - \frac{\Delta t}{(\epsilon_0 + b_{22})}\dot{Q}_z[l,m,n] \end{aligned} \tag{3.7}$$

and

$$\begin{aligned} \dot{Q}_z[l,m,n] = (1 - \Gamma_z \Delta t)\dot{Q}_z[l,m,n] + \Delta t(b_{11}Q_z[l,m,n] \\ + b_{12}E_z[l,m,n]) + F_{ISRS} \cdot \hat{z} \end{aligned} \tag{3.8}$$

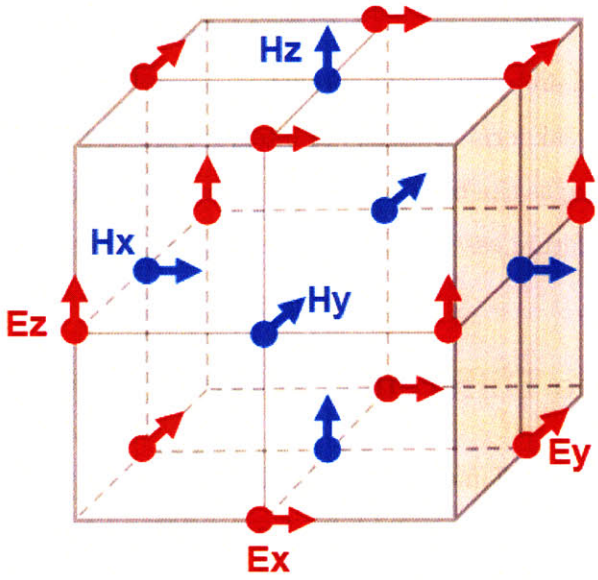


Figure 3-2: Illustration of a standard Cartesian Yee cell. The $E$ components are in the middle of the edges and the $H$ components are in the center of the faces [119].

In general, as illustrated in Figure 3.2, the entire simulation space is divided into a large number of uniform rectangular grids, where the electric fields are solved at a given time; then the magnetic fields in the same spatial volume are solved at the next

instant in time. This leapfrog manner is repeated until the desired time-dependent or steady-state electromagnetic field behavior is fully evolved.

The FDTD algorithm is straightforward and can be quickly put into implementation. It is worth mentioning that in previous simulations [97, 106, 103, 112, 108], the effective perfectly matched layer (PML) boundary condition invented by Berenger [10], which has been proved not to reflect the incoming waves of any radiation pattern, was used to accurately simulate an infinite space problem in a manageable size.

FDTD method has weaknesses as well, especially when it comes to simulation near a curved structure and resolving the skin-depth. One issue is that the rectangular grids FDTD utilizes are not efficient in discretizing the space near a curve, another is that since the grids are uniform, the dense elements in one region would have to span the entire space which makes it unnecessarily expensive to compute.

## 3.3 Finite Element Method (FEM)

The Finite Element Method (FEM) method has a relatively longer history that dates back to complex problems in structural engineering and aeronautics in 1940s. On the mathematic side, general techniques applicable to differential equations were developed, such as finite difference approximations, weighted residual procedures, trial functions, and variational finite differences, while on the engineering side, it was approached in a more intuitive way such as structural analogue substitution and direct continuum elements, etc. While the approaches developed along the history might be different from each other and the way we implement them today, the essential discrete-assembly approach should be the same.

The discretization of the domain is the first and foremost important step since the mesh shape and density distribution directly affect the computation efficiency and accuracy. In the finite element method, the mesh does not need to be uniform, and the basic shape in one dimension, either straight or curved, is a segment; in two dimensional domain triangles and quadrilaterals; and in three dimensional case, it could be tetrahedra, triangular prisms, irregular hexahedra and chisels as shown in

Figure 3-3. These subdomains are called *finite elements.* Corners of an element are called nodes, and there could be nodes in between corner points as well, i.e. edge nodes. It is ideal to generate as many elements as possible to have more elements in the region of particular interest, but the effect of improvement in accuracy with an increasing number of elements becomes negligible beyond a certain point. Many well-developed algorithms have the capability of subdividing an arbitrarily shaped domain and providing the optimization. This discretization process shows flexibility and efficiency as illustrated in Figure 3-4, which is also reflected in the second step, selection of interpolation functions.

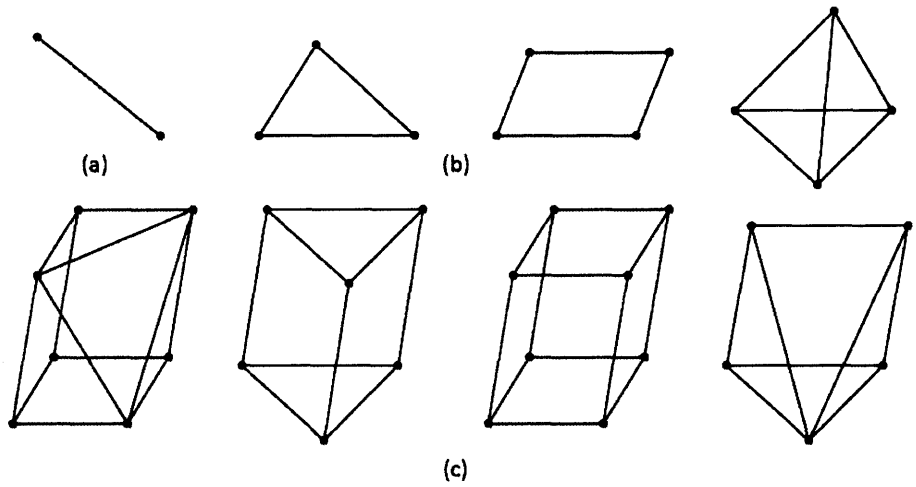


Figure 3-3: Mesh elements used in the finite element method: (a) one dimension, (b) two dimension, (c) three dimension.

The corner nodes and edge nodes are where the solutions are calculated, and interpolation can be used to provide a further approximation of the unknown solution within an element. The commonly used interpolation is the Lagrange polynomial, which uses values of the function at nodes as its degrees of freedom. The Hermite polynomial is another interpolation method, which uses the values and first derivatives at nodes as its degrees of freedom for approximation.

In terms of solving the boundary-value problem, there are two classical methods, Ritz method and Galerkin method. Both of them involve a fair amount of matrix preconditioning, assembly and decomposition in the calculation procedure, which is

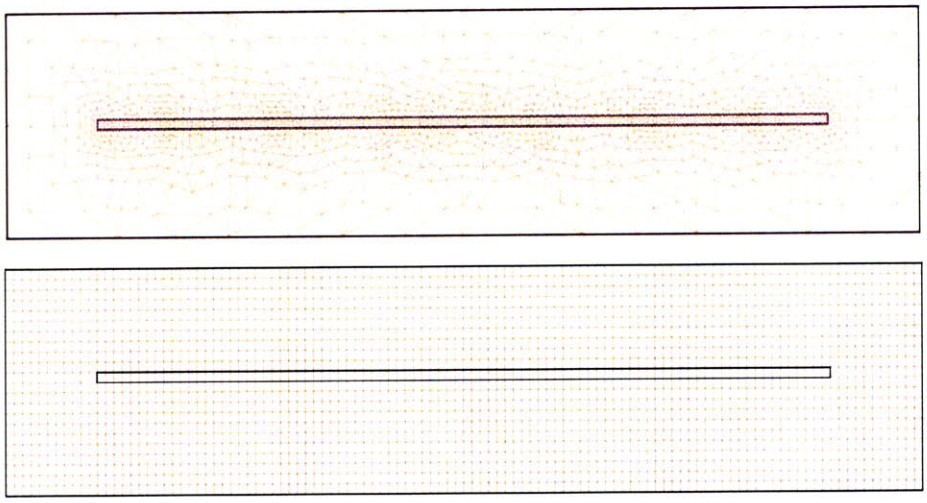

Figure 3-4: For the 2D computation of a dielectric waveguide with air as cladding, the number of mesh elements with FEM method (a) is much less than that with FDTD method (b) while maintaining better accuracy in the region of interest.

expensive in terms of memory use. This is a major weakness of FEM. However, FEM is a good choice for solving partial differential equations over complex domains, especially when the desired precision varies over the entire domain, or when it comes to real industries like car crash, airplanes, chemical reactions, weather patterns, optoelectronic devices, etc.

## 3.4 Multiphysics

On the simulation side, there are similar terms multifield, multiscale, and multidomain, but multiphysics in this thesis exclusively means simulations that involve multiple physical models, mechanisms and phenomena on the same space and time scale, and most importantly the partial differential equations of different models should couple with each other. Most physical simulation involves coupled system, like micro-electro-mechanical system (MEMS), thermal stress system, electromechanical system, etc.

The phonon-polariton excitation through Impulsive Stimulated Raman Scattering

(ISRS) is a multiphysics problem as well. The govering equations (2.30)

$$\ddot{\vec{Q}} + \Gamma\dot{\vec{Q}} + w_{TO}^2\vec{Q} = b_{12}\vec{E} + \vec{F}_{ISRS} \tag{3.9}$$

$$(\nabla^2\vec{A} - \frac{1}{c_0^2/\epsilon_\infty}\ddot{\vec{A}}) = -\mu_0 b_{21}\dot{\vec{Q}} \tag{3.10}$$

couple the phonon motion and electromagnetic propagation together, and $\vec{E}$ and $\vec{Q}$ appear in both equations.

Many commercial software packages, such as CFD-FASTRAN, COMSOL, LS-DYNA and ANSYS, could be used for simulating multiphysics models, and they mainly rely on the finite element method.

# Chapter 4

# Phonon-Polaritons in Bulk Ferroelectric Crystals

In bulk uniaxial ferroelectric crystals, properties of phonons, photons and polaritons along different directions can be fully studied. In this chapter, phonon polariton generation and propagation in bulk $LiNbO_3$ and $LiTaO_3$ crystals are introduced and simulated in both two and three dimensional cases. With some existing excitation schemes in lab, such as point source, line focus, ring excitation, and spatial-temporal pulse shaping, phonon-polariton properties and coherent control are discussed.

## 4.1 Three Dimensional Overview

In terms of phonon polariton generation and propagation through interactions of cylindrically focused femtosecond laser pulses and bulk uniaxial ferroelectric $LiNbO_3$, the typical experimental setup and schematic illustration are in Figure 4-1. In this special case, the polarization of the pump optical pulse (blue) and the generated phonon-polariton wave (orange) are both along the crystal optical axis, which is the vertical Z axis in the figure, and the polariton wave vector is perpendicular to it. The majority contribution is from the coupling of the electromagnetic wave and the lowest transverse optic phonon, which was proved to be the most efficient. It is worth mentioning that the polariton wave propagates far away from the optical excitation

region, and the second 400 nm probe beam can be used for polariton imaging, where the data are collected with a CCD camera.

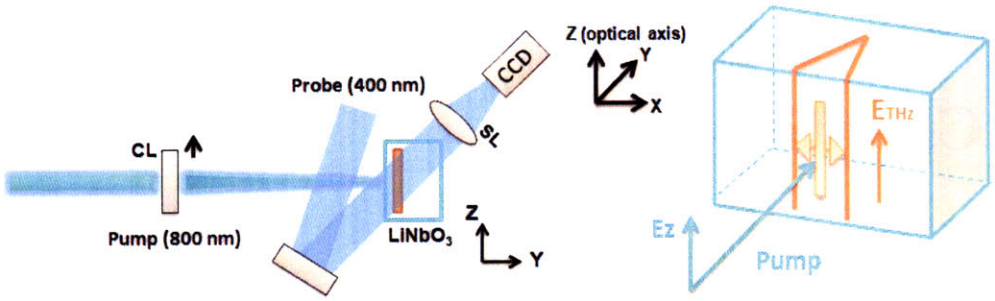


Figure 4-1: Experimental setup (a) and schematic illustration (b) for phonon polariton response to a cylindrically focused pump line source. The light blue beam is the probe, which is sensitive to the index change and can be imaged onto the camera.

The simulations of this case were implemented in a 100 $\mu m$ × 100 $\mu m$ × 50 $\mu m$ $LiNbO_3$ crystal, with the cylindrically focused line of width 15 $\mu m$ and pulse time duration 50 $fs$. As in Figure 4-2, Z component of the polariton electrical field of snapshots at 0.2 $ps$, 0.4 $ps$, 0.6 $ps$ and 0.8 $ps$ are shown. The lateral propagation in the Z-X plane from the front view and the cherenkov-like propagation in the Y-X plane from the top view, are the most important planes in which most simulations will be conducted since simulations in three dimension are computationally expensive in terms of memory use.

## 4.2 Broadband Excitation

### 4.2.1 Top View Plane

Broadband near single cycle polariton waves are usually excited with cylindrically focused pump light. The central frequency or the central wavelength of the polariton wavepacket is tuned by the dimension of the line width, or the wavevector range that could be driven by the pump laser.

The broadband polariton profile in both time and frequency domain for those two cases are shown below in Figure 4-4,

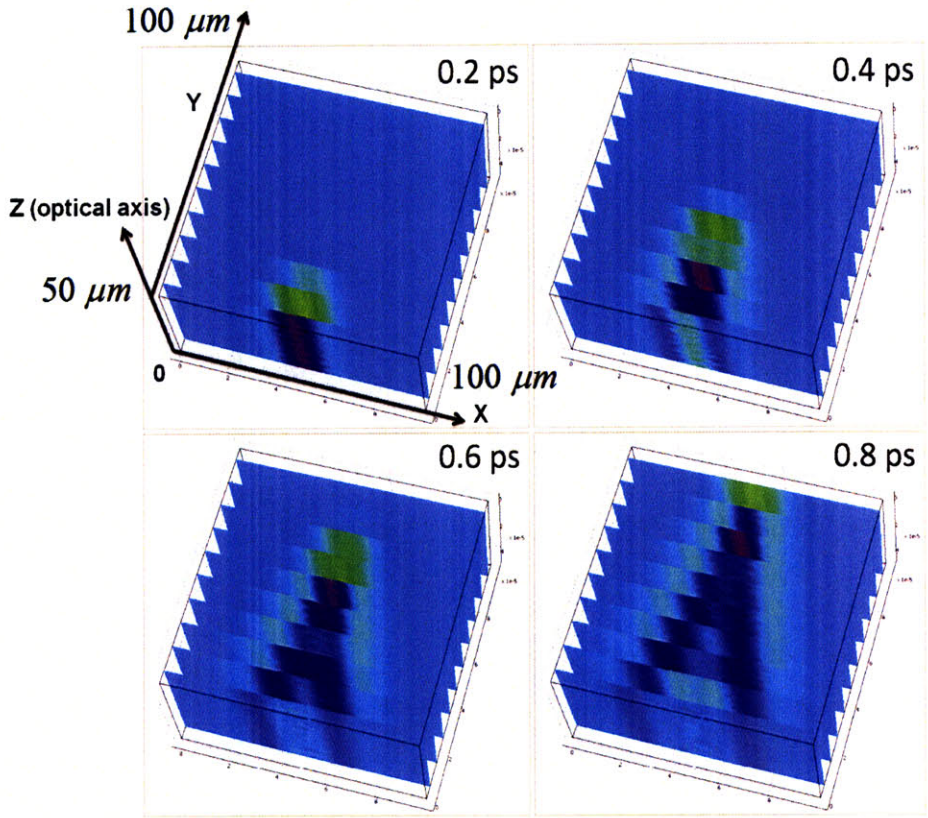


Figure 4-2: In a 100 $\mu m$ × 100 $\mu m$ × 50 $\mu m$ $LiNbO_3$ crystal, the cylindrically focused line of duration 50 $fs$, width 15 $\mu m$ was used to excite phonon polaritons. The Z component of generated polariton electrical fields are shown at 0.2 $ps$, 0.4 $ps$, 0.6 $ps$ and 0.8 $ps$ snapshots. The lateral propagation in the Z-X plane and the cherenkov-like propagation in the Y-X plane are illustrated.

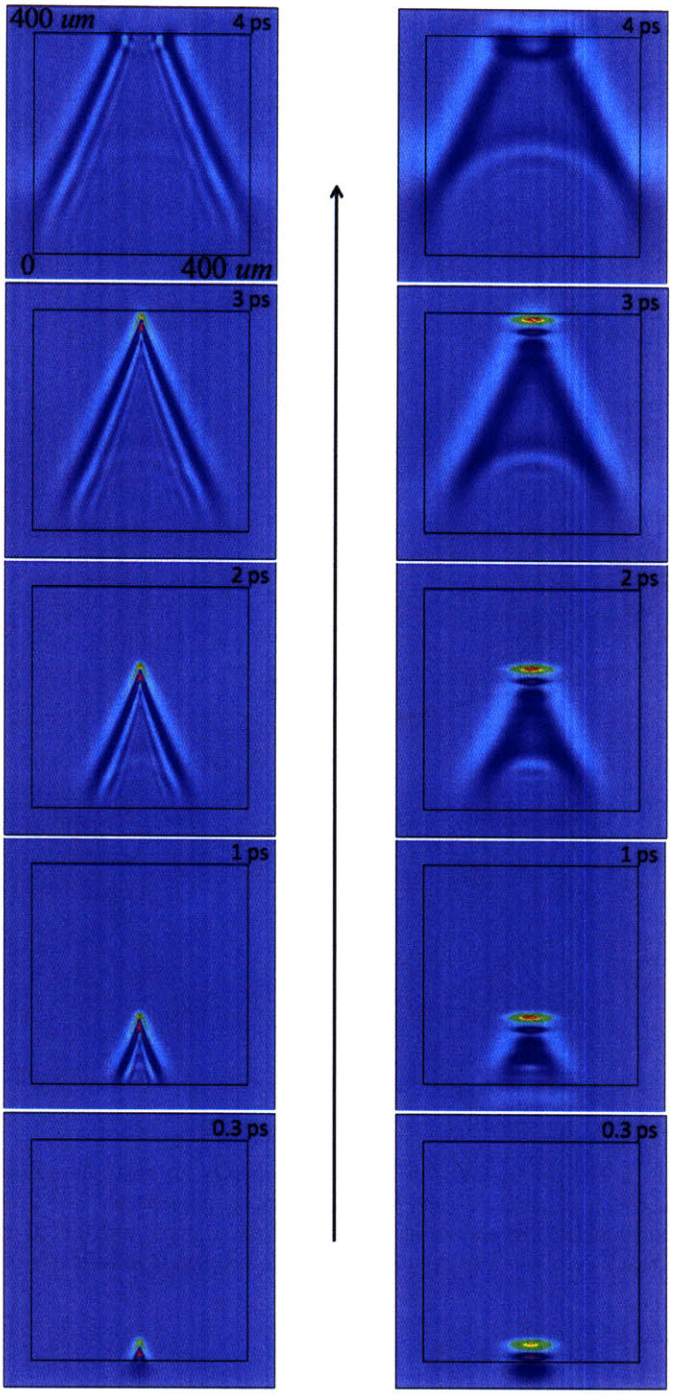


Figure 4-3: Two dimensional plots of the top view plane where the crystal optical axis is pointing out of the plane. The 800 $nm$ pump laser with line width or the spot size of 5 $\mu m$ (a) and 50 $\mu m$ (b), and time duration 50 $fs$, are used to excite the broadband polariton wave. The evolution over time in each case are characterized.

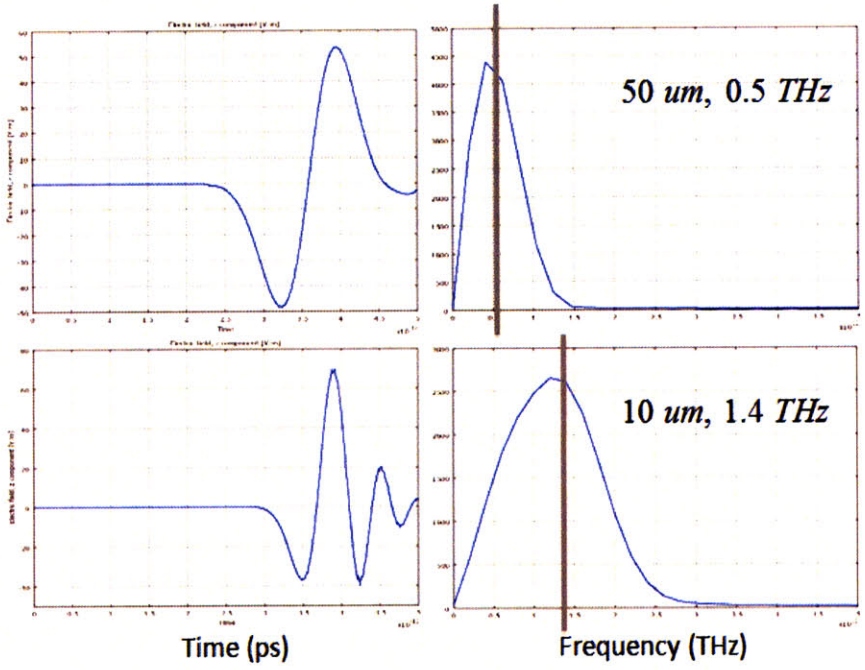


Figure 4-4: Broadband polariton profile in both time and frequency domains. The 50 $fs$, 800 $nm$ pump laser pulse with spot size of 10 $\mu m$ and 50 $\mu m$ is used to excite the polariton wave packet.

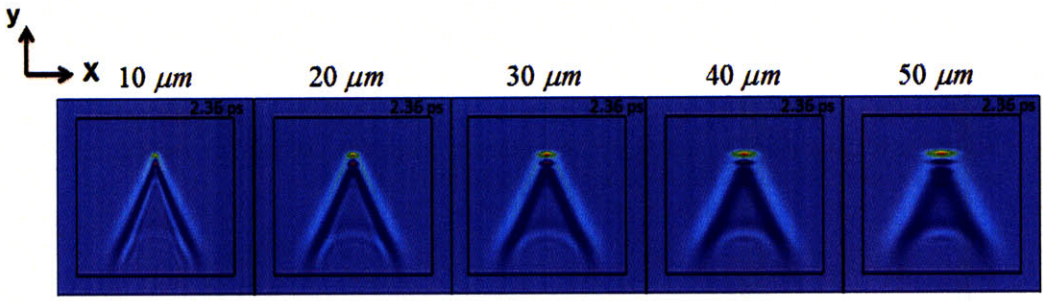


Figure 4-5: Two dimensional plots of the top view plane where the crystal optical axis is pointing out of the plane. The 50 $fs$, 800 $nm$ pump laser with spot size of 10 $\mu m$, 20 $\mu m$, 30 $\mu m$, 40 $\mu m$ and 50 $\mu m$ are used to excite the broadband polariton wave respectively. The snapshots are all at 2.36 $ps$.

The above tunability in Figure 4-5 could be formulated as,

$$\lambda_{center} = w_0 = \frac{4\lambda F}{\pi D} \tag{4.1}$$

where F is the focal length of the lens, D the diameter of the spot incident on the lens, $\lambda$ the wavelength of the pump light (in this case 800 nm), and $\lambda_{center}$ is the central wavelength of the generated polariton wavepacket. More results showing this effect are in Figure 4-6. This tunability is a very useful tool of polariton waveform control, which will be presented from different point of views in Chapter 5 and Chapter 6 as well.

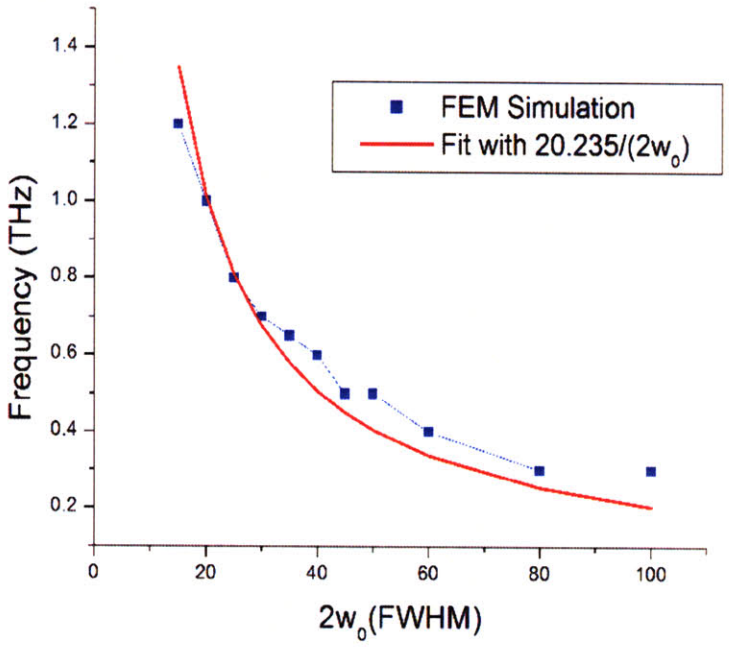


Figure 4-6: The central frequency of the terahertz waveform depends inversely on the excitation beam spot size. Shown here are the simulated and fitted results.

### 4.2.2 Front View Plane

The Z dimension of phonon-polariton generation and propagation from the front view plane, or the Z-X plane, is trivial for a cylindrically focused line beam, as shown in Figure 4-7. The polariton polarization is along the optical axis. As indicated before,

lateral propagation greatly benefits polariton detection, which can be implemented with another probe beam around or far away from the excitation region. This plane is also the view when the polariton imaging technique is applied.

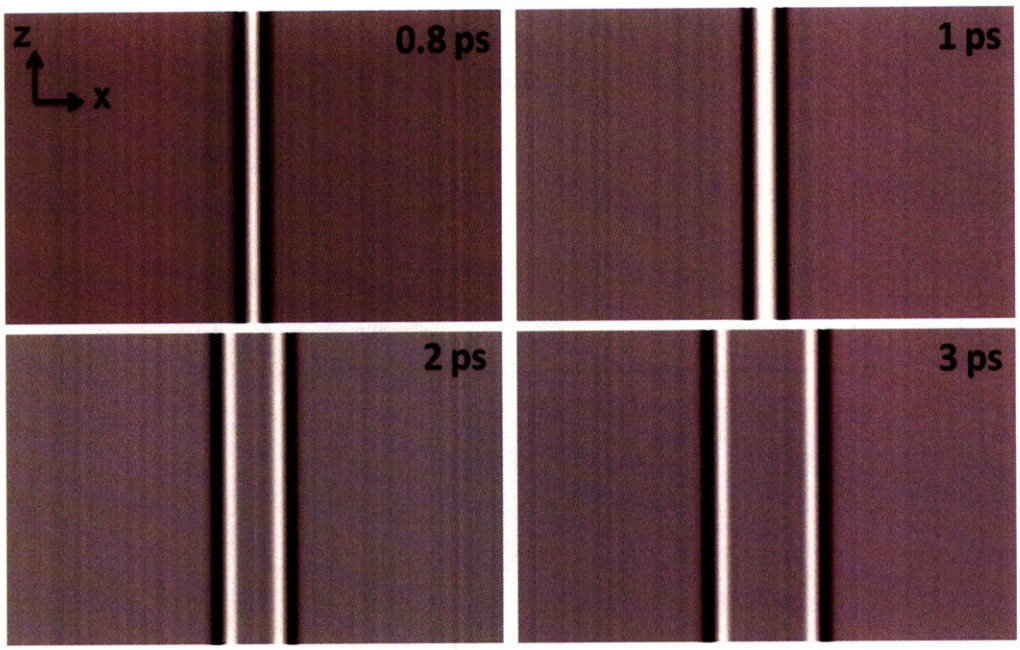


Figure 4-7: Two dimensional simulation plots of the front view plane where the crystal optical axis Z is pointing up. The 50 $fs$, 800 $nm$ pump laser with spot size 30 $\mu m$ is used to excite the broadband polariton wave.

This plane is characterized by its anisotropy. The dielectric tensor $\epsilon_{xx}(w) = \epsilon_{yy}(w) = \epsilon_{\perp}(w)$ and $\epsilon_{zz}(w) = \epsilon_{\parallel}(w)$, where the $\perp$ and $\parallel$ stand for directions perpendicular and parallel to the optic axis Z. Many interesting phenomena could happen from the view of this plane. if there is a certain structure in the $LiNbO_3$ medium, such as a curved structure, through which field amplification will be presented in Chapter 6; or with different excitation schemes, such as a round spot or ring excitation, which is in the following.

To initially demonstrate the anisotropy, a tightly focused round spot with radius 30 $\mu m$ could be used to excite the phonon-polariton response. The wave propagates faster in the horizontal direction than in the vertical dimension with speed ratio $6.46 : 5.11$, since $n_o = 5.11$ and $n_e = 6.46$. Also, the polariton wave pattern is more or less similar to dipole radiation, where the intensity is strongest in the horizontal

direction while gradually decreasing to zero in the vertical direction. Furthermore, round spot excitation with radius 300 $\mu m$ is also shown in Figure 4-9. It is amazing to see that when the line width is set as 30 $\mu m$, the near single-cycle feature of the polariton wave is again clearly demonstrated.

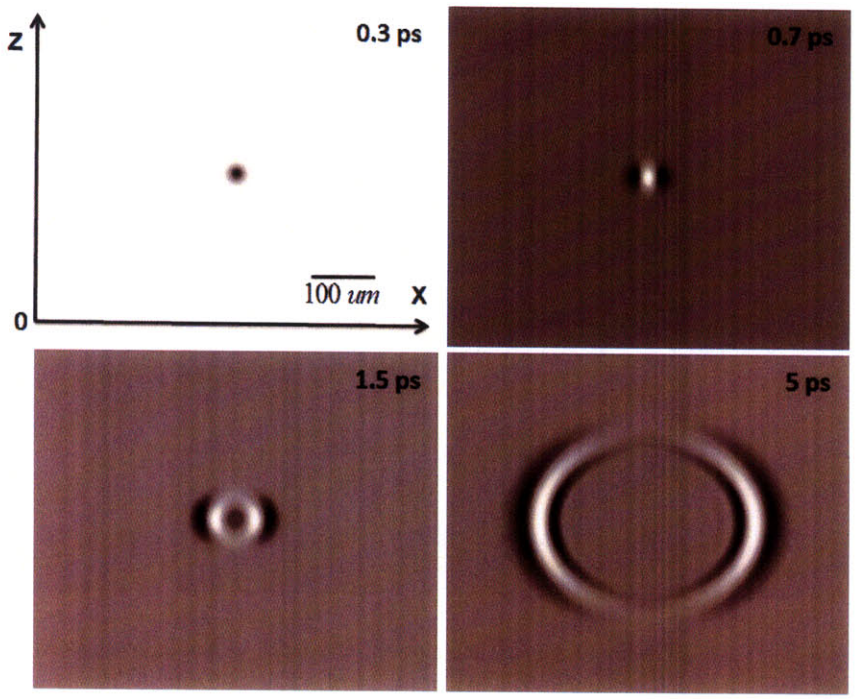


Figure 4-8: Two dimensional simulation plots of the front view plane where the crystal optical axis Z is pointing vertically. The 50 $fs$, 800 $nm$ pump laser tightly focused to a spot with radius 30 $\mu m$ was used to excite the polariton wave.

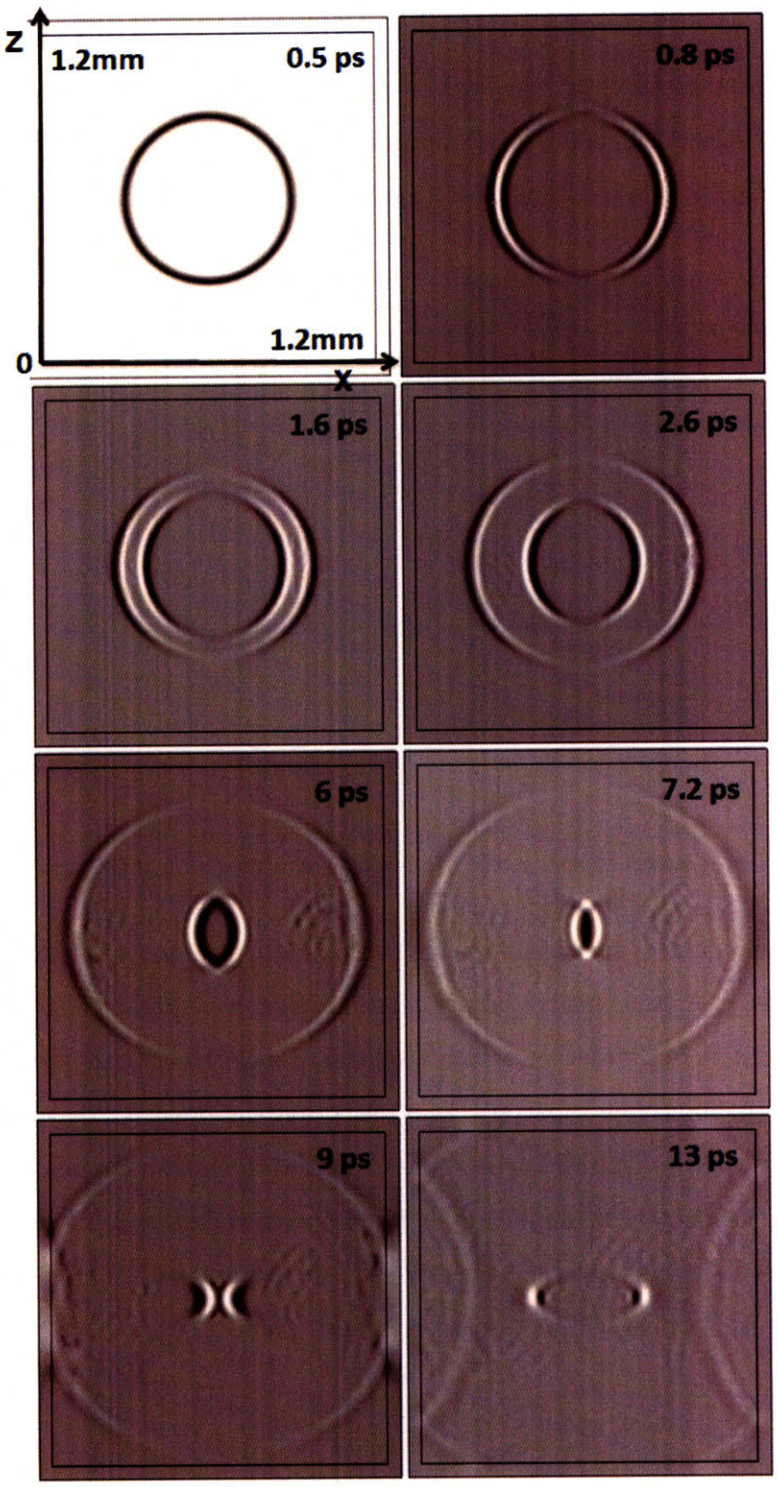


Figure 4-9: Two dimensional simulation plots of the front view plane where the crystal optic axis Z is pointing vertically. The round ring with radius 300 $\mu m$ from a 50 $fs$, 800 $nm$ pump laser was used to excite the polariton wave.

## 4.3 Narrowband Excitation

A narrowband polariton wave can be achieved by spatial shaping, temporal shaping or spatial-temporal shaping. Temporal shaping can be achieved through excitation pulse trains with a constant repetition rate, as shown in Figure 4-10.

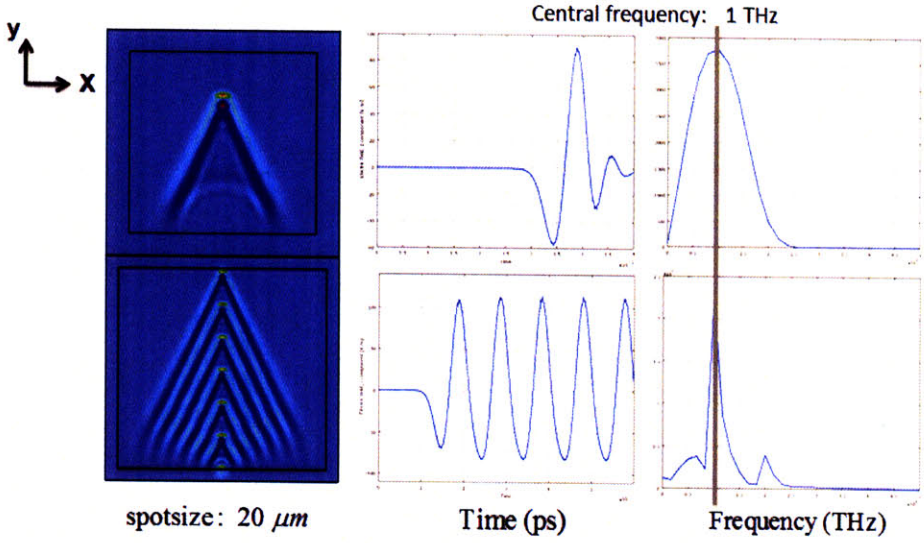


Figure 4-10: Two dimensional simulation plots of the temporal shaping via pulse train with 1 ps interval. The spotsize is 20um, so the bandwidth is narrowed around the central 1THz

One example of spatial shaping is the crossed beam excitation scheme as shown in Figure 4-11. A transmissive binary phase mask can be designed to primarily diffract the $\pm 1$ orders of diffraction, which are focused into the crystal through the telescope to form the interference pattern. It is clear that the polariton wavelength is strongly dependent on the grating wavelength, which is tunable by changing the crossing angle between the two excitation beams. This laser induced grating has been used to excite coherent optic and acoustic waves as early as 1980s [115, 116, 117] in thin medium, the details of which will be discussed in next chapter.

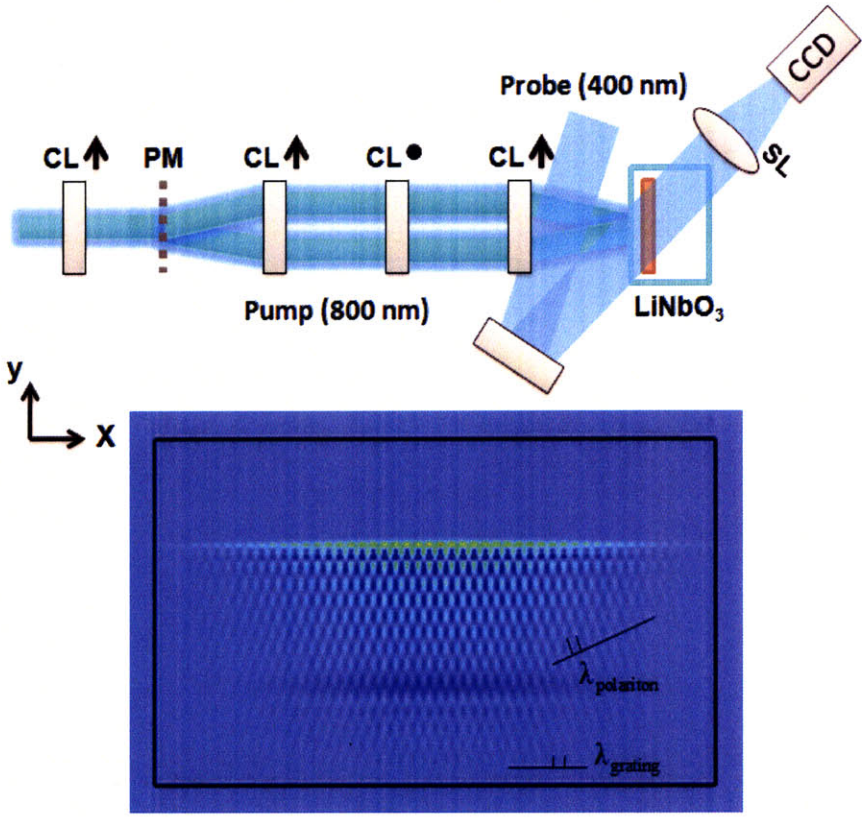


Figure 4-11: Illustration of the spatial shaping via two crossed beam excitation.

# Chapter 5

# Phonon-Polaritons in Thin Ferroelectric Crystals

When the crystal thickness $d$ is gradually decreased from the bulk regime (usually $d > 500\ \mu m$) to the waveguide regime (usually $d < 100\ \mu m$), polariton generation and propagation should be increasingly influenced by the interference of confined waves, and it takes a shorter time for the polariton wave originally propagating according to the bulk dispersion properties at the very beginning of the generation process to turn to follow the rules intrinsic to the confined geometry. This two-fold evolution of the transition and the unique phenomena in the waveguide regime will be characterized in this chapter. Following that, polariton coherent control via different excitation schemes will be discussed.

## 5.1 Theory of Dielectric Waveguide

A simple dielectric waveguide structure is illustrated in Figure 5-1, which is characterized by a slab dielectric core of thickness $d$ with refractive index $n_1$ surrounded by cladding of lower refractive index $n_2$. As is well known in guided wave optics, if the incident angle $\theta_1'$ is smaller than the critical angle $\theta_c$, waves will be partially transmitted into the cladding at each reflection, thus will vanish over a certain amount of distance; but if $\theta_1 > \theta_c$, waves will undergo total internal reflection at the boundaries

and propagate down the waveguide with little loss from damping and absorption of the materials.

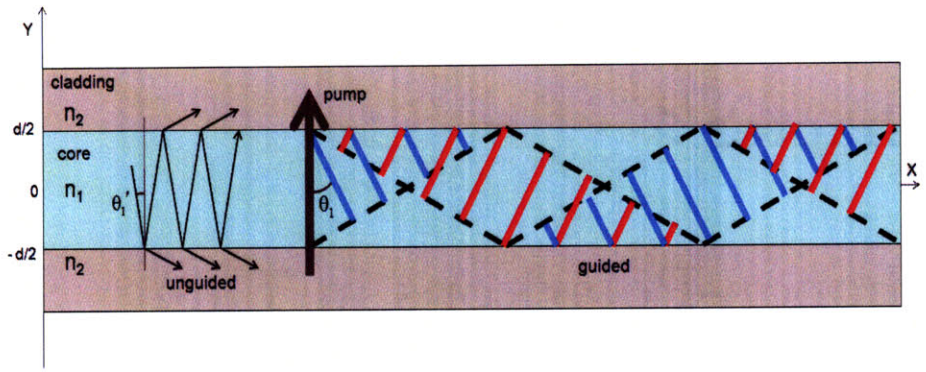


Figure 5-1: Illustration of a high-dielectric-waveguide and total internal reflection of the polariton wave with line excitation.

For the high-dielectric-contrast uniaxial $LiNbO_3$ waveguide in this thesis, the optic axis Z is pointing out of the plane as in Figure 5-1, which makes the core an optically isotropic media for in-plane waves, and the cladding is air. For the phonon-polariton wave with the same cylindrically focused line excitation as in the bulk case, the refraction index in this case is 5.11 since the polariton frequency content is between 0 and 3 THz, which makes the critical angle $11.3^0$, smaller than the cherenkov angle typical in this plane. Since the electric field of the polariton wave is pointing out of the plane, this geometry will make a perfect TE dielectric waveguide.

### 5.1.1 Multi-mode Behavior

There are many ways to analytically solve the eigenmodes in the dielectric slab waveguide. Here we define the wavevector $k = (k_x, k_y, k_z)$ in the dielectric medium, where $k_z$ is 0, and $k_x$ is the propagation constant $\beta$. For a TE waveguide, the perfect waveguide solutions are assumed as,

$$E_z(x, y, t) = E_z(y)e^{i(k_x x - wt)}\hat{z} \tag{5.1}$$

$$H_y(x, y, t) = H_y(y)e^{i(k_x x - wt)}\hat{y} \tag{5.2}$$

$$H_x(x, y, t) = H_x(y)e^{i(k_x x - wt)}\hat{x} \tag{5.3}$$

so the Helmholtz equation $(\nabla^2 + n^2k^2)E_z(x,y) = 0$ becomes,

$$(\frac{\partial^2}{\partial y^2} + \frac{w^2\epsilon_r}{c^2} - k_x^2)E_z(y) = 0 \tag{5.4}$$

or given that the fields have to be zero at infinity,

$$(\frac{\partial^2}{\partial y^2} + k_y^2)E_z(y) = 0, \quad |y| < d/2 \tag{5.5}$$

$$(\frac{\partial^2}{\partial y^2} - \gamma_y^2)E_z(y) = 0, \quad |y| > d/2 \tag{5.6}$$

where $k_y$ and $\gamma_y$ are real positive numbers. So the field pattern is,

$$E_z(y) = \begin{cases} E_0 \cos k_y y, & |y| < d/2, \text{ symmetric mode;} \\ E_0 \cos(k_y y - \frac{\pi}{2}), & |y| < d/2, \text{ antisymmetric mode;} \\ E_0 e^{\pm\gamma_y y}, & |y| > d/2. \end{cases} \tag{5.7}$$

The fields themselves and their first derivative with respect to $y$ are continuous at the boundaries, which lead to

$$\tan(k_y\frac{d}{2}) = \frac{\gamma_y}{k_y}, \quad \tan(k_y\frac{d}{2} - \frac{\pi}{2})) = \frac{\gamma_y}{k_y} \tag{5.8}$$

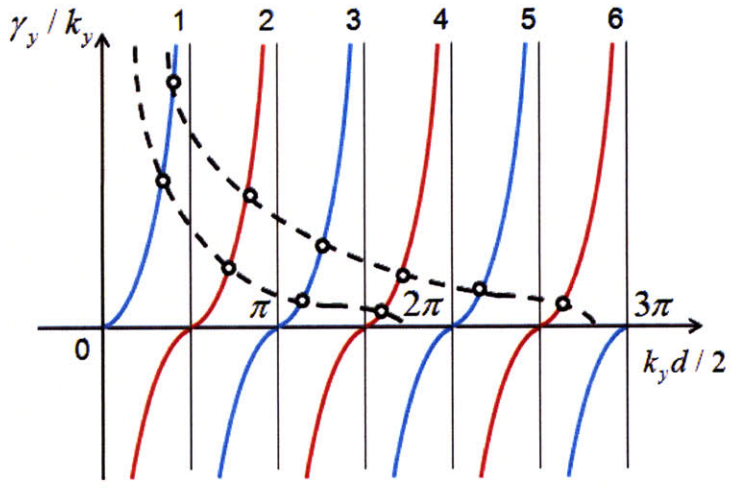


Figure 5-2: Intuitive solutions of the symmetric and antisymmetric modes in dielectric waveguide.

Taking into account the assumption in writing equations (5.5) and (5.6),

$$k_x^2 - \gamma_y^2 = \frac{w^2}{c^2}, \quad k_x^2 + k_y^2 = \frac{w^2 \epsilon_r}{c^2} \tag{5.9}$$

so

$$\frac{\gamma_y}{k_y} = \sqrt{\frac{\omega^2(\epsilon_r - 1)}{c^2 k_y^2} - 1} \tag{5.10}$$

### 5.1.2 Phase Shift

The reflection and transmission coefficients can be expressed with the angle of incidence $\theta_1$ and the angle of refraction $\theta_2$,

$$r = \frac{n_1 \cos\theta_1 - n_2 \cos\theta_2}{n_1 \cos\theta_1 + n_2 \cos\theta_2}, \quad t = 1 + r \tag{5.11}$$

and the phase shift is,

$$\tan\frac{\varphi}{2} = \sqrt{\frac{\cos^2\theta_1}{\cos^2\theta_c} - 1} \tag{5.12}$$

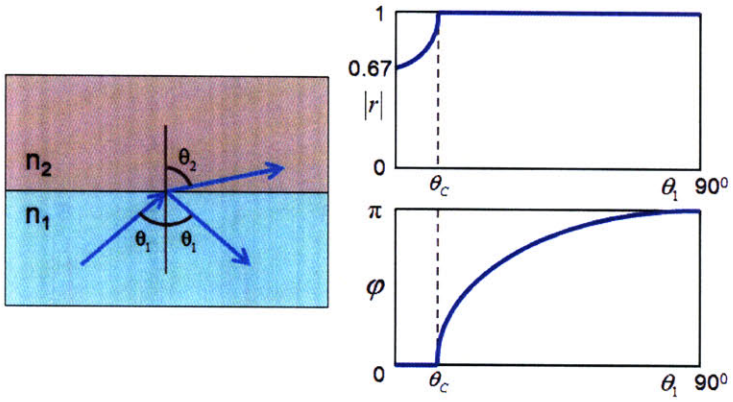


Figure 5-3: Reflection coefficient and phase shift in the internal reflection of a $LiNbO_3$ waveguide.

### 5.1.3 Field Distribution

The transcendental equation solutions could be intuitively illustrated as in Figure 5-2. The crossing points in the blue curves and red curves stand for the symmetric and antisymmetric solutions respectively, and each point corresponds to a mode. From

(5.10), when freqency $\omega$ is decreasing, $\gamma_y/k_y$ will move towards the origin, and the number of crossing points, or the number of modes will decrease accordingly, which means all the higher order modes have a cutoff frequency. There is always a dominant mode though, which is the lowest symmetry type. This mode can remains when the dielectric slab is sufficiently thin.

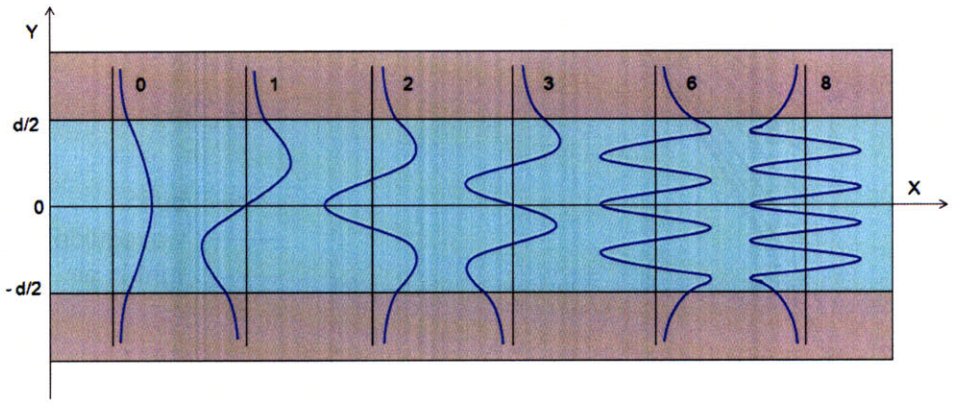


Figure 5-4: The field distribution of TE dielectric waveguide modes characterized by the harmonic patterns in the core and evanescent waves extending into the surrounding medium.

The field distributions of these modes are characterized by the evanescent part in the cladding, which decreases exponentially into the lower index medium, and the harmonic wave with certain symmetry type in the core, as sketched in Figure 5-4. Note that the field is continuous and not zero at the boundaries.

### 5.1.4 Dispersion Relation

The calculated dispersion relation and effective index for a phonon-polariton wave in a bulk crystal and the multi-mode 50 $\mu m$ and 10 $\mu m$ waveguides are shown in Figures 5-5, 5-6, 5-7 and 5-8, taking into account the transcendental equations (5.8) and (5.10). All the waveguide modes lie between the curve of a bulk crystal and the curve of light propagation in a homogeneous lower index surrounding medium, which is air in this thesis.

The effective index is defined as $ck/\omega$. Its dispersion curves indicate that different modes have different velocities, which results in the effect that an original wave packet will spread in time and space and different modes will separate with each other. This

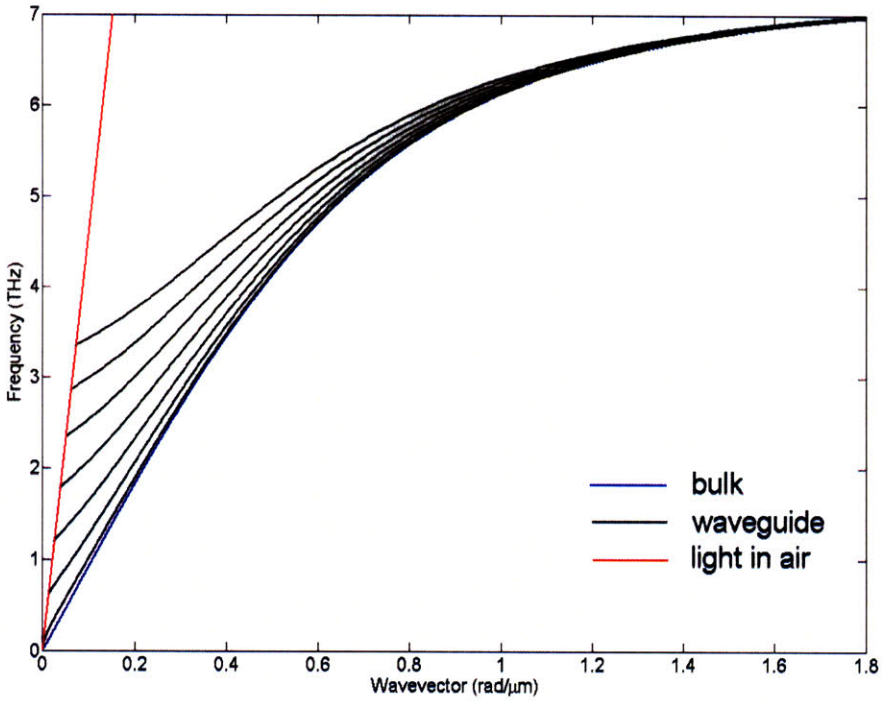


Figure 5-5: Dispersion curves of a 50 $\mu m$ $LiNbO_3$ waveguide, where the first seven modes are ploted.

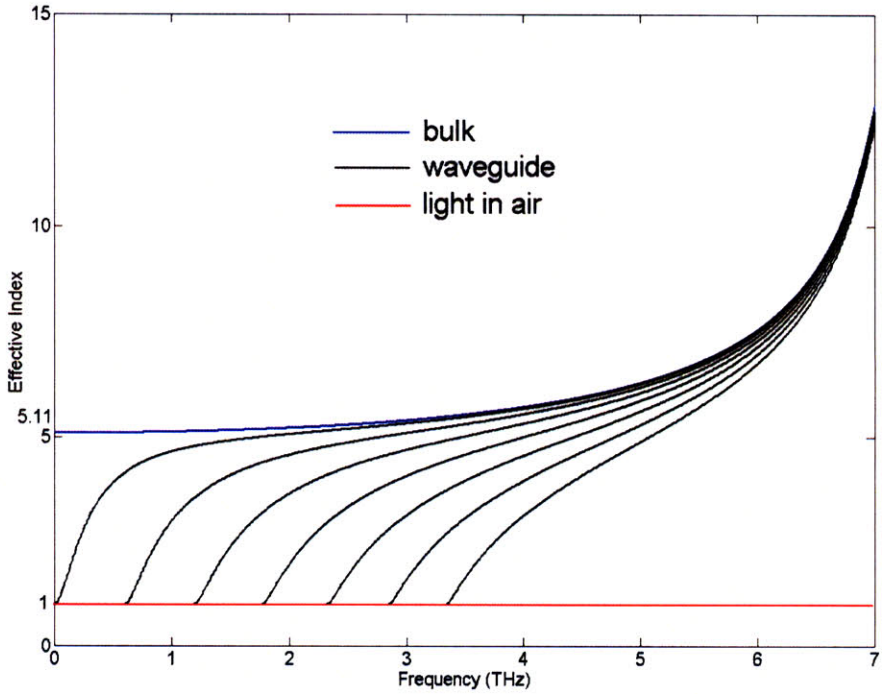


Figure 5-6: Effective index of the first seven modes of a 50 $\mu m$ $LiNbO_3$ waveguide.

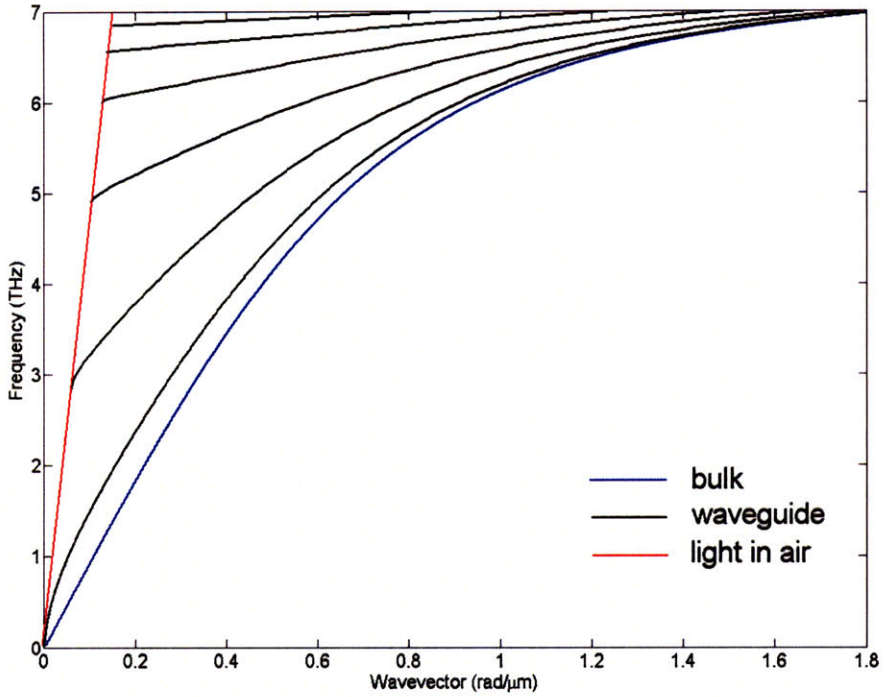


Figure 5-7: Dispersion curves of a 10 $\mu m$ $LiNbO_3$ waveguide, where the first six modes are ploted.

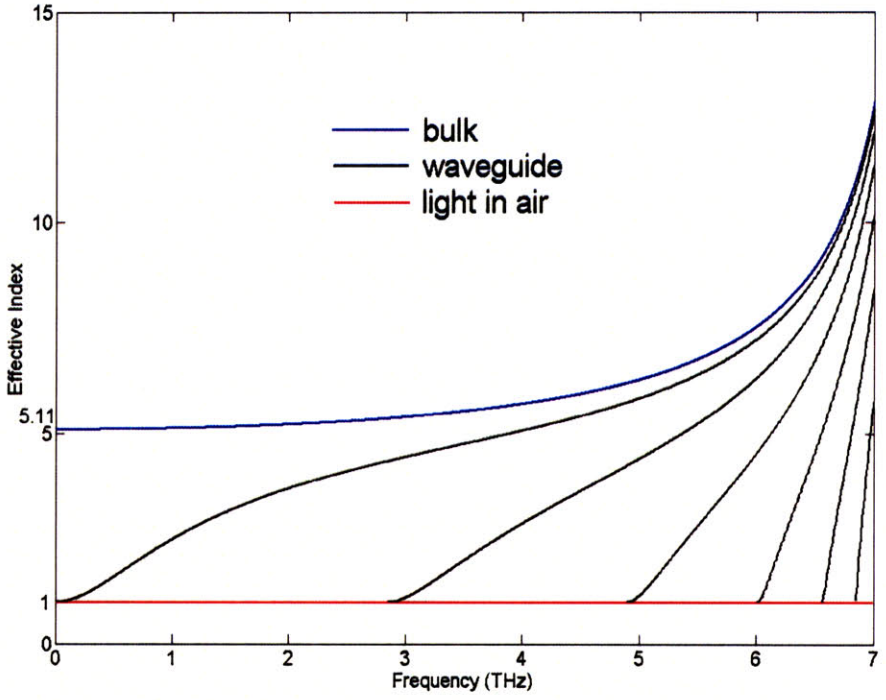


Figure 5-8: Effective index of the first six modes of a 10 $\mu m$ $LiNbO_3$ waveguide.

is modal dispersion. At the same time, the curve of any specific mode is not a straight line, which means the wave packet of any mode itself will spread in time and space as well, which is the group velocity dispersion. In multi-mode waveguides, modal dispersion is more significant than the group velocity dispersion, and the difference is more significant in thinner waveguides, as shown in the dispersion figures.

## 5.2 Transition to the Waveguide Regime

From the derivation of the dielectric waveguide analytical multi-mode solutions, it was assumed that the electric field distributions of all modes are spatially harmonic with different symmetry and degeneracy along the vertical dimension, and temporally harmonic along the propagation direction with planar wave fronts. This multi-mode behavior is intrinsic to the geometrical confinement in one dimension regardless of the excitation scheme and the wave propagating in the crystal. When it comes to the line excitation scheme as shown in Figure 5-1, it is the interference between the waves bouncing back and forth that directly form the waveguide multi-mode behavior.

As mentioned before, the transition has a *two-fold* meaning for the line excitation scheme in this thesis. On one hand, as the crystal thickness $d$ is gradually decreased from the bulk regime (usually $d > 500\ \mu m$) to waveguide regime (usually $d < 100\ \mu m$), the eventual angle between the wave front and vertical line over infinite time and distance is decreased from the cherenkov angle, which is a signature of the bulk, to zero, which is the signature of a multi-mode waveguide. On the other hand, in a specific dielectric crystal with a certain thickness, the phonon-polariton wave experiences the transition from the initial cherenkov-like pattern, which is a signature of the bulk regime, to the straightened multi-mode pattern of different symmetry and degeneracy, which is a signature of the waveguide regime, over a certain amount of time, distance, modal and group velocity dispersion. The time and distance it takes for the polariton wave to eventually reach the gradually straightened multi-mode pattern becomes shorter with longer polariton wavelength or in a thinner crystal. In this section, the first kind of transition over crystal thickness, and the second of

transition over propagation time and distance will be characterized.

### 5.2.1 Transition over Crystal Thickness

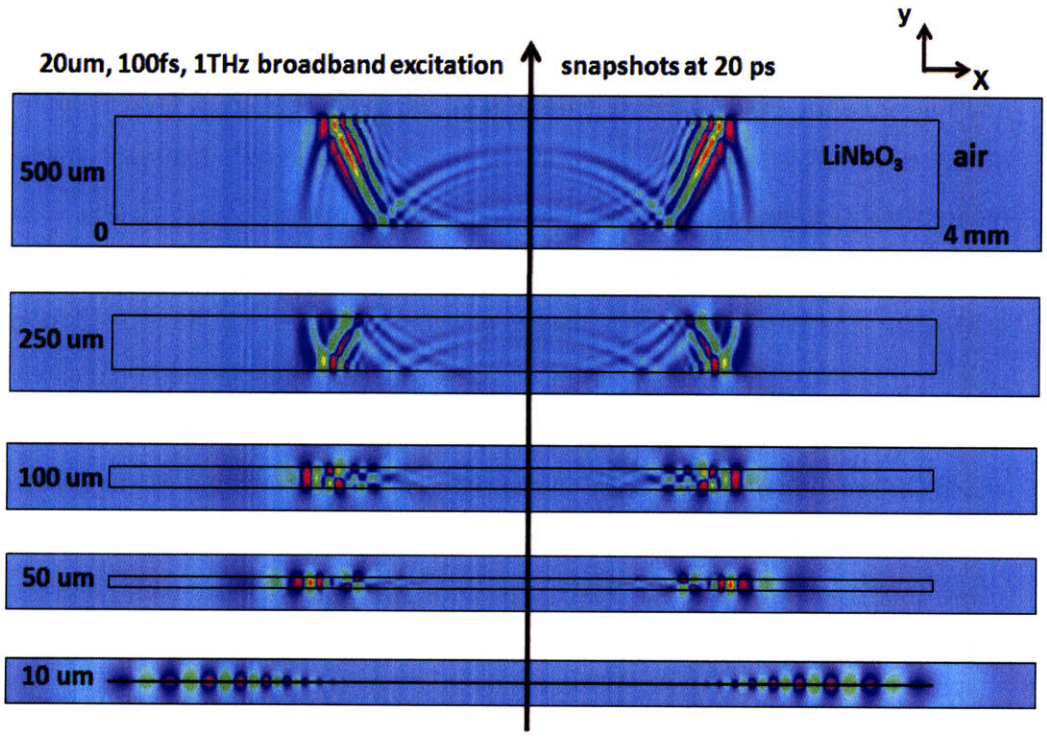


Figure 5-9: Transition over crystal thickness.

The transition over crystal thickness is shown in Figure 5-9, in which the geometry and the excitation scheme is the same as in Figure 5-1. The crystals are excited with the same 20 $\mu m$ cylindrically focused line beam, which results in 1 THz broadband phonon polaritons, as demonstrated in the bulk case, and the snapshots are all taken at 20 $ps$. In the 500 $\mu m$ $LiNbO_3$ crystal, the polariton wave experienced two bounces after the optical excitation pulse went through the crystal. The interference between the waves bouncing back and forth can be seen, but it has little effect on the lateral wave propagation due to the long distance between bounces. It is predictable that over infinite time and distance, the eventual angle between the wave front and the crystal plane will not deviate much from the cherenkov angle before the polariton

wave vanishes due to the damping in the crystal. In this case, no signature of the waveguide regime is observed.

In the other extreme the 10 $\mu m$ crystal, the polariton wave got quickly straightened out and all the cycles are propagating laterally after the countless bounces and interference. It is hard to see any bounce and interference anymore, which is a strong evidence that the polariton wave is propagating with the perfect waveguide pattern and following the exact waveguide dispersion rules, where there is no remaining sign of any tiny bulk effect. The mode in the figure is the lowest dominant symmetric mode, which has no node between the boundaries.

In between the two extreme cases, in 100 $\mu m$ crystal for example, the interference is obvious, and part of the wave packet may be still bouncing, but the multi-mode behavior and straightened wavefront of every single observable mode indicates that the waveguide effect is significantly dominant. There are three observable modes, in which the one propagating fastest on the right is the lowest symmetric mode without node, in the middle is the lowest antisymmetric mode with one node on the crystal plane, and the slowest one is the second symmetric mode with two nodes between the boundaries.

The quantitative modal dispersion will be presented in the next section, but qualitatively several characteristics are already clear here.

- In the multi-mode dielectric waveguide, lower modes propagate faster, and the separation increases over time and distance, in agreement with waveguide analytical solutions.

- The modal dispersion is significantly stronger than the group velocity dispersion of each mode, since the modes are separated well over time but it is hard to see any shape change for each mode.

- For any single mode, more electric field will exist in the lower index medium surrounding the dielectric core in thiner crystals. This effect is strongly evident for the lowest symmetric mode.

### 5.2.2 Transition over Time and distance

Along with the transition to multi-mode behavior over time and distance as shown in Figures 5-10 and 5-11, two effects namely modal dispersion and group velocity dispersion will be discussed.

In the 100 $\mu m$ waveguide, even though there is a little deviation from the cherenkov angle, the polariton wave front is still tilted in the first 5 ps as shown in Figure 5-10, which means it is propagating as in bulk. At 10 ps, the first three modes start to separate from each other; the separation increases over time, and the polariton wave gradually turns to propagate in a more multi-mode way, which marks the end of the transition. The modal dispersion is very strong but the group velocity dispersion is hard to observe in this case.

In the 10 $\mu m$ waveguide shown in Figure 5-11, it takes much less time for the wave to propagate in a waveguide manner since the time interval between bounces is much shorter. Since the dominant mode forms quite early and there is only one mode in this waveguide, the effect of group velocity dispersion is very strong. According to the curves in Figure 5-7 and 5-8, the lower frequency part should propagate faster within any given mode. In the figure at 16.08 ps, it is obvious that the front cycles have lower frequency content and more electric fields extending into the surrounding air as far as several hundreds of microns, and those small cycles lagging behind have higher frequency content.

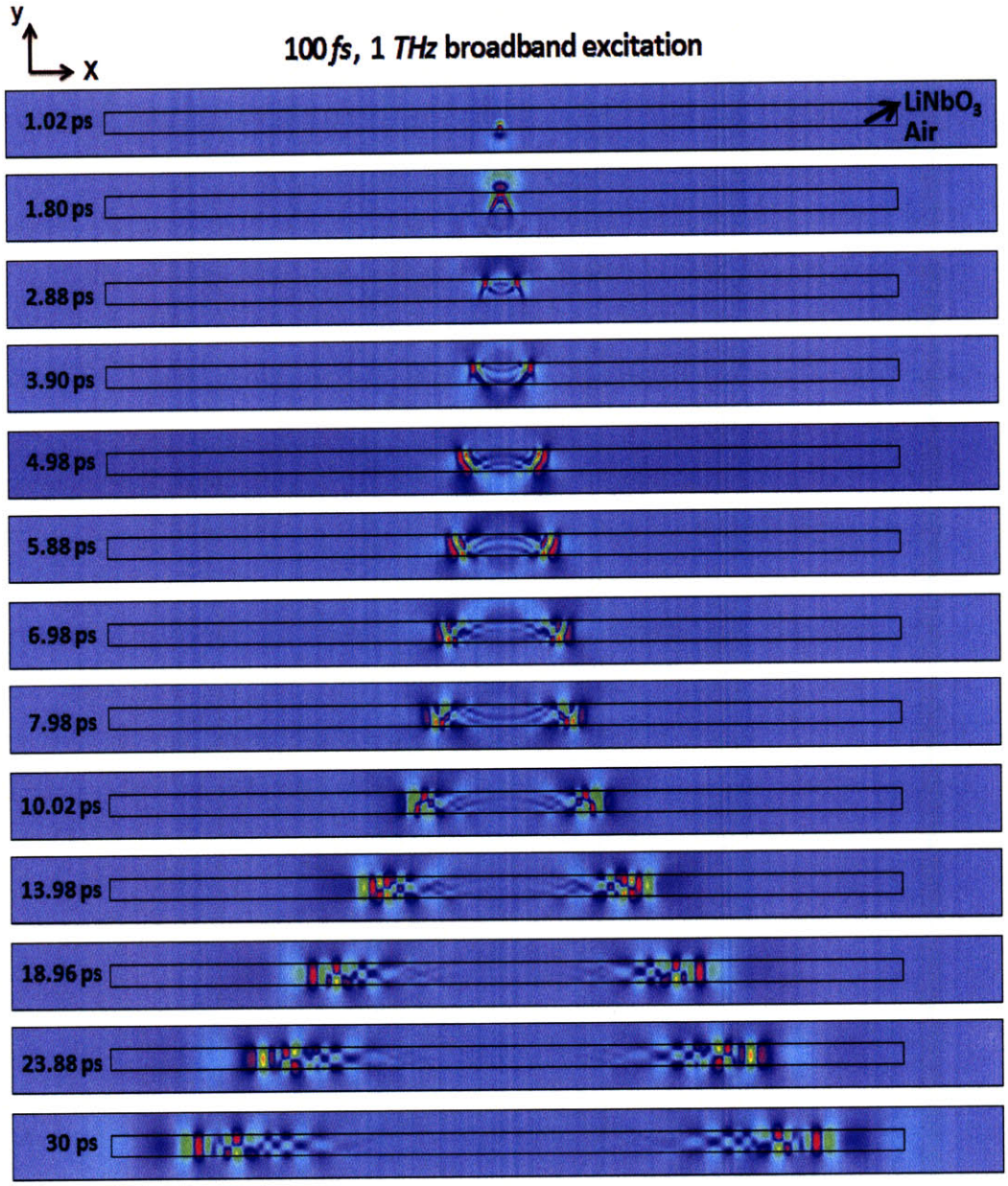


Figure 5-10: Transition over time and distance: modal dispersion.

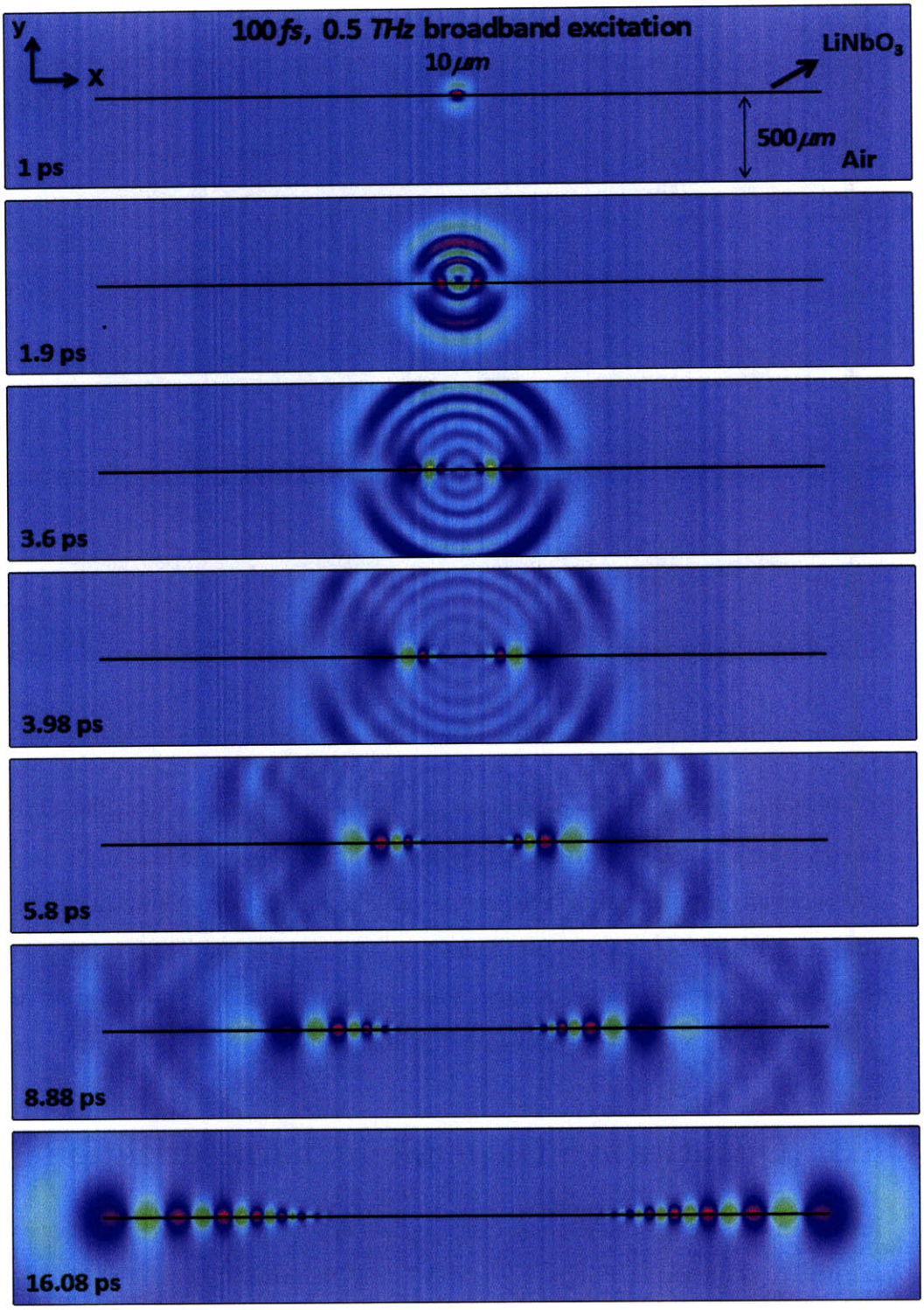


Figure 5-11: Transition over time and distance: group velocity dispersion.

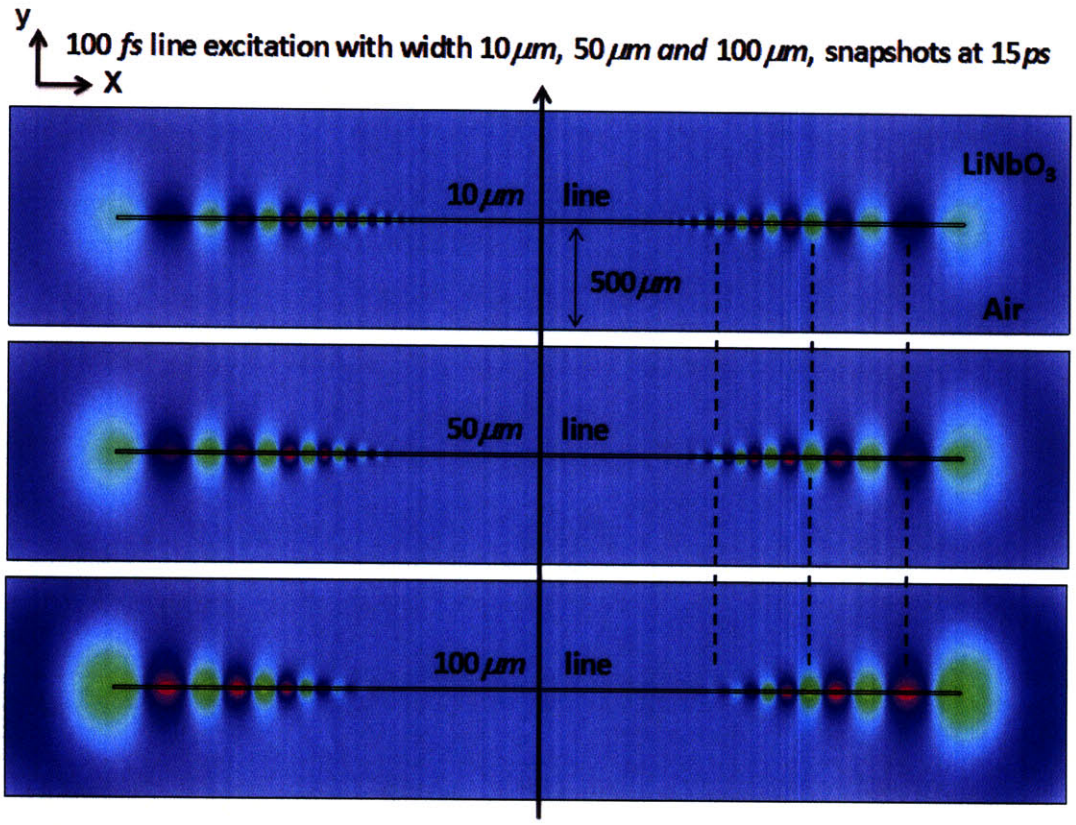


Figure 5-12: Transition over time and distance: line excitation tunability.

With line excitation, the polariton wave vector content can be varied by changing the line width as demonstrated in Chapter 4. In a 10 $\mu m$ waveguide as in Figure 5-12, this tunability can be qualitatively shown with snapshots taken at the same time 15ps after excitation. The 100 $\mu m$ line source excites a smaller wave vector range, while the 10 $\mu m$ line source excites a larger wave vector content. The quantitative results from the dispersion curves are presented in next section.

## 5.3 Quantitative Dispersion Characterization

In section 5.1, the theoretical dispersion curves of a dielectric waveguide have been calculated as shown in Figure 5-5 and 5-7. As indicated before, it is intrinsic to the geometric confinement regardless of the excitation scheme and the type of the wave propagating in the crystal. However, different excitation schemes do control the

intensity distribution or relative pump efficiencies among different modes and different wavevector content. These properties are characterized quantitatively in polaritonic and EM waveguides in the following.

### 5.3.1 Polaritonic Waveguide

For the polaritonic waveguide, the simulation dispersion curves and analytical solutions have been put on the same plots in Figures 5-13, 5-14, 5-15 and 5-16, in which the line excitation geometry is the same as in Figure 5-1 and the pulse duration is 100 $fs$. On the left of these figures are space-time plots, in which the time evolution of different modes can be directly observed, and on the right side are two-dimensional Fourier transformed dispersion curves, where the simulation can be compared with the analytical theory.

The waveguide mode change over the crystal thickness are shown in series 1-4, where the time dimension covers 10-80 $ps$, and the line width are all 100 $\mu m$ corresponding to broadband polariton wave with 0.3 THz central frequency. Several conclusions can be easily derived.

- The number of modes increases as the crystal thickness increases, and the intensity distribution moves up to higher modes accordingly.
- The mode velocity increases as the crystal thickness decreases. Taking the lowest symmetric mode for example, it takes ~60 $ps$ to travel 4 $mm$ in the 100 $\mu m$ crystal while it takes ~35 $ps$ in the 10 $\mu m$ case.
- The effect of modal dispersion becomes stronger as the crystal thickness decreases.

In series 5-8 and 9-12 with higher resolution, the time dimension covers 50-200 $ps$, and the crystal thicknesses are 200 $\mu m$ and 100 $\mu m$. As discussed before, the frequency and wave content of the polariton wave can be varied by the changing the line width in this excitation sheme. This effect can be directly seen in the figures: the smaller the line width, the broader wave vector range the optical beam can excite, and the higher the central frequency of the broadband polariton wave.

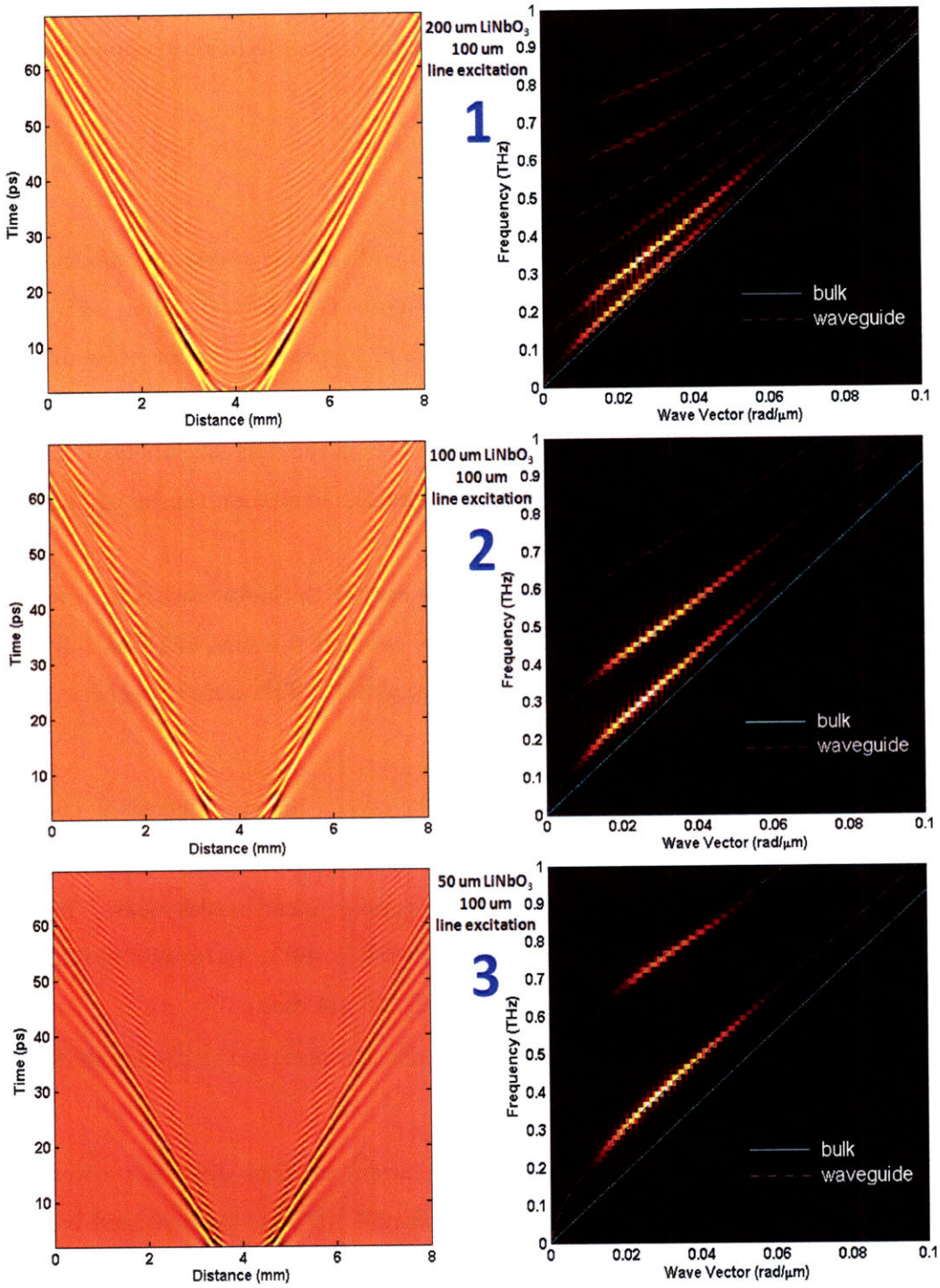


Figure 5-13: Space-time plots and dispersion curves for three crystal thickness with the same excitation width 100 $\mu m$. Waveguide multi-mode shifts over the crystal thickness are illustrated.

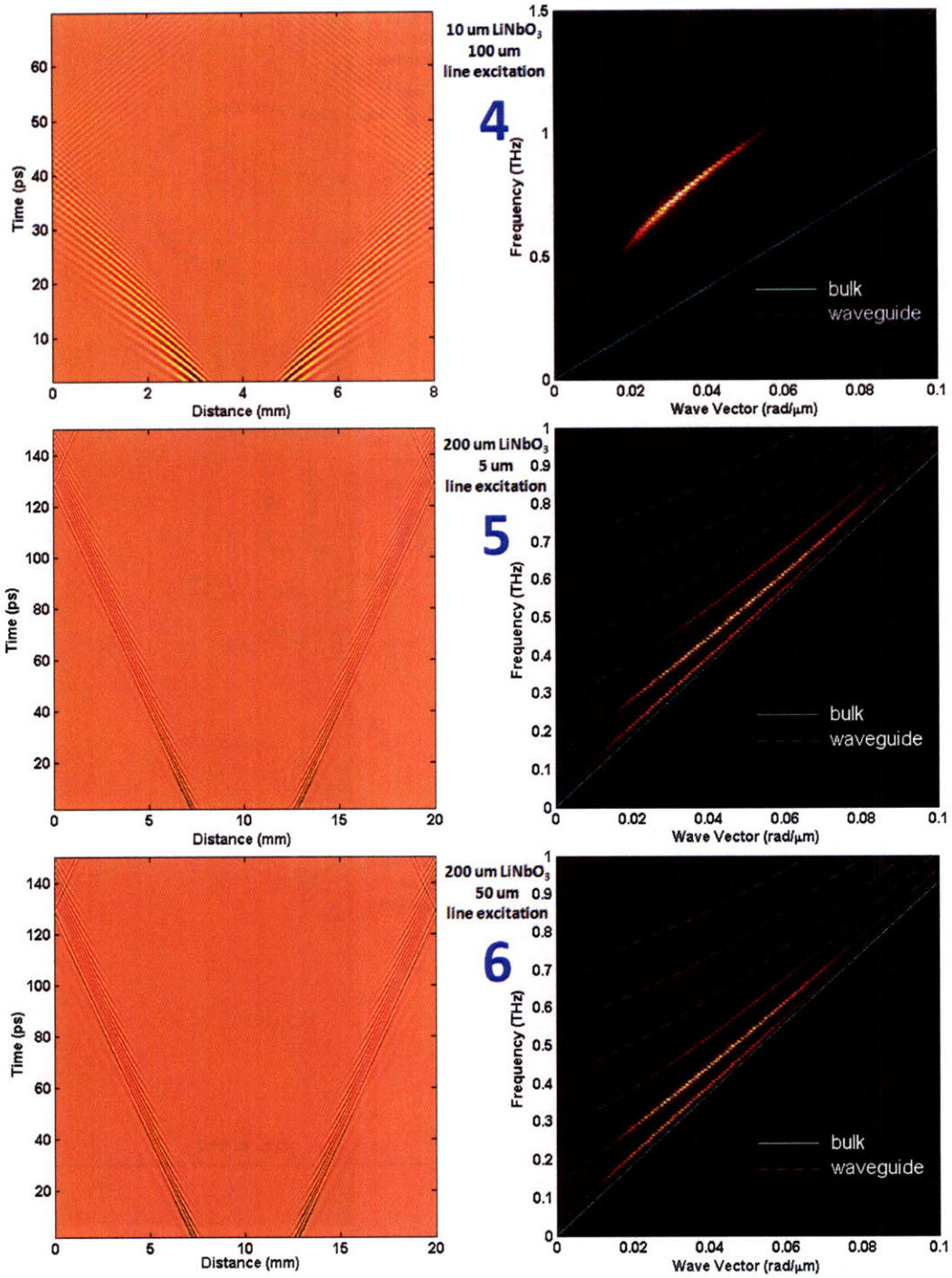


Figure 5-14: Space-time plots and dispersion curves in 200 $\mu m$ and 100 $\mu m$ $LiNbO_3$ waveguides. Polariton frequency and wave vector variation are achieved by changing the excitation line width.

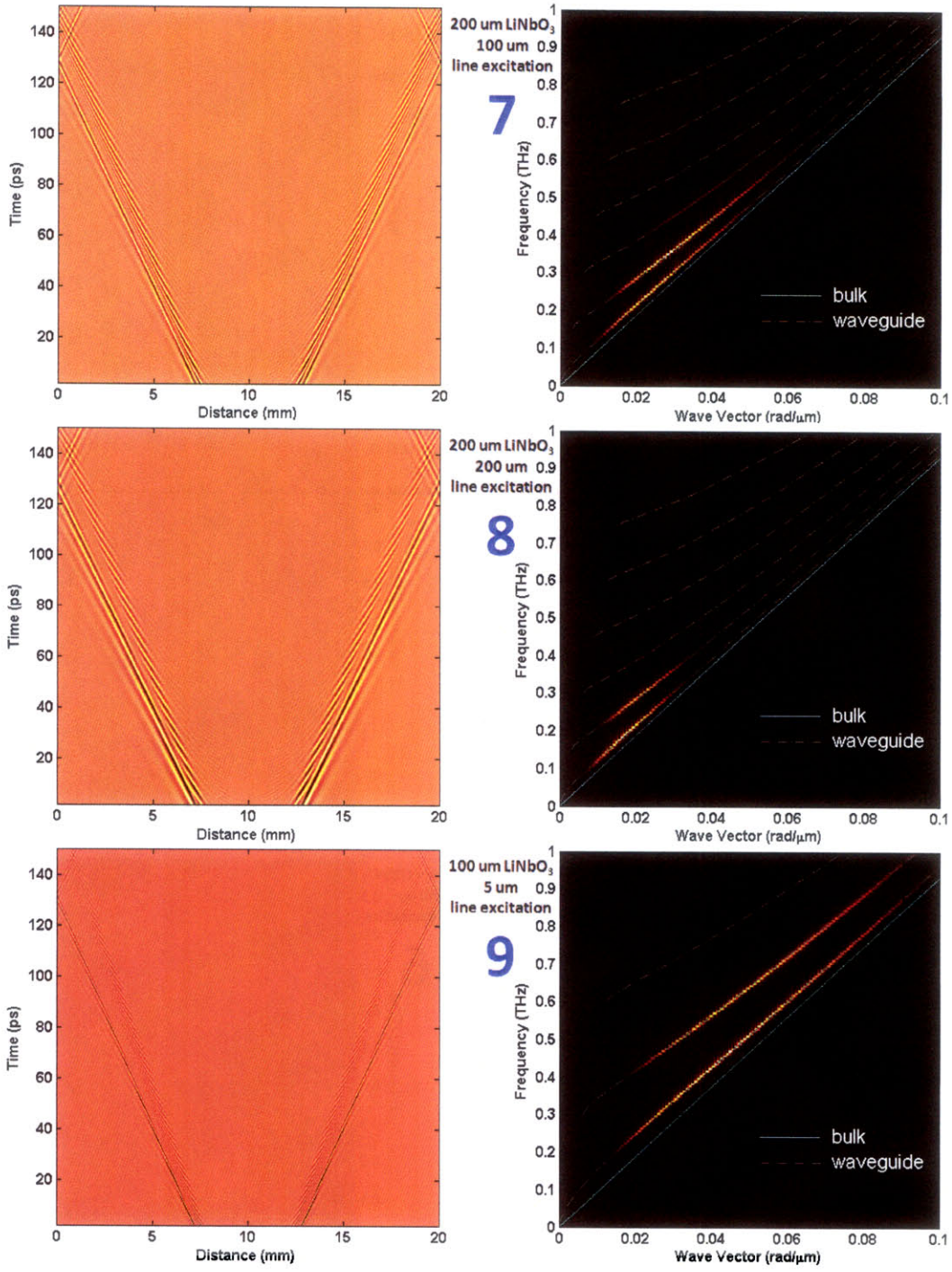


Figure 5-15: Space-time plots and dispersion curves in 200 $\mu m$ and 100 $\mu m$ $LiNbO_3$ waveguides. Polariton frequency and wave vector variation are achieved by changing excitaion line width.

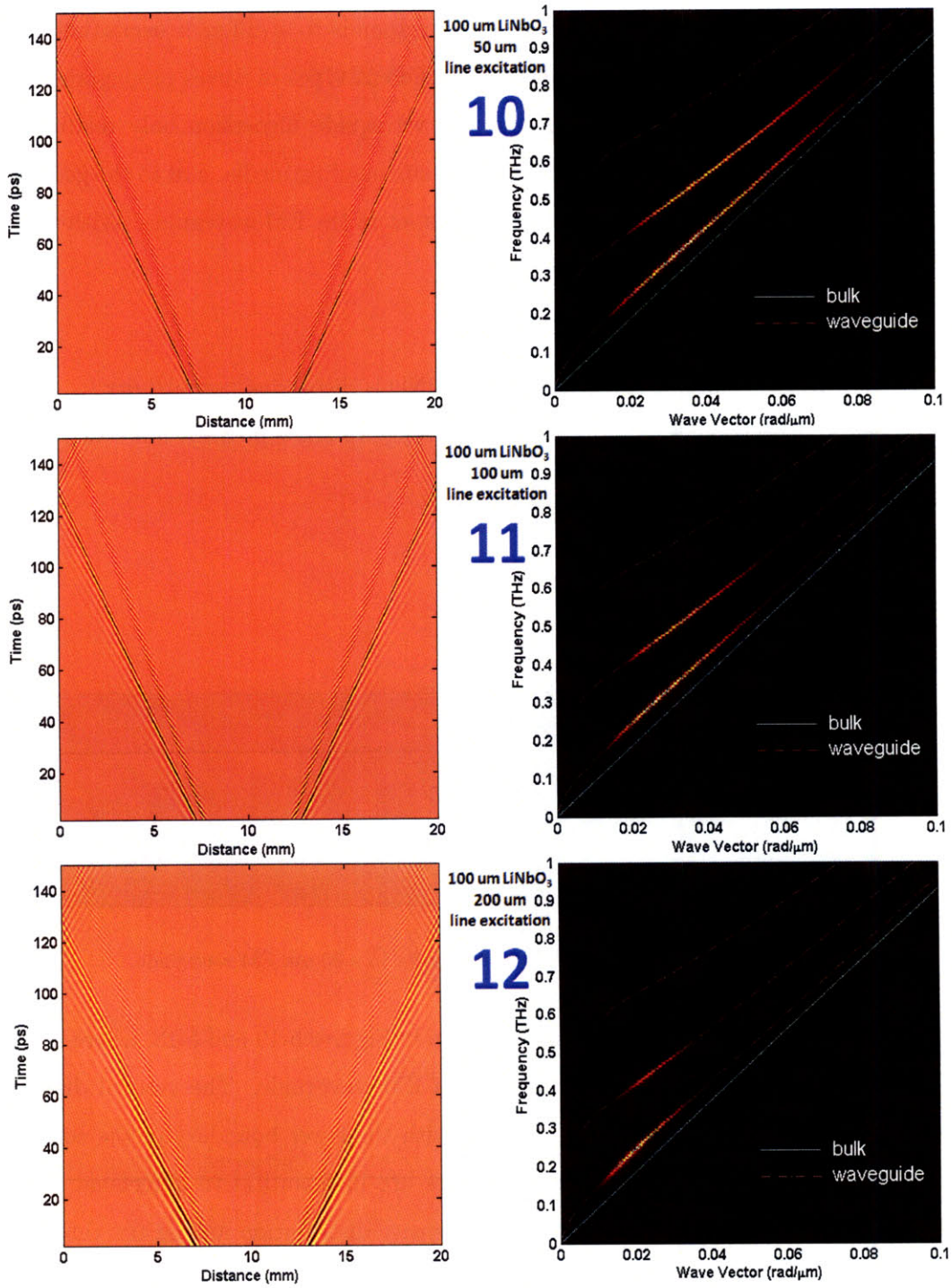


Figure 5-16: Space-time plots and dispersion curves in 200 $\mu m$ and 100 $\mu m$ $LiNbO_3$ waveguides. Polariton frequency and wave vector variation are achieved by changing the line width.

### 5.3.2 EM Waveguide

The purely electromagnetic waveguide corresponds to a different excitation scheme, different dispersive waveguide core, and different types of waves propagating inside. The purpose is to demonstrate that the waveguide dispersion only relates to the optical refractive index of the core and the surrounding media, and to the geometrical confinement, which are the only conditions set in the EM waveguide. With that, the following EM waveguide is assumed.

1. air cladding;
2. dielectric core, with the analytical $LiNbO_3$ dispersive permittivity;
3. excitation confined within a certain range to allow propagation over time.

and what are naturally not included are,

1. phonon contribution;
2. ISRS driving.

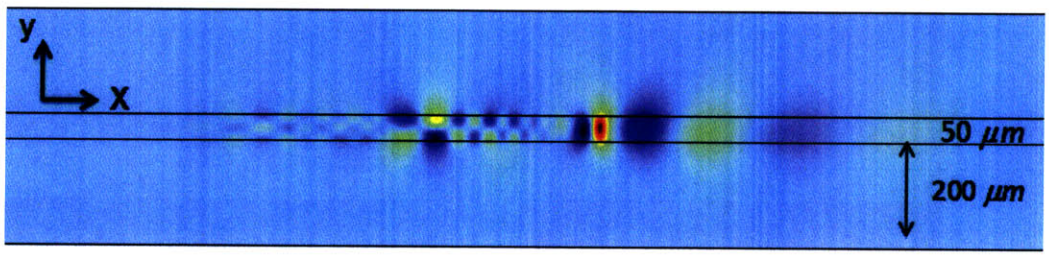


Figure 5-17: Multi-mode behavior in a 50 $\mu m$ EM waveguide.

The resulting field distribution is shown in Figures 5-19 and 5-18, where it is clear that there are three modes in this 50 $\mu m$ EM waveguide. The vertical distance in Figure 5-18 means the distance along y with the lower boundary of the core as the origin. The field patterns of these modes are in quantitative agreement with the analytical solutions here. In fact, the intensity distribution among the three modes should be different from the polaritonic waveguide due to the different excitation scheme, but the dispersion curve should be exactly the same, which is confirmed in Figure 5-19.

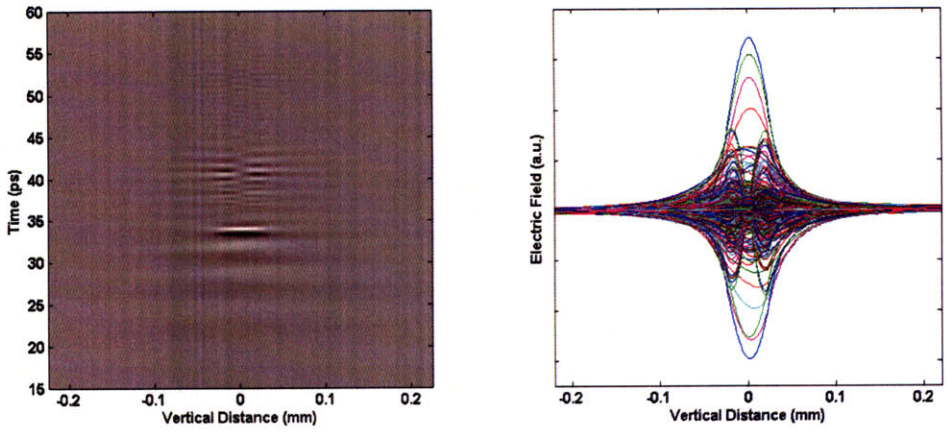


Figure 5-18: Field distribution in a 50 $\mu m$ EM waveguide and the surrounding medium.

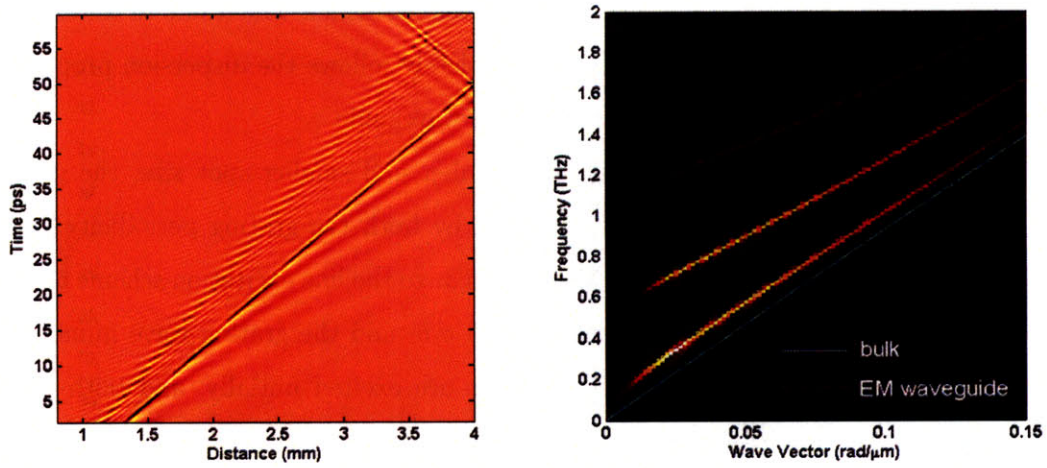


Figure 5-19: The space-time plot and dispersion curves of a 50 $\mu m$ EM waveguide, which is in agreement with analytical solutions while there is a little difference in the intensity distribution among the modes.

## 5.4 Narrowband Tunability

Laser induced grating by crossing two beams has been used to excite coherent optic and acoustic waves as early as 1980s [115, 116, 117]. The use of specially designed phase mask [67] and heterodyne detection [68] improved this traditional method. The intensity profile of a grating was assumed as a gaussian envelope modulated by squared sinusoid function. As shown in Figure 4-10, the grating wavelength can be tuned by changing the crossing angle between two excitation pulses. In this section, we present simulation results of laser induced grating excitation in a 33 $\mu m$ waveguide.

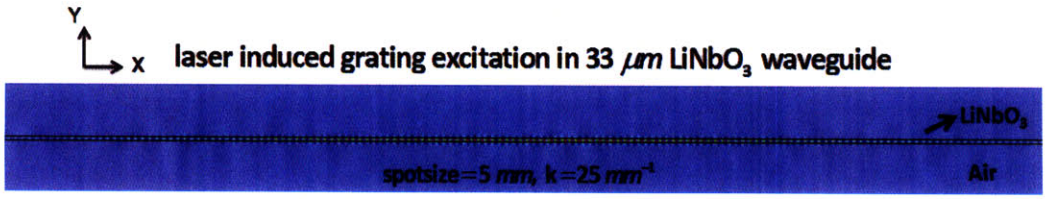


Figure 5-20: Laser induced grating excitation in a 33 $\mu m$ waveguide.

Tunable multi-cycle or narrowband phonon-polariton wave by grating periodicity is shown in Figure 5-21. The spot size was assumed as $5mm$, and there are as many as 100 cycles of polariton waves in the envelope, which will result in an extremely narrowed bandwidth. The tunability completely follows the dispersion properties of the fundamental mode in a 33 $\mu m$ $LiNbO_3$ waveguide.

With relatively large grating wave number and smaller spot size, the polariton wave frequency content can be influenced by both the grating periodicity and the envelope function, the latter of which is similar to the line excitation scheme discussed before. In Figure 5-22, the spot size is 0.5 $mm$ and the grating wave number is 25 $mm^{-1}$. Low and high frequency contents are excited initially, and both of them belong to the fundamental mode. The lower frequency part propagates faster, and the higher frequency part damps faster. These features are shown in Figure 5-23, where the time evolution are probed at different spots with L as the distance away from the center of the excitation region.

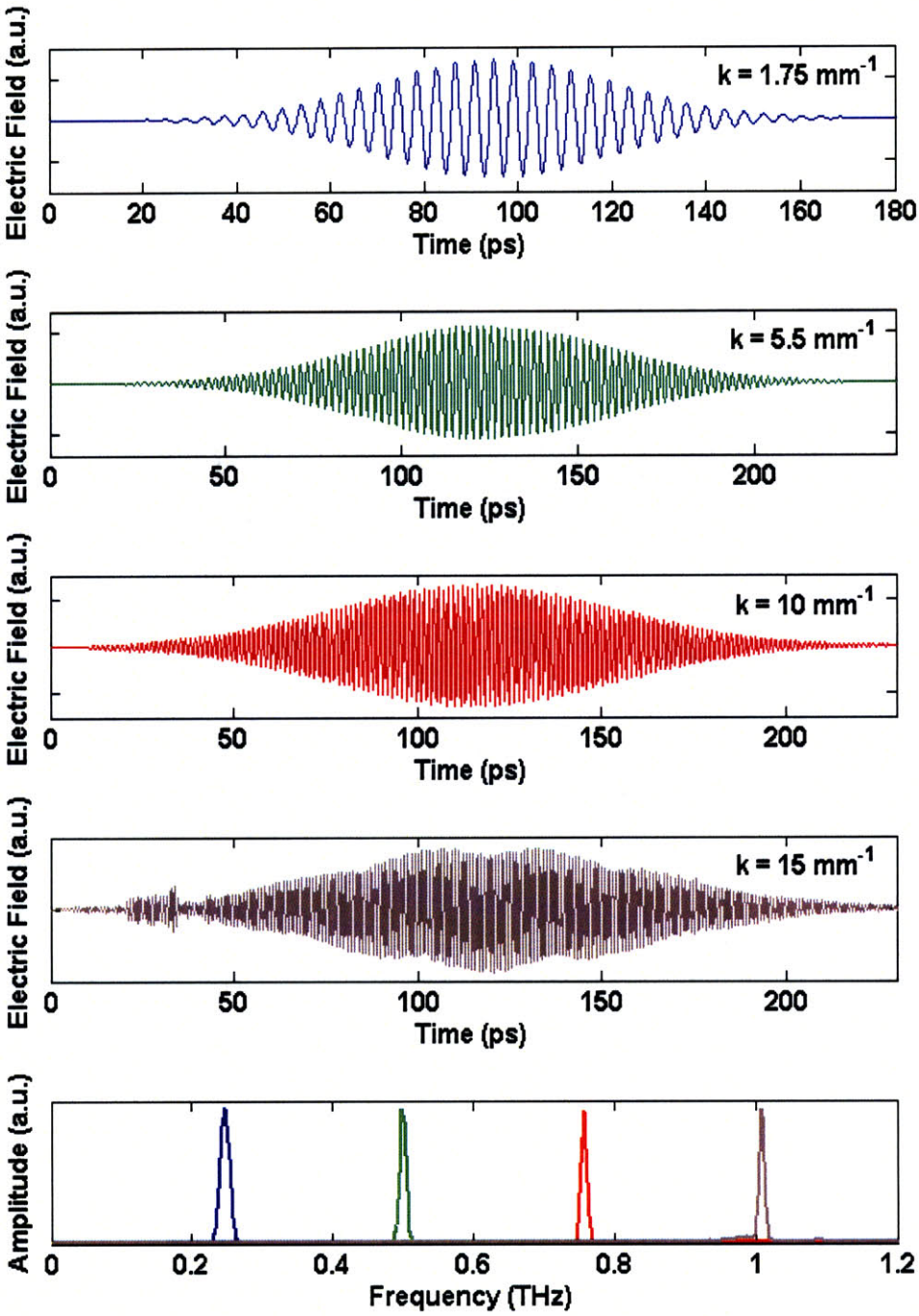


Figure 5-21: Narrowband phonon-polariton waves by tuning the grating periodicity. The dispersion properties follows the fundamental mode.

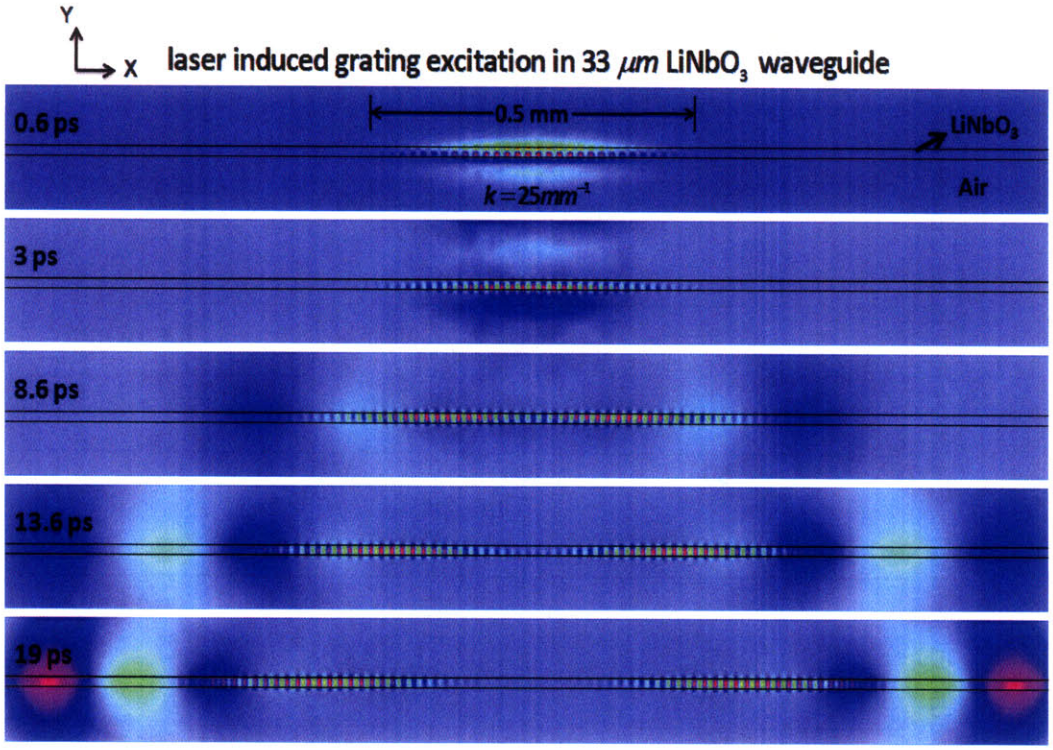


Figure 5-22: Narrowband phonon polariton wave, launched by laser induced grating excitation, is influenced by both the grating periodicity and the envelope function.

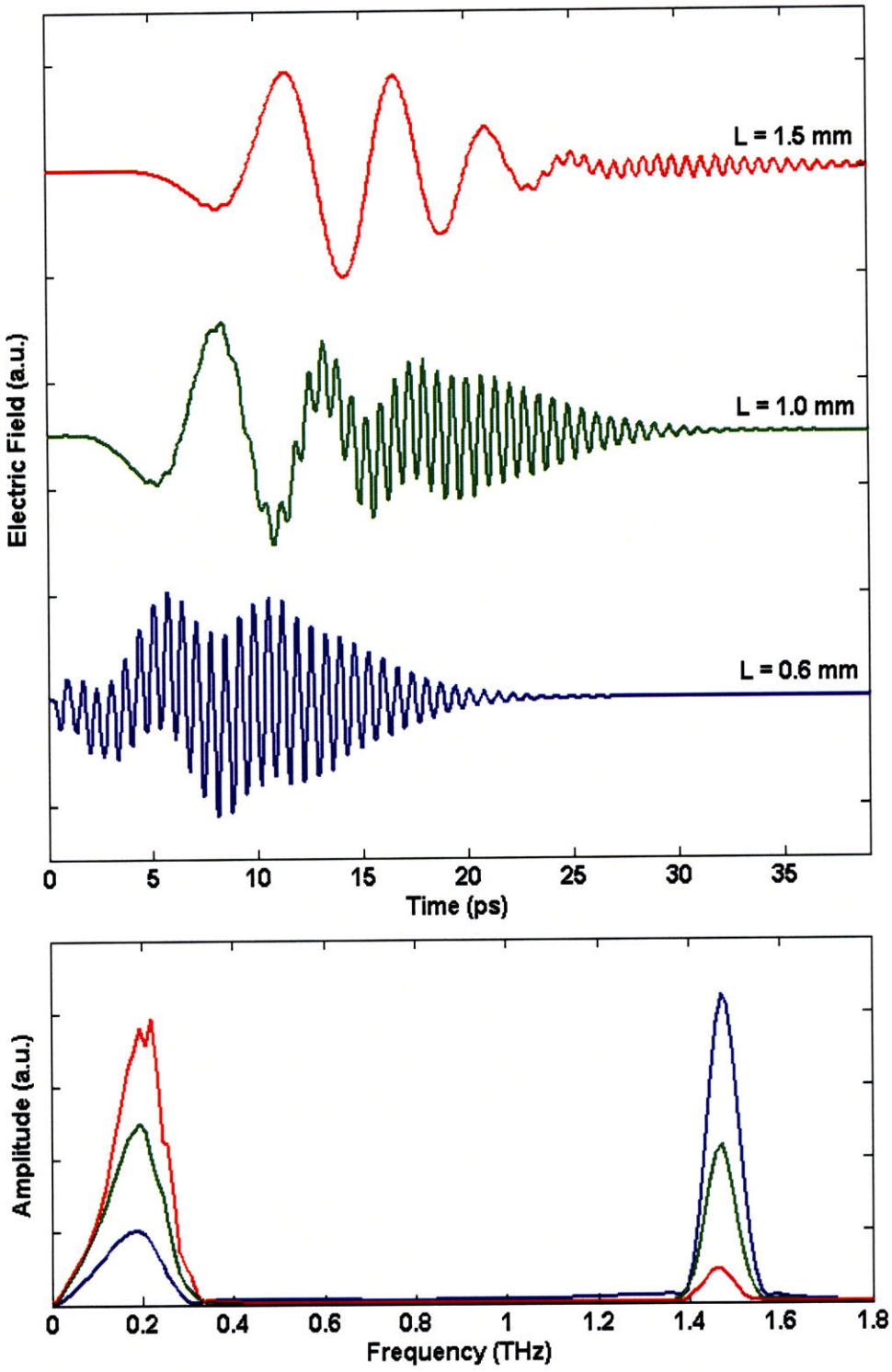


Figure 5-23: Narrowband phonon polariton wave, launched by laser induced grating excitation, is influenced by both the grating periodicity and the envelope function.

# Chapter 6

# Terahertz Field Enhancement

Nonlinear lattice dynamics and spectroscopy have long been particularly interesting and require large amplitude vibrational motion [115]. Recent progress in field enhancement includes phonon-polarition focusing in patterned material [45, 97, 30], spatial-temporal waveform control [100, 101, 33] and high power terahertz generation via a tiled-pulse-front [123, 41, 42, 40, 122, 121]. While many other methods will keep pushing this forward, in this chapter we present simulations of phonon-polariton focusing, the associated phase anomaly or gouy phase shift, and a simple multi-reflection method for gaining larger amplitude. Some of the following simulations can be further optimized because there are more tunable parameters in complicated geometries, and some are difficult to achieve in experiment, but as preliminary results and exploration, the unique phenomena are already clear and can be characterized.

## 6.1 Phonon-polariton Focusing

Phonon-polariton focusing is a straightforward way of enhancing the field amplitude. It is natural to think about focusing the polariton wave in three dimensional space, but in this chapter, we exclusively discuss the case in the Z-X plane as shown before, which can be compared with experiment, where the polariton imaging technique can be used to directly visualize the phonon-polarition generation and propagation.

Visualization of phonon-polariton focusing has been demonstrated experimentally

via an elliptical reflective mirror [97, 30], and full-circle and semicircular excitation [100, 101]. The associated gouy phase shift was observed as well [29, 30]. In this section, simulations of focusing through parabolic reflection, ellipse excitation and semicircular excitation are presented. In each method the gouy phase shift can be observed, and narrowband polariton wave can be easily achieved via either spatial, temporal or spatial-temporal pulse shaping.

### 6.1.1 Parabolic Reflection

As shown in Figure 6-2, the parabolic structure is designed to focus the phonon-polariton wave, which is near single cycle from line excitation scheme. Since the critical angle for total internal reflection of $LiNbO_3$-Air interface is $11.3^0$, the polariton wave propagating laterally to the left will be directed to the focus with little transmission loss. The crystal optical axis is along Z, and because of anisotropy the actual polaritonic focus will be shifted to the right of the geometric focus in this particular $LiNbO_3$ reflector. The distance between these two foci depends on the structure dimensions and parabolic parameter, but both foci are on a horizontal line. An improved off-axis reflector, or the central part of this parabolic curve, was designed to focus polariton waves as shown in Figure 6-1. Since the focus is far from the excitation region, clear field enhancement can be expected.

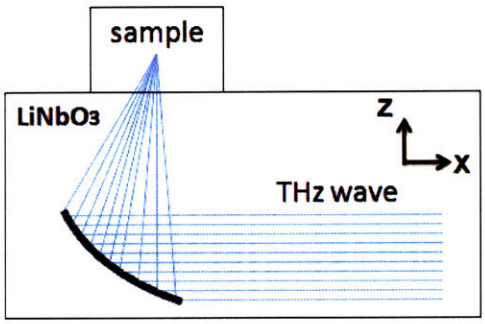


Figure 6-1: A simple off-axis parabolic reflector to focus phonon-polariton wave into the sample of interest.

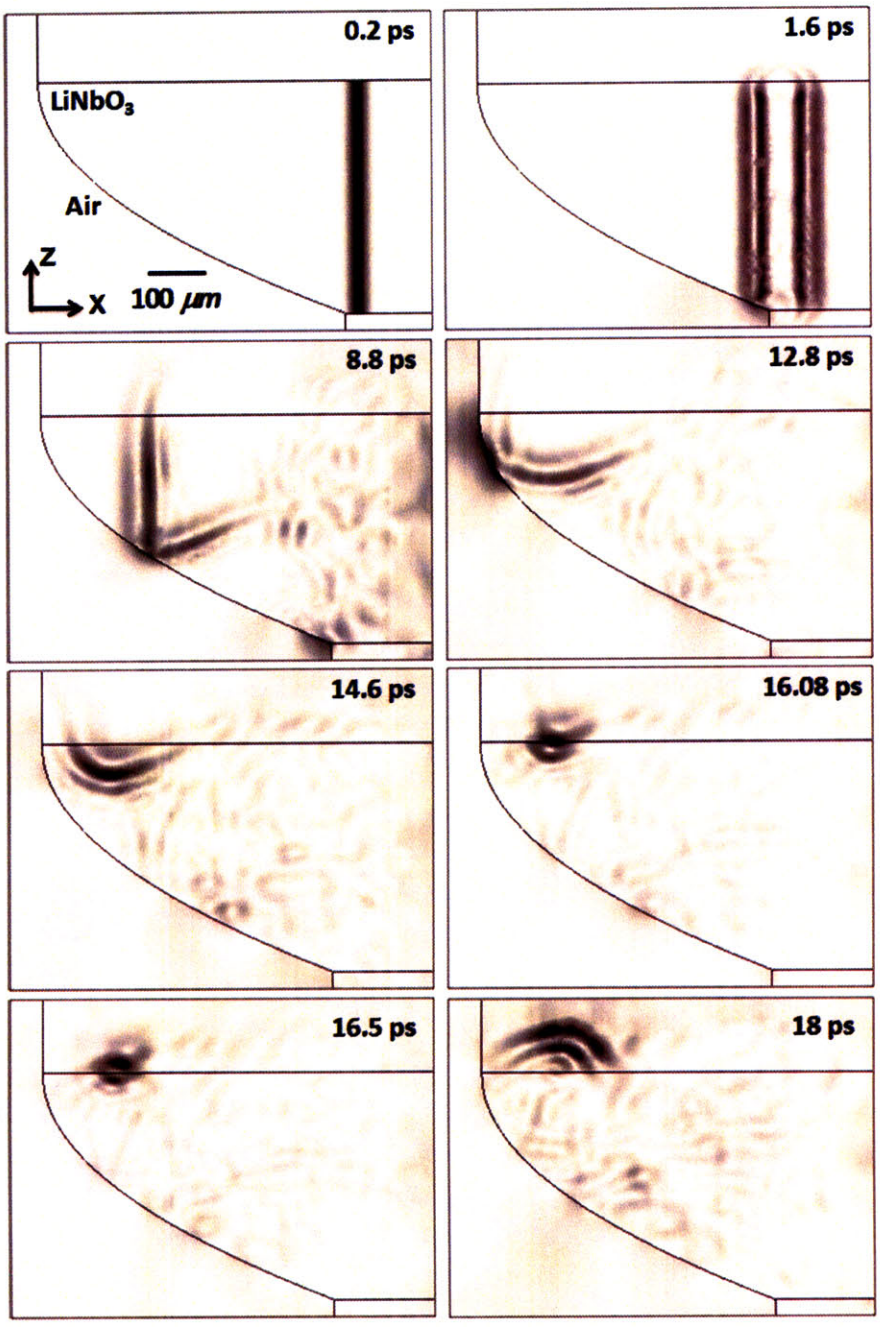


Figure 6-2: Simulations of phonon-polariton focusing through a parabolic reflector. Due to the anisotropy, the actual polaritonic focus is shifted to the right of the geometric focus.

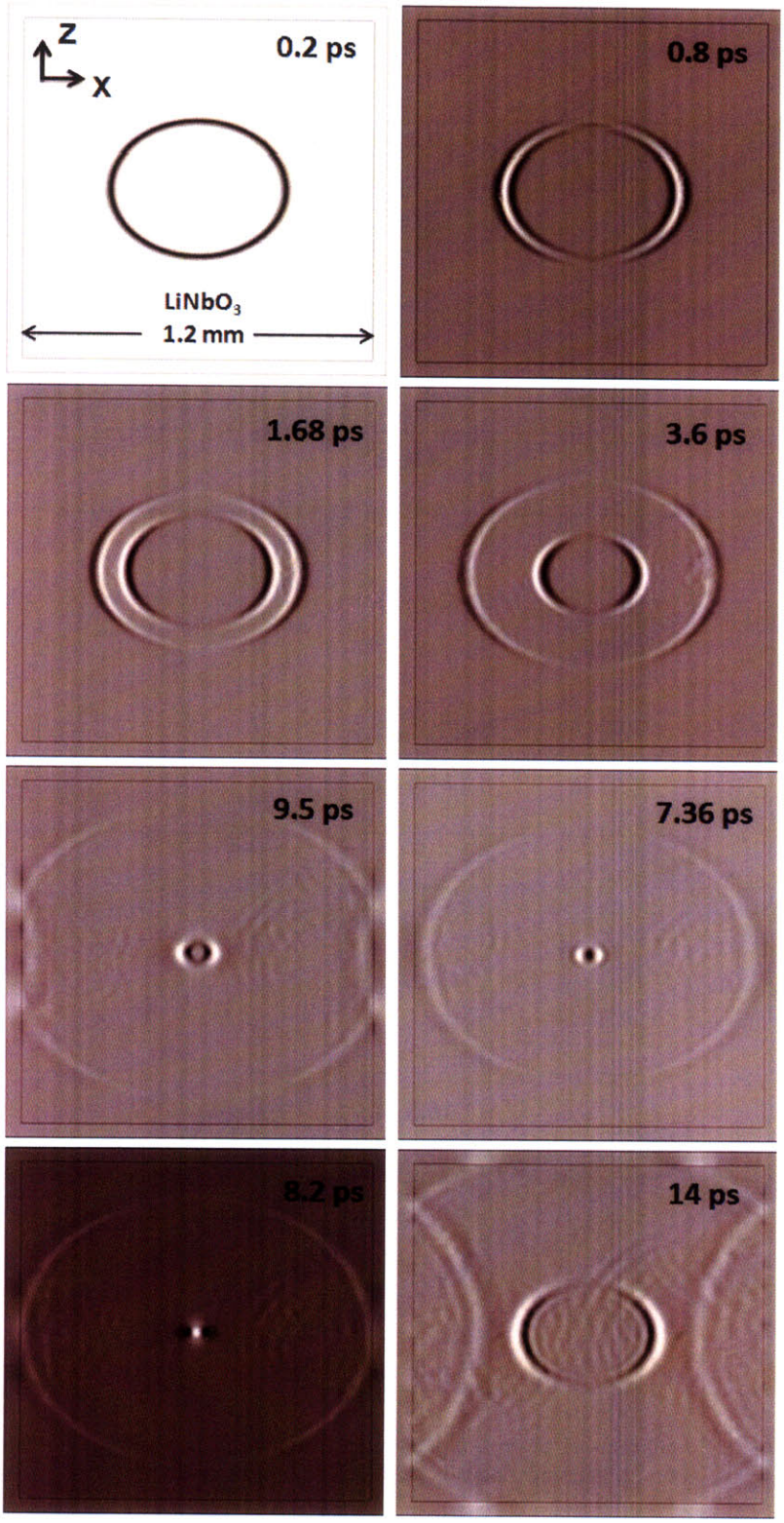


Figure 6-3: Full-ellipse excitation.

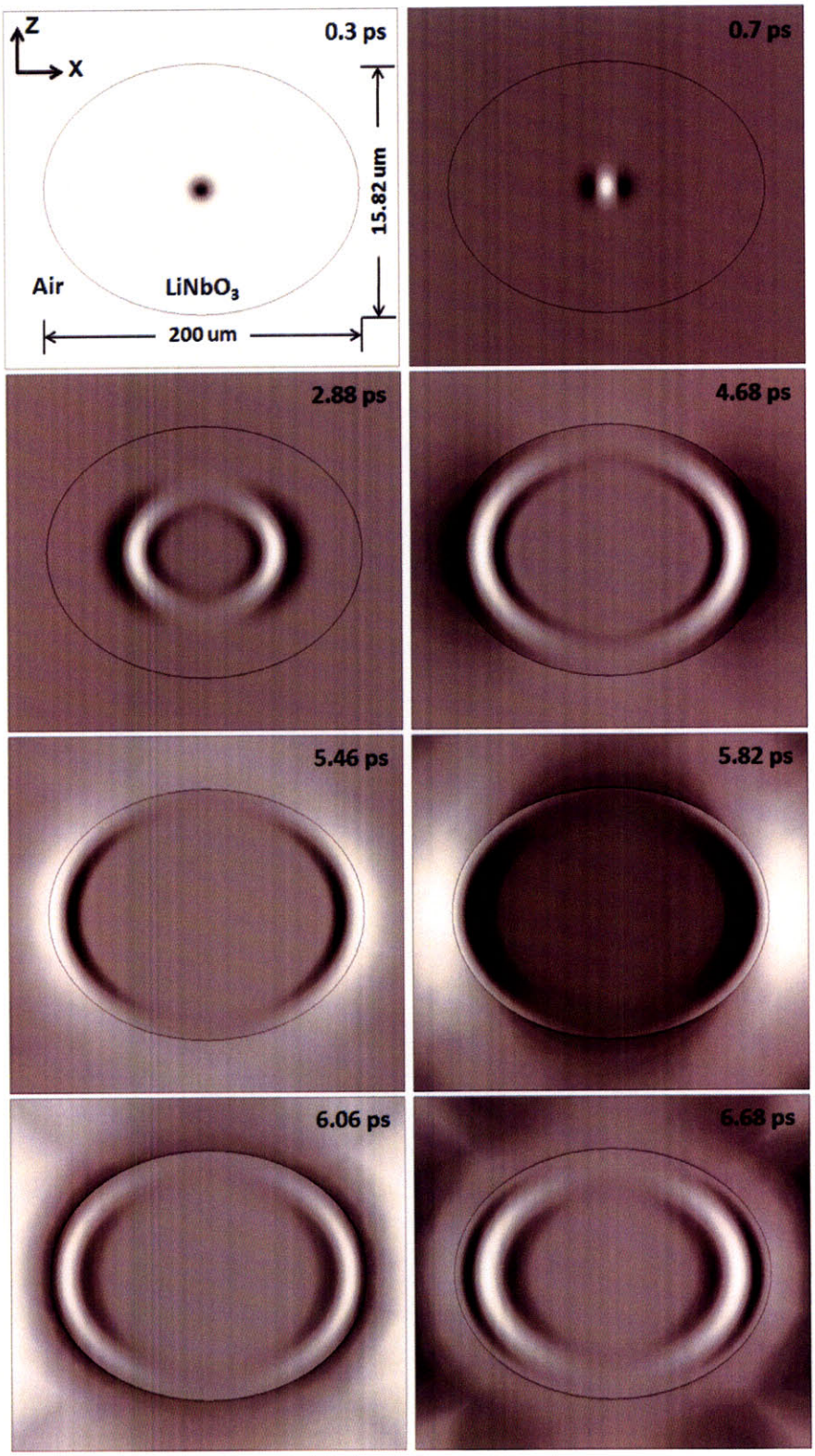


Figure 6-4: Resonator.

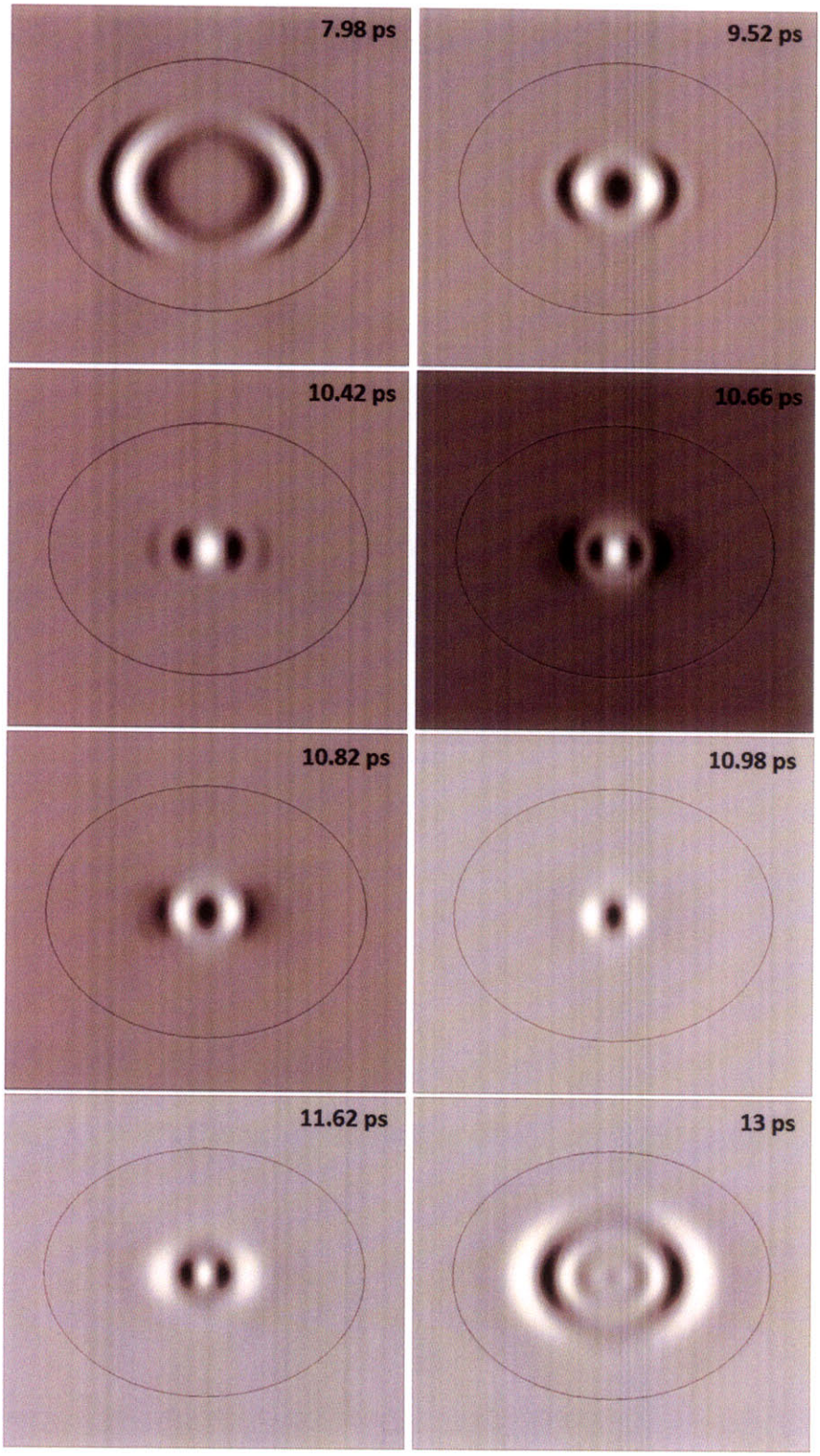


Figure 6-5: Resonator.

### 6.1.2 Ellipse Geometry

In chapter 4, it was shown that a phonon-polariton wave generated in $LiNbO_3$ through full-circle excitation can not focus well due to anisotropy. Here, an ellipse excitation, which can achieved through two cylindrical lenses for example, can be used to focus a polariton wave as shown in Figure 6-3, where the two main axis are 600 $\mu m$ and 474.6 $\mu m$. Also, a $LiNbO_3$ resonator with an ellipse structure is shown in Figure 6-4 and 6-5. Single-cycle polariton waves, launched with a tightly focused round spot beam, propagated to the edge of $LiNbO_3$, reflected back, and focused again at the original position. Furthermore, polariton waves excited with either spatially or temporally shaped puleses can be in phase to scale up the enhancement.

### 6.1.3 Semielliptical Excitation

Circular excitation can be achieved with an axicon-lens combination in experiment, and for semicircular excitation, half of the ring is blocked. In [29] and [100], the semicircular polariton wave is focused with little spatial distortion due to anisotropy in $LiTaO_3$. In $LiNbO_3$, however, the actual focus will be significantly shifted. While it is more convenient to achieve semicircular excitation in experiment, here instead we present a semielliptical excitation as shown in Figure 6-6.

### 6.1.4 Multi-cycle Wave Focusing

Multi-cycle phonon-polariton waves can be realized with either spatial or temporal pulse shaping as shown in Figure 6-7 and 6-8 respectively. As indicated in Chapter 4, the bandwidth of multi-cycle waves will be narrowed, and the more cycles there are, the narrower the bandwidth will be. The central frequency can be tuned by changing the spatial or temporal delay. In the spatial shaping figures, there are 10 cycles and in the temporal shaping ones, there are 6 cycles between the place of the excitation and the focus. The frequency-dependent phenomena can be better observed with narrowband waves, and in the next section, we present the phase anomaly or gouy phase shift in both single-cycle and multi-cycle cases.

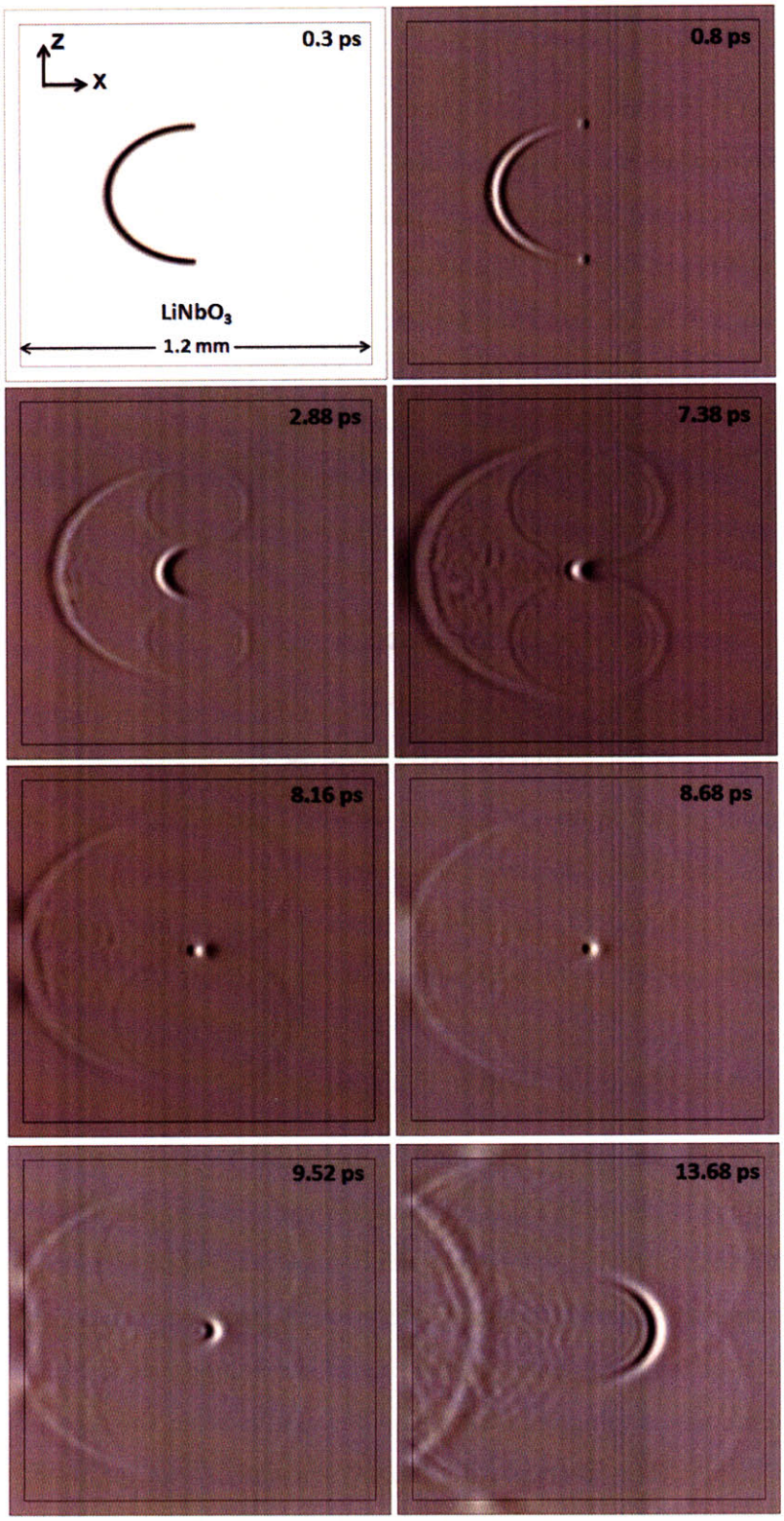


Figure 6-6: A single-cycle semielliptical phonon polariton wave propagates from left to right and focuses at the center with an increase in amplitude.

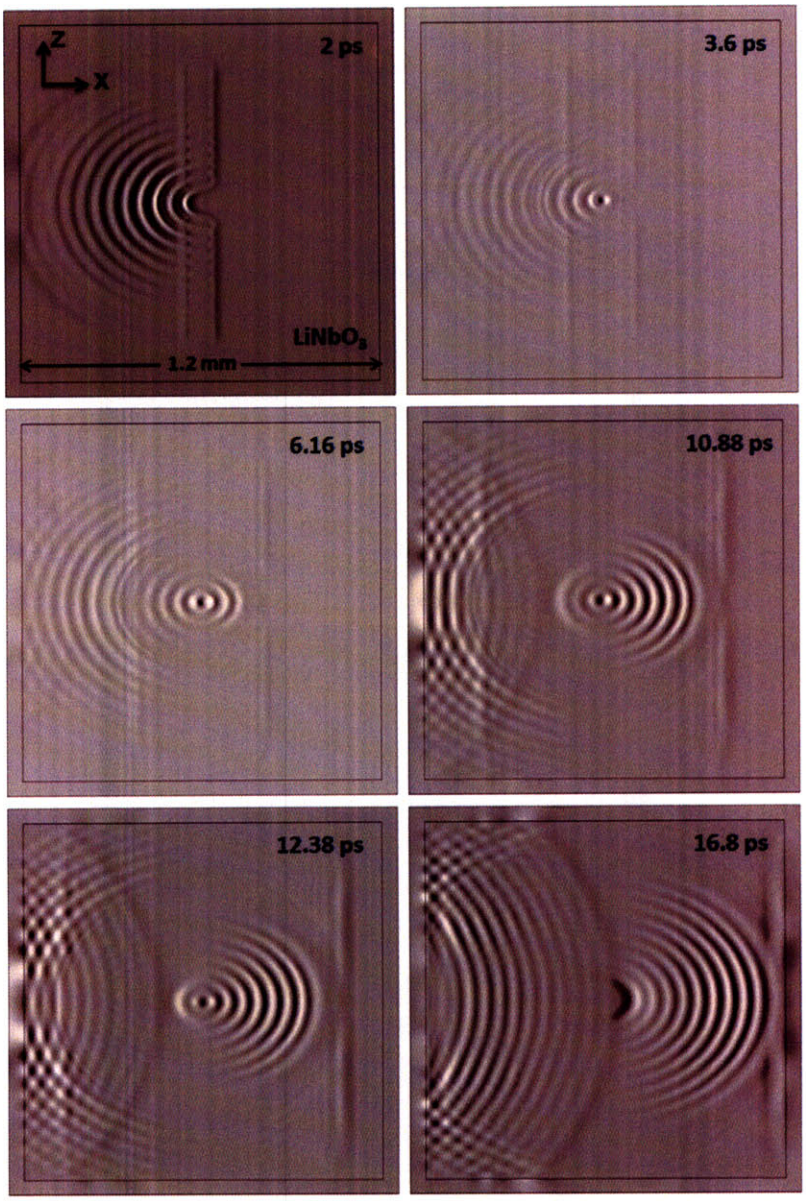


Figure 6-7: A multi-cycle semielliptical phonon polariton wave, excited by spatially shaped pulses, propagates from left to right and focuses at the center. The distance between two wave packets along the central horizontal line is 50 $\mu m$.

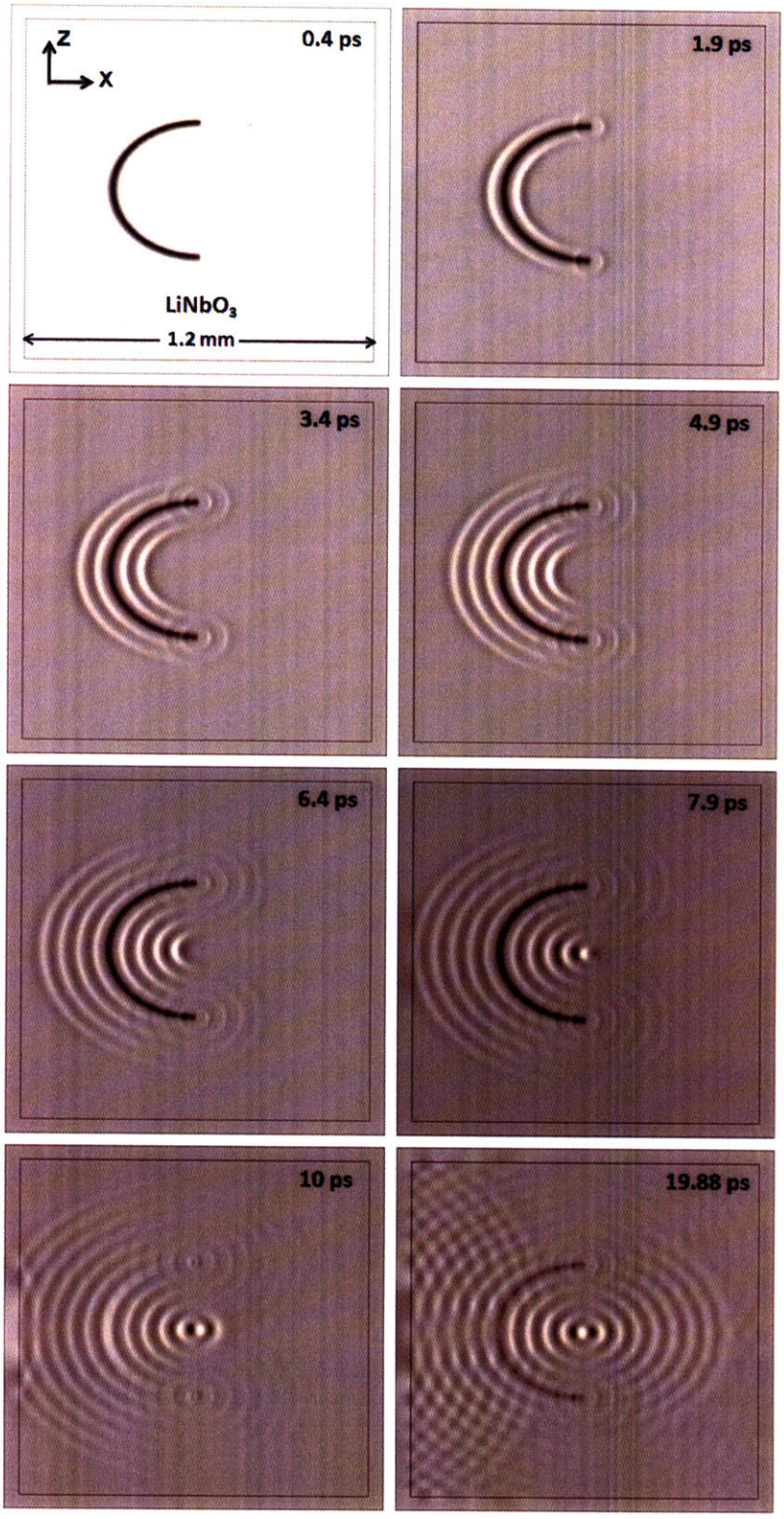


Figure 6-8: A multi-cycle semielliptical phonon polariton wave, excited by temporally shaped pulses, propagates from left to right and focuses at the center. The temporal delay between two wave packets is 1.5 ps.

## 6.2 Gouy Phase Shift

The gouy phase anomaly can be observed whenever a wave focuses to the diffraction limit, where the wavevector content relocates due to the spatial confinement and shifts back after the focal region. The gouy phase by focusing phonon polaritons has been demonstrated and visualized before [29, 100] in one dimension confinement along the optic axis, in which the phase shift is expected to be $\pi/2$. The following simulations show excellent agreement with experiments and give preliminary results of multi-cycle phonon-polariton wave focusing.

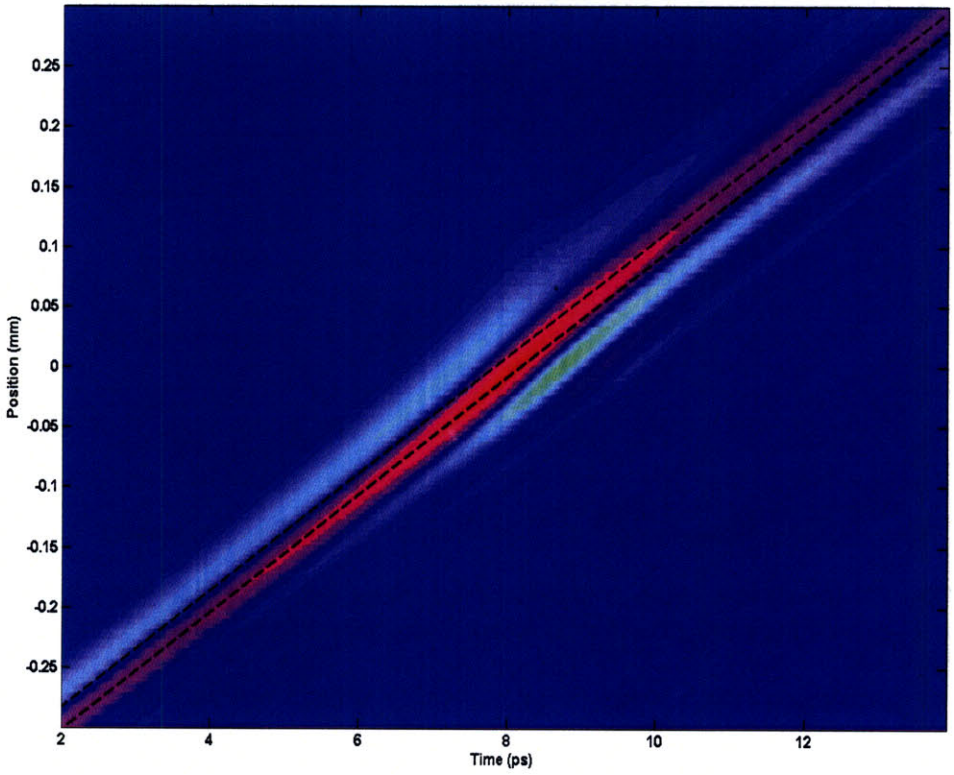


Figure 6-9: Space-time plot of the field distribution of the single-cycle phonon-polariton wave shown in Figure 6-6. The two dotted lines indicate the normal phase peak traces.

The space-time plot of single-cycle phonon-polariton focusing in Figure 6-6 is shown in Figure 6-9, which shows the electric field distribution of the polariton wave as a function of time and position along the propagation direction. It is clearly shown that when the wave packet propagates around 8.5 ps, the phase velocity increases

in the focal region and decrease back to the original value after the focus. The two dotted lines in the figure give the extrapolation of normal phase peak based on the traces before and after the focal region. Along the lower free space propagation line, the phase shifts from the peak position to somewhere between the peak and the valley after the focal region, which gives the phase shift value around $\pi/2$ qualitatively.

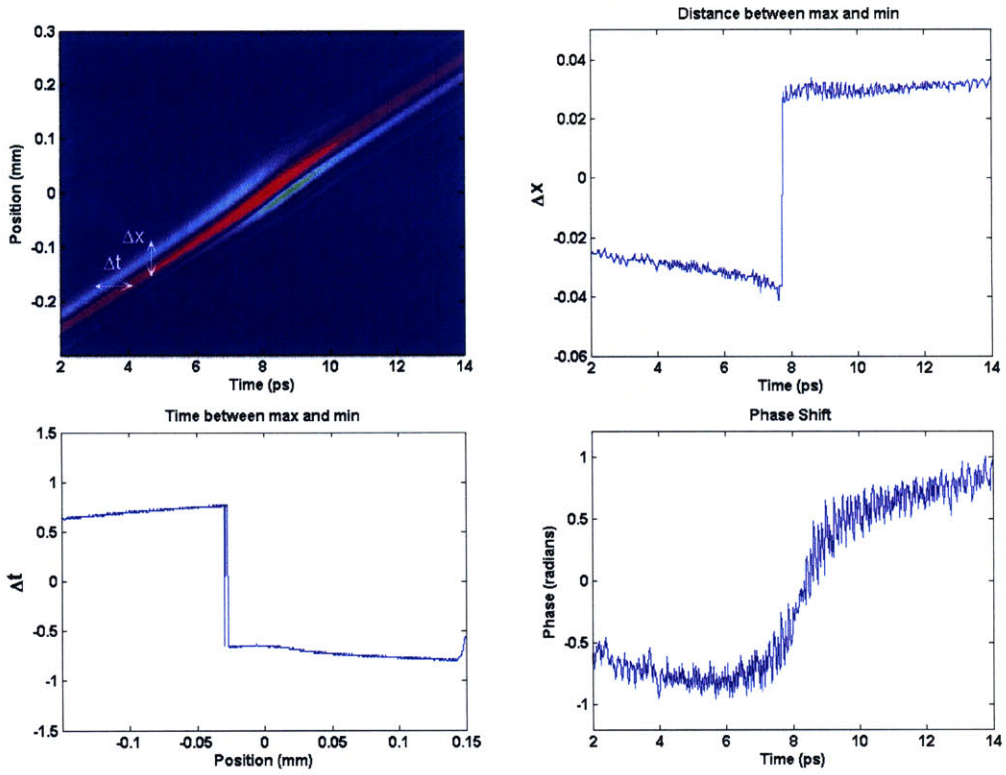


Figure 6-10: Quantitative determination of gouy phase shift of the single-cycle phonon-polariton wave shown in Figure 6-6. The $\Delta$x and $\Delta$t are the distance and time delay between the phase peak and valley.

Quantitatively as in Figure 6-10, the normal phase propagation information can be extracted by averaging the distance between the phase peak and valley at a certain time, and the time delay between the phase peak and valley at a certain point. Subtracting the free space propagation from the single-cycle phonon-polariton wave, the phase anomaly in the focal region is clearly revealed. The phase difference between any two points with the exactly same time delay before and after the focusing 8.2 ps gives the shift amount $\pi/2$.

For the multi-cycle polariton wave, we will discuss the temporal shaping in Figure 6-8 in detail. The time delay between two wave packets was set as 1.5 ps just to make the waveform in time domain as smooth as possible. The space-time plot accordingly is shown in Figure 6-11.

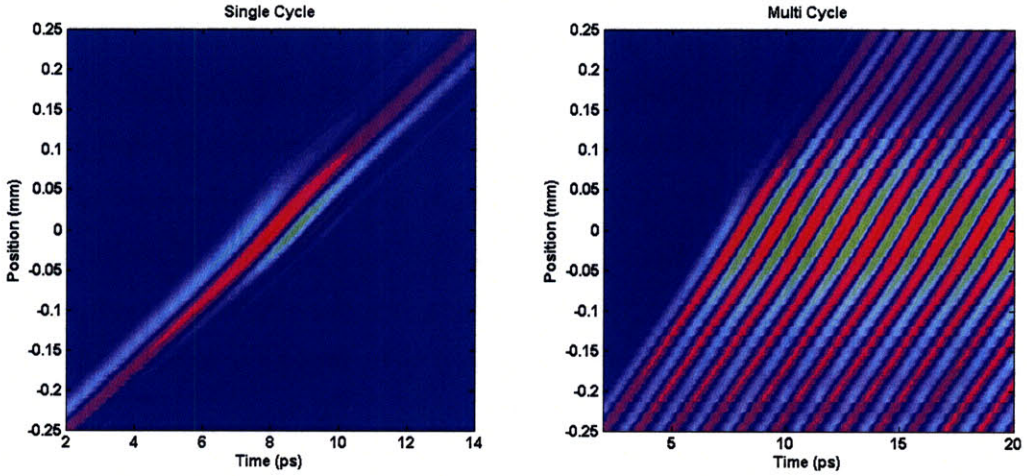


Figure 6-11: Space-time plots of the field distribution of single-cycle and the temporally shaped multi-cycle phonon-polarition wave packets along the propagation direction.

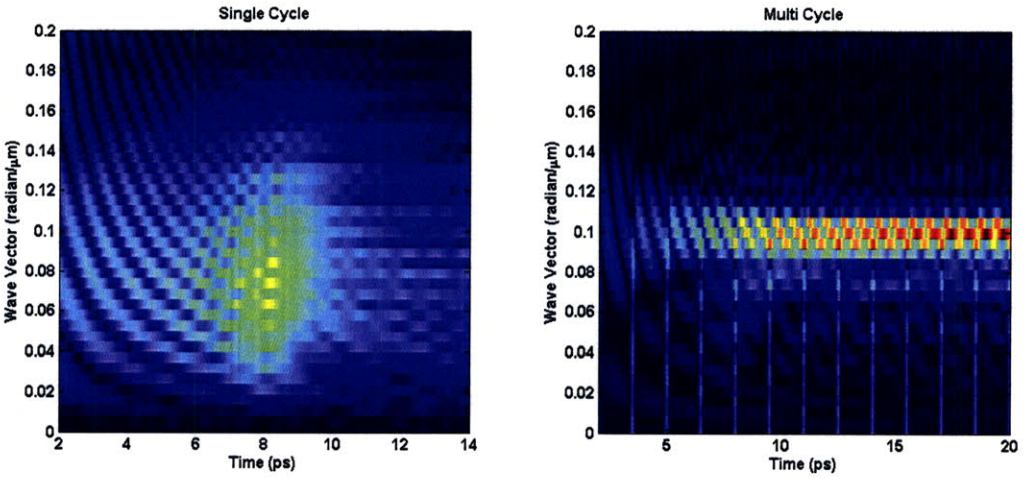


Figure 6-12: Distribution of wave vector components along the propagation direction as a function of time for the single-cycle and the temporally shaped multi-cycle phonon-polarition wave packets.

With the spatial confinement perpendicular to the propagation direction, the wavevector components along that will be shifted positively according to the uncertainty principle, so the wavevector contents along the propagation direction will

decrease in the focal region.

## 6.3 Multi-reflection

High power terahertz generation via tilted-pulse-front [41, 42, 40, 122, 121] has been demonstrated recently, and a multi-reflection scheme was proposed [123, 41] to further improve the velocity matching and re-use the optical pulses to achieve even higher terahertz output. As illustrated in Figure 6-13, the blue lines are the pump beam traces with a tilted-pulse-front, and the orange lines are the expected enhanced terahertz output. The pump beam enters the crystal at the complement of the Cherenkov angle so that the generated THz wave propagates laterally down the crystal; when the pump beam is further bounced back and forth with total internal reflection, the THz response will be greatly enhanced.

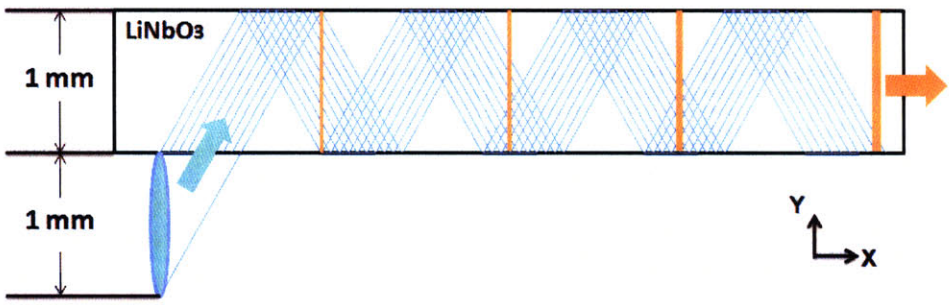


Figure 6-13: Illustration of multi-reflection scheme.

Preliminary simulation results of the THz response are shown in Figures 6-14 and 6-15, where the maximum and minimum electric field amplitudes at periodic moments right before each bounce are indicated. With a $LiNbO_3$ crystal of length 6 mm, the field amplification is 3.6 for maxima and 3.3 for minima, which means a 10 times enhancement in peak intensity. It is also obvious that the near single cycle phonon-polariton spreads over time in the vertical dimension, which means the THz intensity and power enhancement is even larger. Further optimization can be made by adjusting parameters like pulse duration and crystal thickness, etc.

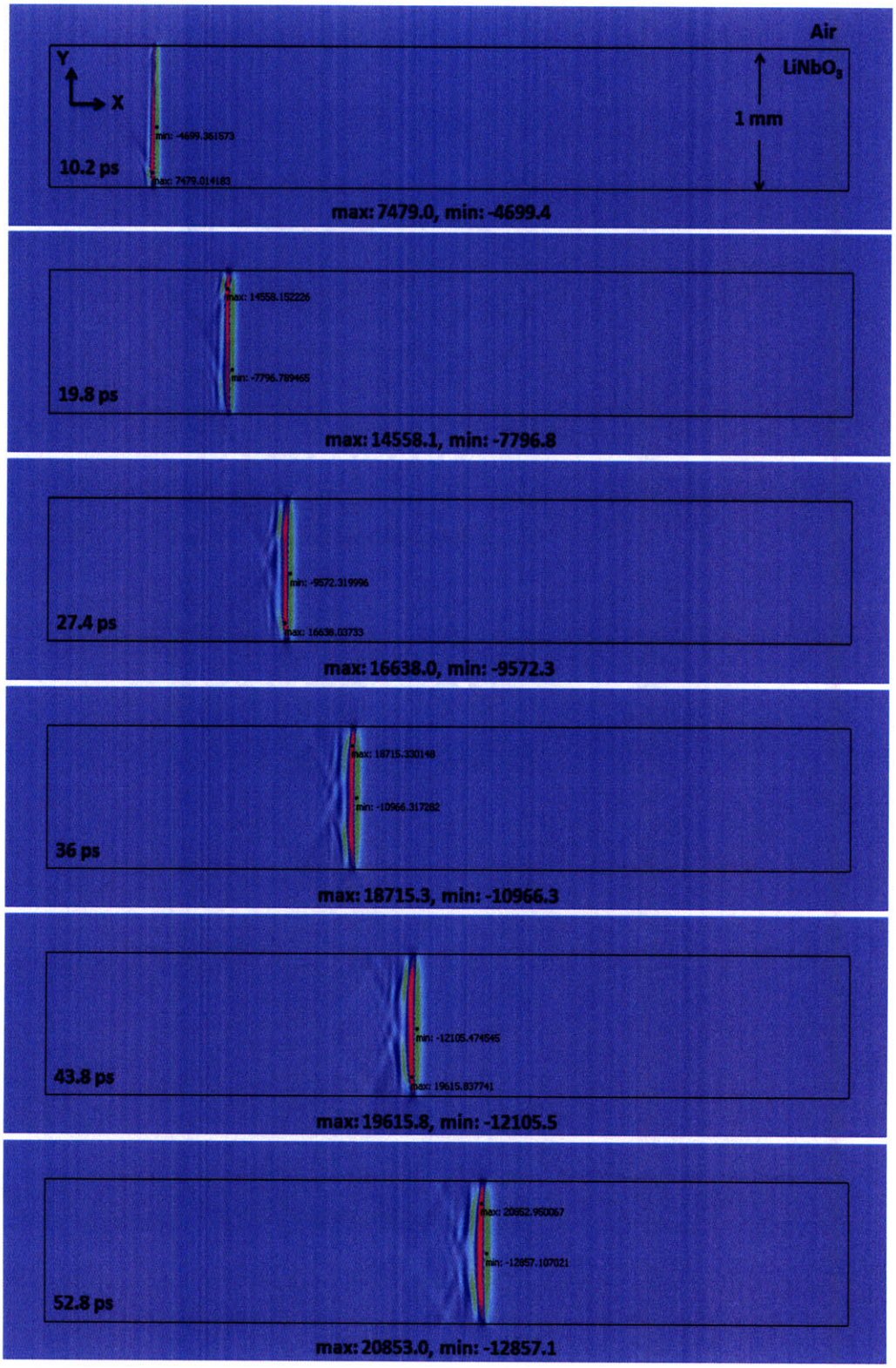


Figure 6-14: Simulation results of the multi-reflection scheme for enhancing terahertz field.

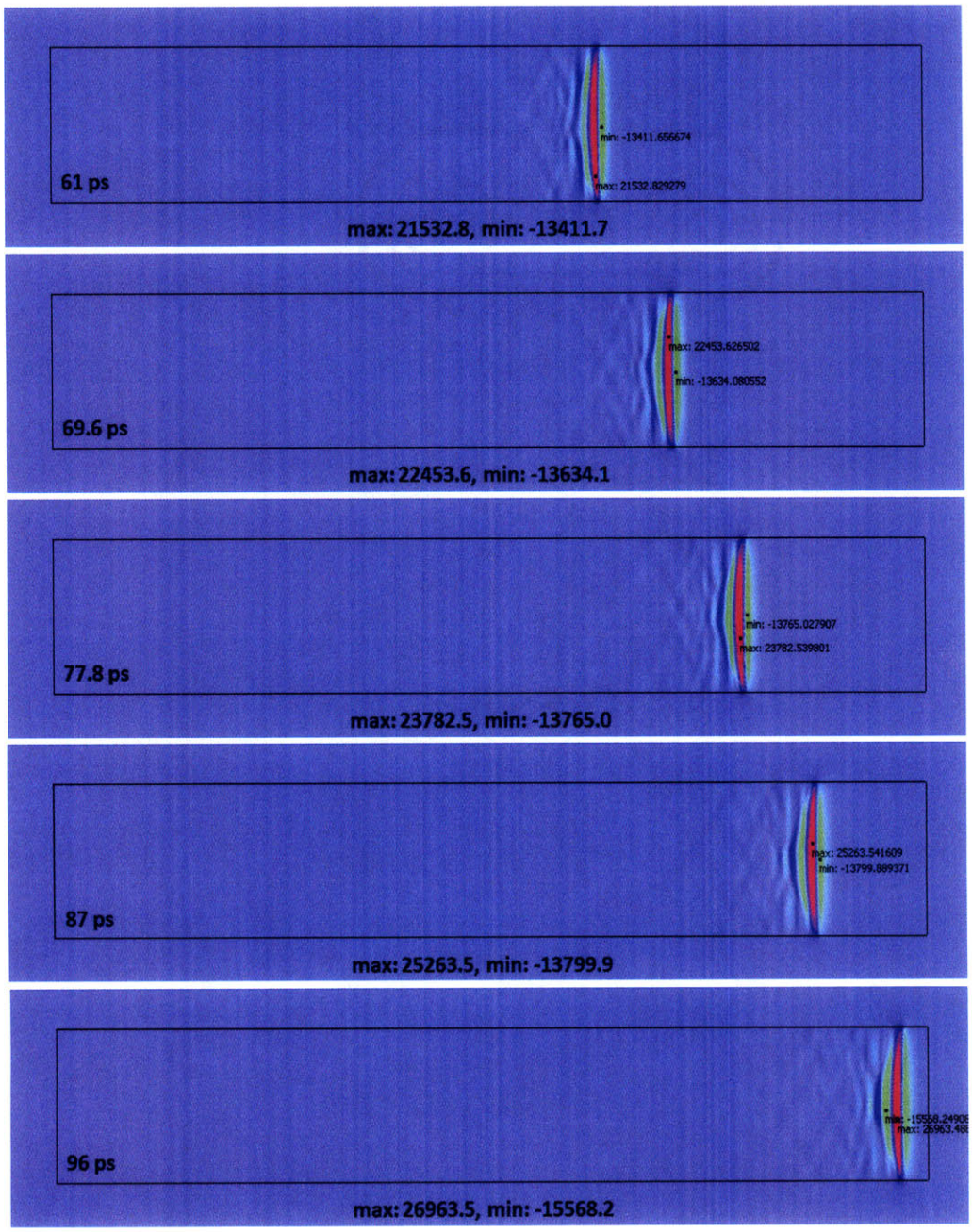


Figure 6-15: Simulation results of the multi-reflection scheme for enhancing terahertz field.

# Bibliography


[1] S. Adachi, R.M. Koehl, and K.A. Nelson. Real-space and real-time imaging of polariton wavepackets. *J. Lumin.*, 87-89:840–843, 2000.

[2] Abdul Al-Azzawi. *Photonics: Principles and Practices.* CRC Press, 2006.

[3] D. Allan and A.P. Cracknell. Polaritons in $LiTaO_3$. *J. Phys. C: Solid St. Phys.*, 10:123–136, 1977.

[4] Jr. A.S. Barker and R. Loudon. Dielectric properties and optical phonons in $LiNbO_3$. *Phys. Rev.*, 158:433–445, 1967.

[5] Jr. A.S. Barker and R. Loudon. Response functions in the theory of raman scattering by vibrational and polariton modes in dielectric crystals. *Rev. Mod. Phys.*, 44:18–47, 1972.

[6] D.H. Auston. Subpicosecond electro-optic shock waves. *Appl. Phys. Lett.*, 43:713, 1983.

[7] D.H. Auston, K.P. Cheung, J.A. Valdmanis, and D.A. Kleinman. Cherenkov radiation from femtosecond optical pulses in electro-optic media. *Phys. Rev. Lett.*, 53:1555 – 1558, 1984.

[8] D.H. Auston and M.C. Nuss. Electrooptic generation and detection of femtosecond electrical transients. *Quantum Electronics, IEEE Journal of*, 24(2):184–197, Feb 1988.

[9] J.D. Axe and D.F. O'Kane. Infrared dielectric dispersion of $LiNbO_3$. *Appl. Phys. Lett.*, 9:58, 1966.

[10] P. Berenger. Three-dimensional perfectly matched layer for the absorption of electromagnetic waves. *Journal of Computational Physics*, 127:363–379, 1996.

[11] B.J. Berne and R. Pecora. *Dynamic light scattering : with applications to chemistry, biology, and physics.* Wiley, New York, 1976.

[12] M. Born and K. Huang. *Dynamical Theory of Crystal Lattices.* Oxford University Press, London, 1954.

[13] Ciaran Joseph Brennan. *Femtosecond wavevector overtone spectroscopy of anharmonic lattice dynamics in ferroelectric crystals.* PhD thesis, Massachusetts Institute of Technology, 1997.

[14] L. Brillouin. Diffusion of light and x-rays by a transparent homogeneous body. the influence of thermal agitation. *Ann. phys. (Paris)*, 17:88–122, 1922.

[15] M.H. Brodsky, E. Burstein, M. Cardona, L.M. Falicov, M.V. Klein, R.M. Martin, A. Pinczuk, A.S. Pine, and Y.-R. Shen. *Light Scattering in Solids.* Springer-Verlag, 1975.

[16] A. Cavalleri, S. Wall, C. Simpson, E. Statz, D.W. Ward, K.A. Nelson, M. Rini, and R. W. Schoenlein. Tracking the motion of charges in a terahertz light field by femtosecond x-ray diffraction. *Nautre*, 442:664–666, 2006.

[17] K.P. Cheung and D.H. Auston. Excitation of coherent phonon polaritons with femtosecond optical pulses. *Phys. Rev. Lett.*, 55(20):2152–2155, 1985.

[18] R. Claus. Light scattering by optical phonons and polaritons in perfect crystals. *phys. stat. sol. (b)*, 50:11, 1972.

[19] R. Claus, G. Borstel, E. Wiesendanger, and L. Steffan. Assignments of optical phonon modes in $LiNb_3$. *Phys. Rev. B*, 6:4878, 1972.

[20] R. Claus, L. Merten, and J. Brandmüller. *Light Scattering by Phonon-Polaritons.* Springer Tracts in Modern Physics, 1975.

[21] T.F. Crimmins, N.S. Stoyanov, and K.A. Nelson. Heterodyned impulsive stimulated raman scattering of phonon-polaritons in $LiTaO_3$ and $LiNbO_3$. *J. Chem. Phys.*, 117:2882–2896, 2002.

[22] Timothy Francis Crimmins. *Ultrahigh Frequency Characterization of Complex Materials using Transient Grating Techniques.* PhD thesis, Massachusetts Institute of Technology, 2000.

[23] L. Dhar, J.A. Rogers, and K.A. Nelson. Time-resolved vibrational spectroscopy in the impulsive limit. *Chem. Rev.*, 94:157–193, 1994.

[24] P.A.M. Dirac. The quantum theory of dispersion. *Proc. R. Soc. Lond. A*, 114:710–728, 1927.

[25] T.P. Dougherty, G.P. Wiederrecht, and K.A. Nelson. Impulsive stimulated raman scattering experiments in the polariton regime. *J. Opt. Soc. Am. B.*, 9:2179–2189, 1992.

[26] D. Dragoman and M. Dragoman. *Optical Characterization of Solids.* Springer, 2001.

[27] U. Fano. Atomic theory of electromagnetic interactions in dense materials. *Phys. Rev.*, 103:1202–1218, 1956.

[28] M.R. Farrar, L.-T. Cheng, Y.-X. Yan, and K.A. Nelson. Impulsive stimulated brillouin scattering in $KD_2PO_4$near the structural phase transition. *Quantum Electronics, IEEE Journal of*, 22:1453 – 1456, 1986.

[29] T. Feurer, N.S. Stoyanov, D.W. Ward, and K.A. Nelson. Direct visualization of the gouy phase by focusing phonon-polaritons. *Phys. Rev. Lett.*, 88(25), 2002.

[30] T. Feurer, N.S. Stoyanov, D.W. Ward, J.C. Vaughan, E.R. Statz, and K.A. Nelson. Terahertz polaritonics. *Annu. Rev. Mater. Res.*, 37:317–350, 2007.

[31] T. Feurer, J.C. Vaughan, T. Hornung, and K.A. Nelson. Typesetting of terahertz waveforms. *Opt. Lett.*, 29:1802–1804, 2004.

[32] T. Feurer, J.C. Vaughan, R.M. Koehl, and K.A. Nelson. Multidimensional control of femtosecond pulses by use of a programmable liquid-crystal matrix. *Opt. Lett.*, 27:652–654, 2002.

[33] T. Feurer, J.C. Vaughan, and K.A. Nelson. Spatiotemporal coherent control of lattice vibrational waves. *Science*, 299:374–377, 2003.

[34] T. Feurer, J.C. Vaughan, N.S. Stoyanov, and Keith A. Nelson. Coherent control over collective polariton excitations: the dawn of polaritonics. In R.D. Miller, M.M. Murnane, N.F. Scherer, and A.M. Weiner, editors, *Ultrafast Phenomena XIII*, pages 541–545, Berlin, 2002. Springer-Verlag.

[35] R.L. Fork, B.I. Greene, and C.V. Shank. Generation of optical pulses shorter than 0.1 ps by colliding pulse mode locking. *Appl. Phys. Lett.*, 38:671–672, 1981.

[36] B. Fornari and M. Pagannone. Experimental observation of the upper polartion branch in isotropic crystals. *Phys. Rev. B*, 17(8):3047–3050, 1977.

[37] A.M. Glass. Optical materials. *Science*, 235(4792):1003–1009, 1987.

[38] G. Grosso and G.P. Parravicini. *Solid State Physics.* Academic Press, 2000.

[39] W. Hayes and R. Loudon. *Scattering of light by crystals.* Wiley, New York, 1978.

[40] J. Hebling, K.-L. Yeh, M.C. Hoffmann, B. Bartal, and K.A. Nelson. Generation of high-power terahertz pulses by tilted-pulse-front excitation and their application possibilities. *J. Opt. Soc. Amer. B*, 25(7):B6–B19, 2008.

[41] J. Hebling, K.-L. Yeh, M.C. Hoffmann, and K.A. Nelson. Terahertz polaritonics: High power THz signal generation in ferroelectric crystals. *Integrated Ferroelectrics*, 92:87–94, 2007.

[42] J. Hebling, K.-L. Yeh, M.C. Hoffmann, and K.A. Nelson. High power THz generation, THz nonlinear optics, and THz nonlinear spectroscopy. *IEEE J. Selected Topics in Quantum Electronics*, 14:345–353, 2008.

[43] C.H. Henry and J.J. Hopfield. Raman scattering by polaritons. *Phys. Rev. Lett.*, 15:964–966, 1965.

[44] J.J. Hopfield. Theory of the contribution of excitons to the complex dielectric constant of crystals. *Phys. Rev.*, 112:1555 – 1567, 1958.

[45] T. Hornung, K.-L. Yeh, and K.A. Nelson. Terahertz nonlinear response in lithium niobate. In P. Corkum, D. Jonas, D. Miller, and A.M. Weiner, editors, *Ultrafast Phenomena XV*, pages 772–774, Berlin, 2007. Springer-Verlag.

[46] K. Huang. Lattice vibrations and optical waves in ionic crystals. *Nature*, 167:779–780, 1951.

[47] K. Huang. On the interaction between the radiation field and ionic crystals. *Proceedings of the Royal Society of London. Series A, Mathematical and Physical Sciences*, 208(1094):352–365, 1951.

[48] K.C. Huang, P. Bienstman, J.D. Joannopoulos, K.A. Nelson, and S. Fan. Phonon-polariton excitations in photonic crystals. *Phys. Rev. B.*, 68:075209, 2003.

[49] I.P. Kaminow and W.D. Johnston, Jr. Quantitative determination of sources of the electro-optic effect in $LiNbO_3$ and $LiTaO_3$. *Phys. Rev.*, 160(3):519–522, 1967.

[50] J.M. Jin. *The Finite Element Method in Electromagnetics.* Wiley, New York, 2002.

[51] D.A. Kleinman and D.H. Auston. Theory of electrooptic shock radiation in nonlinear optical media. *Quantum Electronics, IEEE Journal of*, 20(8):964–970, Aug 1984.

[52] Richard Michael Koehl. *Spatial and Temporal Ultrafast Imaging and Control of Terahertz Wavepackets.* PhD thesis, Massachusetts Institute of Technology, 1995.

[53] R.M. Koehl, S. Adachi, and K.A. Nelson. Direct visualization of collective wavepacket dynamics. *J. Phys. Chem. A*, 103:10260–10267, 1999.

[54] R.M. Koehl, S. Adachi, and K.A. Nelson. Real-space polariton wave packet imaging. *J. Chem. Phys.*, 110:1317–1320, 1999.

[55] R.M. Koehl, T.F. Crimmins, and K.A. Nelson. Lattice vibrations that move at the speed of light: how to excite them, how to monitor them, and how to image them before they get away. In M.D. Fayer, editor, *Ultrafast Infrared and Raman Spectroscopy*, pages 513–539. Marcel Dekker, New York, 2001.

[56] R.M. Koehl and K.A. Nelson. Coherent optical control over collective vibrations traveling at light-like speeds. *J. Chem. Phys.*, 114:1443–1446, 2001.

[57] R.M. Koehl and K.A. Nelson. Terahertz polaritonics: Automated spatiotemporal control over propagating lattice waves. *Chem. Phys.*, 267:151–159, 2001.

[58] H.A. Kramers and W. Heisenberg. The scattering of radiation by atoms. *Zeitschrift fuer Physik*, 31:681–708, 1925.

[59] P. Kukura, D.W. McCamant, and R.A. Mathies. Femtosecond stimulated raman spectroscopy. *Annu. Rev. Phys. Chem.*, 58:461–488, 2007.

[60] T. Kurosawa. Polarization waves in solids. *J. Phys. Soc. Jpn.*, 16:1298–1308, 1961.

[61] L. Merten. Polariton dispersion in biaxial and uniaxial crystals. *phys. stat. sol.*, 30:449–454, 1968.

[62] G. Landsberg and L. Mandelstam. Eine neue erscheinung bei der lichtzerstreuung in krystallen OR a novel effect of light scattering in crystals. *Naturwissenschaften*, 16:557–558, 1928.

[63] M. Lawrence. Lithium niobate integrated optics. *Rep. Prog. Phys.*, 56:363–429, 1993.

[64] Y.-S. Lee. *Principles of terahertz science and technology.* Springer, 2009.

[65] M.E. Lines and A.M. Glass. *Principles and applications of ferroelectrics and related materials.* International series of monographs on physics. Clarendon Press, 1977.

[66] S.A. Maier. *Plasmonics: Fundamentals and Applications.* Springer, 2007.

[67] A.A. Maznev, T.F. Crimmins, and K.A. Nelson. How to make femtosecond pulses overlap. *Opt. Lett.*, 23:1378–1380, 1998.

[68] A.A. Maznev, J.A. Rogers, and K.A. Nelson. Optical heterodyne detection of laser-induced gratings. *Opt. Lett.*, 23:1319–1321, 1998.

[69] J.G. Michopoulos, C. Farhat, and J. Fish. Modeling and simulation of multiphysics systems. *J. Comput. Inf. Sci. Eng.*, 5:198, 2005.

[70] D.L. Mills and E. Burstein. Polaritons: the electromagnetic modes of media. *Rep. Prog. Phys.*, 37:817–926, 1974.

[71] G. Mourou, C.V. Stancampiano, and D. Blumenthal. Picosecond microwave pulse generation. *Appl. Phys. Lett.*, 38:470, 1981.

[72] S. Nakajima, Y. Toyozawa, and R. Abe. *The Physics of Elementary Excitations.* Springer series in solid-state sciences. Springer-Verlag, 1980.

[73] Benjamin John Paxton. *Development of Phonon-Polariton THz Spectroscopy, and The Investigation of Relaxor Ferroelectrics.* PhD thesis, Massachusetts Institute of Technology, 2006.

[74] P. Peier, S. Pilz, F. Müller, K.A. Nelson, and T. Feurer. Analysis of phase contrast imaging of terahertz phonon-polaritons. *J. Opt. Soc. Am. B*, 25(7):B70–B75, 2008.

[75] D. Pines. *Elementary Excitations in Solids.* W. A. Benjamin, New York, 1964.

[76] J.M. Pitarke, V.M. Silkin, E.V. Chulkov, and P.M. Echenique. Theory of surface plasmons and surface-plasmon polaritons. *Rep. Prog. Phys.*, 70:1–87, 2007.

[77] G. Placzek. Rayleigh streeung und raman effekt. In E. Marx, editor, *Handbuch Der Radiologie*, volume VI, page 205.

[78] M. Posledovich, F. X. Winter, G. Borstel, and R. Claus. Properties of extraordinary polaritons in $LiNbO_3$. *phys. stat. sol. (b)*, 55:711, 1973.

[79] K. Rabe, Ch.H. Ahn, and J.-M. Triscone. *Physics of Ferroelectrics: a modern perspective.* Springer, 2007.

[80] C.V. Raman. The diamond. *Proc. Ind. Acad. Sci. Sec. A*, 44:99, 1956.

[81] C.V. Raman and K.S. Krishnan. A new type of secondary radiation. *Nature*, 121:501–502, 1928.

[82] Sir C.V. Raman. A new radiation. *Indian Journal of Physics*, 2:387–398, 1928.

[83] V. Romero-Rochín, R.M. Koehl, C.J. Brennan, and K.A. Nelson. Anharmonic phonon-polariton excitation through impulsive stimulated raman scattering and detection through wavevector overtone spectroscopy: Theory and comparison to experiments on lithium tantalate. *J. Chem. Phys.*, 111:3559–3571, 1999.

[84] R. Ruppin and R. Englman. Optical phonons of small crystals. *Rep. Prog. Phys.*, 33:149–196, 1970.

[85] K. Sakai. *Terahertz Optoelectronics.* Springer, 2005.

[86] R.F. Schaufele and M.J. Weber. Raman scattering by lithium niobate. *Phys. Rev.*, 152:705–708, 1966.

[87] C. A. Schmuttenmaer. Exploring dynamics in the far-infrared with terahertz spectroscopy. *Chem. Rev.*, 104:1759–1779, 2004.

[88] C.V. Shank. Investigation of ultrafast phenomena in the femtosecond time domain. *Science*, 233:1276–1280, 1986.

[89] C.V. Shank and E.P. Ippen. Subpicosecond kilowatt pulses from a mode-locked cw dye laser. *Appl. Phys. Lett.*, 24:373–375, 1974.

[90] Y.R. Shen. Theory of stimulated raman effect. II. *Phys. Rev.*, 138:A1741, 1965.

[91] Y.R. Shen. Far-infrared generation by optical mixing. *Progress in Quantum Electronics*, 4:207, 1976.

[92] Y.R. Shen and N. Bloembergen. Theory of stimulated brillouin and raman scattering. *Phys. Rev.*, 137:A1787, 1965.

[93] Y.R. Shen and N. Bloembergen. Interaction between light waves and spin waves. *Phys. Rev.*, 143:372–384, 1966.

[94] S.K. Kurtz and J.A. Giordmaine. Stimulated raman scattering by polaritons. *Phys. Rev. Lett.*, 22:192–195, 1969.

[95] A. Smekal. Zur quantentheorie der dispersion OR the quantum theory of dispersion. *Naturwissenschaften*, 11:873–875, 1923.

[96] E.R. Statz, D.W. Ward, and K.A. Nelson. Phonon-polariton excitation in ferroelectric slab waveguides and photonic crystals. In P. Corkum, D. Jonas, D. Miller, and A.M. Weiner, editors, *Ultrafast Phenomena XV*, pages 784–786, Berlin, 2007. Springer-Verlag.

[97] Nikolay Staykov Stoyanov. *Phonon-Polaritons in Bulk and Patterned Materials.* PhD thesis, Massachusetts Institute of Technology, 2003.

[98] N.S. Stoyanov, T. Feurer, D.W. Ward, and K.A. Nelson. Integrated diffractive terahertz elements. *Appl. Phys. Lett.*, 82:674–676, 2003.

[99] N.S. Stoyanov, T. Feurer, D.W. Ward, E.R. Statz, and K.A. Nelson. Direct visualization of a polariton resonator in the THz regime. *Opt. Express*, 12:2387–2396, 2004.

[100] N.S. Stoyanov, D.W. Ward, T. Feurer, and K.A. Nelson. Direct visualization of phonon-polariton focusing and amplitude enhancement. *J. Chem. Phys.*, 117:2897–2901, 2002.

[101] N.S. Stoyanov, D.W. Ward, T. Feurer, and K.A. Nelson. Terahertz polariton propagation in patterned materials. *Nature Materials*, 1:95–98, 2002.

[102] M. Tonouchi. Cutting-edge terahertz technology. *Nature Photonics*, 1:97–105, 2007.

[103] Joshua Charles Vaughan. *Two-dimensional Ultrafast Pulse Shaping and its Application to Coherent Control and Spectroscopy.* PhD thesis, Massachusetts Institute of Technology, 2005.

[104] T. Volk and M. Wöhlecke. *Lithium niobate: defects, photorefraction and ferroelectric switching.* Springer, 2008.

[105] J.K. Wahlstrand and R. Merlin. Cherenkov radiation emitted by ultrafast laser pulses and the generation of coherent polaritons. *Phys. Rev. B*, 68:054301, 2003.

[106] David Wayne Ward. *Polaritons: An Intermediate Regime Between Electronics and Photonics.* PhD thesis, Massachusetts Institute of Technology, 2005.

[107] D.W. Ward, J.D. Beers, T. Feurer, E.R. Statz, N. Stoyanov, and K.A. Nelson. Coherent control of phonon-polaritons in a terahertz resonator fabricated with femtosecond laser machining. *Opt. Lett.*, 29:2671–2673, 2004.

[108] D.W. Ward and K.A. Nelson. Finite-difference time-domain (fdtd) simulations of electromagnetic wave propagation using a spreadsheet. *Comput. Appl. Eng. Educ.*, 13:213–221, 2005.

[109] D.W. Ward, E.R. Statz, J.D. Beers, T. Feurer, J.D. Joannopoulos, R.M. Roth, R.M. Osgood, K.J. Webb, and K.A. Nelson. Polaritonics in complex structures: confinement, bandgap materials, and coherent control. In T. Kobayashi, T. Okada, T. Kobayashi, K.A. Nelson, and S.De Silvestri, editors, *Ultrafast Phenomena XIV*, pages 298–300, Berlin, 2005. Springer-Verlag.

[110] D.W. Ward, E.R. Statz, and K.A. Nelson. Fabrication of polaritonic structures in $LiNbO_3$ and $LiTaO_3$ using femtosecond laser machining. *Applied Physics A - Materials Science & Processing*, 86(1):49–54, 2007.

[111] D.W. Ward, E.R. Statz, K.A. Nelson, R.M. Roth, and R.M. Osgood. Terahertz wave generation and propagation in thin film lithium niobate produced by crystal ion slicing. *Appl. Phys. Lett.*, 86(2):022908, 2005.

[112] D.W. Ward, E.R. Statz, N.S. Stoyanov, and K.A. Nelson. Simulation of phonon-polariton propagation in ferroelectric $LiNbO_3$. In R. Wehrspohn, F. Garcial-Vidal, M. Notomi, and A. Scherer, editors, *Engineered Porosity for Microphotonics and Plasmonics: MRS Symposium Proceedings*, volume 784, pages C11.60.1–6, Pittsburgh, PA, 2004.

[113] G.P. Wiederrecht, T.P. Dougherty, L. Dhar, and K.A. Nelson. Explanation of anomalous polariton dynamics in $LiTaO_3$. *Phys. Rev. B*, 51:916–931, 1995.

[114] K.K. Wong, editor. *Properties of lithium niobate.* Number 28 in EMIS datareviews series. INSPEC/Institution of Electrical Engineers, London, 2002.

[115] Y.-X. Yan, Jr. Edward B. Gamble, and K.A. Nelson. Impulsive stimulated scattering: General importance in femtosecond laser pulse interactions with matter, and spectroscopic applications. *J. Chem. Phys.*, 83:5391, 1985.

[116] Y.-X. Yan and K.A. Nelson. Impulsive stimulated light scattering. i. general theory. *J. Chem. Phys.*, 87:6240–6256, 1987.

[117] Y.-X. Yan and K.A. Nelson. Impulsive stimulated light scattering. ii. comparison to frequency-domain light scattering spectroscopy. *J. Chem. Phys.*, 87:6257–6265, 1987.

[118] K.H. Yang, P.L. Richards, and Y.R. Shen. Generation of far-infrared radiation by picosecond light pulses in $LiNbO_3$. *Appl. Phys. Lett.*, 19:320, 1971.

[119] K.S. Yee. Numerical solution of initial boundary value problems involving maxwells equations in isotropic media. *IEEE Transactions on Antennas and Propagation*, AP14:302, 1966.

[120] C. Yeh and F.I. Shimabukuro. *The essence of dielectric waveguides.* Springer, 2008.

[121] K.-L. Yeh, J. Hebling, M.C. Hoffmann, and K.A. Nelson. Generation of high average power 1 kHz shaped THz pulses via optical rectification. *Opt. Comm.*, 13:3567–3570, 2008.

[122] K.-L. Yeh, M.C. Hoffmann, J. Hebling, and K.A. Nelson. Generation of 10 $\mu$J ultrashort THz pulses by optical rectification. *Appl. Phys. Lett.*, 90:171121, 2007.

[123] K.-L. Yeh, T. Hornung, J.C. Vaughan, and K.A. Nelson. Terahertz amplification in high-dielectric materials. In P. Corkum, D. Jonas, D. Miller, and A.M. Weiner, editors, *Ultrafast Phenomena XV*, pages 802–804, Berlin, 2007. Springer-Verlag.

[124] K.-L. Yeh, E.R. Statz, J.C. Vaughan, T. Hornung, and K.A. Nelson. Terahertz polaritonics: High-field thz coherent control and spectroscopy. *Lasers and Electro-Optics Society, 2006. LEOS 2006. 19th Annual Meeting of the IEEE*, pages 138–139, Oct. 2006.

[125] O.C. Zienkiewicz. The birth of the finite element method and of computational mechanics. *Int. J. Numer. Meth. Engng*, 60:3–10, 2004.

[126] O.C. Zienkiewicz, R.L. Taylor, and J.Z. Zhu. *Finite Element Method - Its Basis and Fundamentals.* Elsevier, sixth edition, 2005.

[127] William B.J. Zimmerman. *Process Modelling and Simulation with Finite Element Method.* Series on stability, vibration, and control of systems. World Scientific, 2004.